Study on Nonlinear Optical Properties of Ag Nanoparticles: Effect of Size Quantization and Excitation Power Modulation

Study on Nonlinear Optical Properties of Ag Nanoparticles: Effects of Size Quantization and Excitation Power Modulation

Rodrigo Sato
Doctoral Program in Materials Science and Engineering

Submitted to the Graduate School of
Pure and Applied Sciences
in Partial Fulfillment of the Requirements
for the Degree of Doctor of Philosophy in
Engineering

at the
University of Tsukuba

Acknowledgments

Many people deserve recognition for their help and support throughout the years.

Prof. Takeda, thank you for being my supervisor and for all advices and patience. Also, thank you for all the effort you have put in to help me become a better researcher.

Prof. Adelaide and Prof. Zimmerman, thank you for believing in me. Your dedication, support and friendship always inspired me to work hard and improve myself.

Prof. Akimoto, Prof. Sakoda, and Prof. Sekiguchi, thank you very much for being my referees.

To all professors and researches at University of Tsukuba and Nims. In special to Dr. Kishimoto for his wise advices. Also, Prof. Koyano, Prof. Hino, Prof. Sakka, Prof. Nakayama and Prof. Takemori. Dr. Ohi, for supporting the ellipsometry measurements. Dr. Ohnuma and Dr. Suresh, for SAXS measurements. Dr. Oyoshi, for fabrication of the samples.

Lastly, I would like to thank my parents. They raised me, supported me, taught me, and loved me since the very beginning. In addition, they gave me the freedom and the opportunity to pursue my own dreams.

Outline

List of figures

2.7: a) Real and b) imaginary components of the intrinsic dielectric function of Ag nanoparticles with average particles sizes ranging from 3.0 to 16 nm as labeled.

2.8: Normalized absorption efficiency of Ag particles [26].

2.9: a) Larger particles than 10 nm, LSPR is described as a collective oscillations of a free electron gas. b) For particles smaller than 10 nm, quantum finite-size effects result in the plasmon resonance energy blueshift [49].

3.1: Schematic diagram of Z-scan technique.

3.2: Schematic diagram of pump-and-probe spectroscopy.

3.3: Transient transmission changes of Ag NPs embedded in silica glass as a function of excitation intensity.

3.4: Group velocity delay of CaF_2 analyzed by measuring the optical nonlinearities of $SrTiO_3$.

3.5: Time dependences of the transient transmission and reflection changes of 13-nm Ag NPs embedded in silica glass for different probe photon energies as labeled.

3.6: Transient transmission and reflection changes around the LSPR right after an excitation photon energy of 3.1 eV.

3.7: Differential terms of Ag nanoparticles embedded in silica glass numerically calculated.

3.8: Real and imaginary components of the third order susceptibility of Ag nanoparticles embedded in silica glass. Applied electric field of 4.6×10^8 V/m.

3.9: Calculated real and imaginary components of the modulation of dielectric function along with the third order susceptibility of Ag nanoparticles embedded in silica glass. Several a) volume fractions and b) sizes of Ag nanoparticles. Damping constant for free electrons and electron temperature of bound electrons were set at 3.6×10^{14} Hz and 600 K, respectively.

3.10: Calculated real and imaginary components of the third order susceptibility of Ag nanoparticles embedded in silica glass. Damping constant for free electrons and electron temperature of bound electrons were set at 3.6 x 10^{14} Hz and 600 K, respectively. D = 13 nm and p = 0.035.

3.11: Calculated real and imaginary components of the forth power of the local field factor of Ag nanoparticles embedded in silica glass. D = 13 nm.

4.1: Spectral range of white-light continua for three incident wavelengths, 262 (3ω), 393 (2ω) and 785 nm (1ω) [54].

4.2: Dispersion of the transient transmission changes $\Delta T/T$ of Ag nanoparticles in SiO_2 with average particles sizes ranging from 3.0 to 16 nm as labeled. Right after the excitation pulse at 3.1 eV.

4.3: Transmission of 13-nm-diameter Ag nanoparticles at excitation condition along with steady state.

4.4: a) Real and b) imaginary components of the dielectric function of 13-nm-diameter Ag nanoparticles at excitation ($\varepsilon_m^{EXC} = \varepsilon + \Delta\varepsilon$) along with steady state condition.

4.5: a) Real and b) imaginary components of the third-order susceptibility $\chi_{eff}^{(3)}$ of Ag nanoparticles in SiO_2 with average particles sizes ranging from 3.0 to 16 nm as labeled.

4.6: Third-order susceptibility $\left|\chi_{eff}^{(3)}\right|$ of Ag nanoparticles in SiO_2 with average particles sizes ranging from 3.0 to 16 nm as labeled.

4.7: Normalized $\left|\chi_{eff}^{(3)}\right|/\alpha$ (□) and $\left|pf_l^2\left|f_l\right|^2\right|/\alpha$ (p) as a function of the Ag particle size.

4.8: a) Absolute component of the intrinsic third-order susceptibility $\left|\chi_m^{(3)}\right|$ of Ag nanoparticle with average particle sizes ranging from 3.0 to 16 nm as labeled. b) Absolute component of $\left|\chi_m^{(3)}\right|$ of Ag nanoparticle in respect to nanoparticle diameter at 2.5, 3.1 and 3.5 eV.

4.9: Absolute component of the intrinsic third-order susceptibility of an Ag nanoparticle in respect to its size. 0.9 eV. In the inset, results at T = 0 and at T = 300 K [29].

4.10: Absolute component of the intrinsic third-order susceptibility of an Ag nanoparticle in respect to its size. At fixed ratio of $\Gamma_2/\Gamma_1 = 10$ and various values of Γ_2 as labeled [33].

4.11: Real and imaginary components of the dielectric function of an Ag nanoparticle with particle diameter ranging from 2 to 8 nm as labeled [26].

4.12: a) Real and b) imaginary components of the intrinsic third-order susceptibility $\chi_m^{(3)}$ of Ag nanoparticles with average particle sizes ranging from 3.0 to 16 nm as labeled.

5.1: Dispersion of the transient transmission changes $\Delta T/T$ of Ag nanoparticles in SiO_2 with average particles sizes of a) 6.6, b) 9.6, c) 13 and d) 16 nm as labeled. Right after the excitation pulse at 3.1 eV.

5.2: a) Absolute, b) real and c) imaginary components of the local field factor of Ag nanoparticles in SiO_2 with average particle sizes of 6.6, 9.6, 13 and 16 nm as labeled.

5.3: Absolute component of the third-order susceptibility of Ag nanoparticles in SiO_2 with average particle sizes of 6.6, 9.6, 13 and 16 nm as labeled.

5.4: Absolute component of the local field factor of the Ag nanoparticle with particle sizes of a) 6.6, b) 9.6, c) 13 and d) 16 nm.

5.5: Absolute component of the local field factor of an Ag nanoparticle with particle diameters of a) 6 and d) 22 nm [33].

5.6: Transient transmission changes $\Delta T/T$ of Ag nanoparticles embedded in SiO_2 with particle sizes of a) 6.6, b) 9.6, c) 13 and d) 16 nm. Values relative to a maximum pump intensity of 3.70 GW/cm^2. Solid lines are guides to the eyes. Dashed lines represent the linear fit of ΔT / T of 2.80, 3.00, and 3.10 eV up to a relative excitation intensity of 0.42.

5.7: Open aperture Z-scan at several wavelengths in Ag particles in lead-germanium oxide glass with average particle size of 5.4 nm [70].

5.8: Open aperture Z-scan at 3.12 eV (397 nm) in Ag particles in water with particle size of 5-10 nm [71].

5.9: Open aperture Z-scan at 3.07 eV (404 nm) in Ag particles in soda lime glass with estimated particle size of 6.35 (550 °C), 4.62 (500 °C), 3.63 (450 °C), 2.58 nm (350 °C) [72].

5.10: Open aperture Z-scan at 3.07 eV (404 nm) in Ag particles in soda lime glass with estimated particle size of 6.35 (550 °C), 4.62 (500 °C), 3.63 (450 °C), 2.58 nm (350 °C) [32].

Chapter 1

Introduction

Metal nanoparticles have generated considerable interest in recent years owing to their potential applications, however metal nanoparticles have been observed in colored glasses since the late Bronze Age (1200 – 1000 BC) [1]. Its intense color and unusual color change had fascinated many civilizations, including Celts and Romans. A famous colored glass example is the Lycurgus cup from the 4th century. In the Middle Ages and Renaissance, the use of metal nanoparticles had expanded in Europe. It was mainly applied in the fabrication of color glaze decorations on ceramics and church windows [2]. The fabrication process of red glasses expanded worldwide. A famous example outside Europe is the Satsuma glasses produced in Japan from the 19th century [3]. The nature of the intense color of these glasses was only understood in the 1850s by Faraday [4]. By studying ruby glasses, he concluded that its color was due to dispersed gold nanoparticles.

The revival of interest in metal nanoparticles has arisen after several advances in fundamental physical and chemical science [5-7]. In the beginning of the 20th century, the unusual optical properties were linked to the confinement of the quasi-free electrons within the nanoparticles by Mie and Maxwell-Garnett investigations [5]. Metal nanoparticles support the resonant

collective oscillation of these quasi-free electrons by an electromagnetic field excitation as shown in Figure 1.1. This phenomenon is known as localized surface plasmon resonance (LSPR).

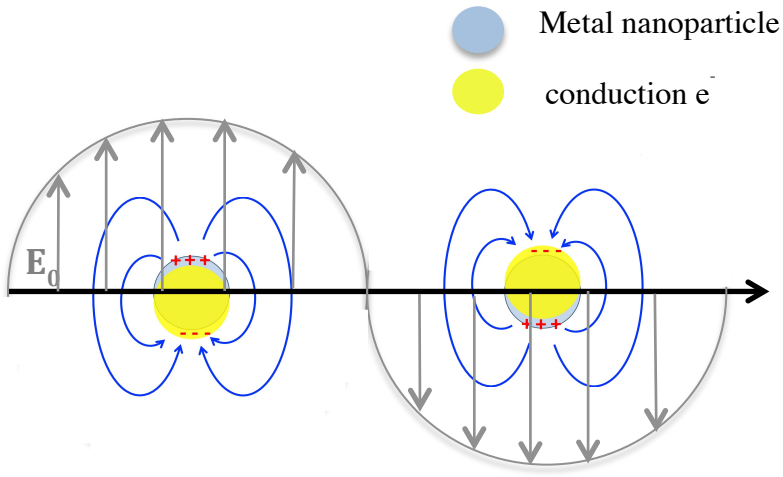

Figure 1.1: Schematic representation of the localized surface plasmon resonance of metal nanoparticle. The quasi-free electrons displacement relative to the particle is shown in yellow.

With advances in the fabrication methods and characterization of metal nanoparticles, better understanding of the fundamental properties provided more advanced insights, including quantum mechanical effects and inter-particle interaction [8]. From the 20th century, experimental and theoretical investigations largely expanded the possibility of applications of metal nanoparticles' LSPR in nanotechnology, raging from biological sensing [9] and cancer treatment [10] to quantum information transfer [11] and ultrafast applications [12] in nanophotonics.

1.1 Background of NLO properties of metal nanoparticles

Metals nanoparticles have generated considerable interest owing to a strong enhancement of their effective nonlinear optical response [13-15]. This enhancement is achieved by the LSPR [5]. Due to large nonlinearity and ultrafast response, metal nanoparticles have potential for applications in nanophotonics technology, including third-harmonic generation, wavelength tuning, and all-optical signal processing and switching [16-18]. By optimizing the nanoparticle's size and shape, the control of the light confinement in the nanoscale via nonlinear modulation of the local electric field may provide new interesting applications [17].

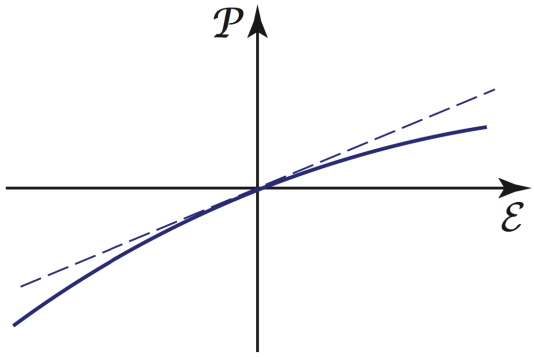

Figure 1.2: Schematic representation of the nonlinear optical response in a strong electromagnetic field.

When a metal nanoparticle is subject to a strong electromagnetic field the motion of the electrons cannot be considered harmonic and the induced polarization **P** becomes nonlinear with respect to the applied field (Figure 1.2). The anharmonic **P** can be expanded as power series in respect to the electric field **E**. In nanospheres, the even-order nonlinearities vanish due to inversion symmetry [19]. Therefore, the first non-zero nonlinear component is the third-order. This component contains terms in the applied frequencies leading to nonlinear changes of the dielectric function, known as optical Kerr

effect. Owing to the plasmonics effects, the effective third-order susceptibility $\chi_{eff}^{(3)}$ of Ag nanoparticles composites is strongly enhanced by the forth power of the local field factor $f_l^2(\omega_{probe})\left|f_l(\omega_{pump})\right|^2$. Using Maxwell-Garnett effective medium approximation, $\chi_{eff}^{(3)}$ can be expressed as

$$\chi_{eff}^{(3)}(\omega_{probe}) = pf_l^2(\omega_{probe})\left|f_l(\omega_{pump})\right|^2 \chi_m^{(3)}(\omega_{probe}), \quad (1.1)$$

where p is the volume fraction of metal and $\chi_m^{(3)}$ is the intrinsic third-order susceptibility of Ag nanoparticles itself. To understand $\chi_{eff}^{(3)}$, characterization of the local field factor and $\chi_m^{(3)}$ are necessary.

Experimentally, the third-order nonlinearities of metal nanoparticles have been investigated by means of Z-scan, degenerate four-wave mixing (DFWM), and pump-and-probe methods [20-23]. In the last 25 years, the evaluations of the $\chi_{eff}^{(3)}$, and rarely $\chi_m^{(3)}$, were often performed for one wavelength only. Far-field optical measurements of metal nanoparticles have proven challenging due to reduced absorption and scattering with a^{-3} and a^{-6}, respectively [24]. Figure 1.3 shows a review of $\chi^{(3)}$ by Stepanov [25]. Owing to the resonant behavior of the conduction electrons of the Ag nanoparticles, $\chi_{eff}^{(3)}$ shows strong spectral dependence. Furthermore, quantum finite-size effects modify the plasmon resonance of Ag particles smaller than 15 nm and it is expect to impact the nonlinear response. Scattered values of $\chi_{eff}^{(3)}$ for different particle sizes at various excitation laser characteristics restrict the understanding of the mechanisms underlying the optical nonlinearities of Ag nanoparticles.

Nonlinear optical properties of implanted metal nanoparticles in various transparent matrixes...

Metal (Ion)	Matrix	Synthesis conditions: Energy (E), keV, Dose (D), ion/cm^2, Current density (J), μA/cm^2, Annealing temper. (T), °C and time	Study nonlinear optical method	Laser parameters: Wavelength (λ), nm, Pulse duration (τ), ps, Repetition rate (ν), Hz; Intensity (I_0), W/cm^2 Pulse energy (P), mJ	Nonlinear parameters: Refract. coef. (n_2), cm^2/W Absorption coef. (β), cm/W Satur. intensity (I_{sat}), W/cm^2 Re$\chi^{(3)}$], Im$\chi^{(3)}$], $\lvert\chi^{(3)}\rvert$, esu	Authors
Ag	SiO_2	E = 1.5×10^3 D = 4.0×10^{16} J = 2 T = 500, 1 h	Z-scan	λ = 532 τ = 4.5 ν = 76×10^6	$\lvert\chi^{(3)}\rvert$ = 5.0×10^{-7}	Ila *et al.* 1998 [50]
Ag	SiO_2	E = 60 D = 4.0×10^{16} J = 10	Z-scan	λ=354.7 τ = 55 ν = 2 I_0 = 1.3×10^9	n_2 = -2.7×10^{-7} Re$[\chi^{(3)}]$ = -6.0×10^{-8} β = -1.4×10^{-5} Im$[\chi^{(3)}]$ = -6.1×10^{-9} $\lvert\chi^{(3)}\rvert$ = 6.1×10^{-8}	Ganeev *et al.* 2003 [58]2004 [63]
Ag	SiO_2	E = 60 D = 4.0×10^{16} J = 10	Z-scan	λ = 532 τ = 55 ν = 2 I_0 = (2.5 - 14)×10^9	n_2 = -(6.2 - 0.7)×10^{-10} Re$[\chi^{(3)}]$ = -(3.5 - 0.4)×10^{-8} β = -(3.6 - 0.5)×10^{-5} Im$[\chi^{(3)}]$ = -(1.3 - 0.2)×10^{-8}	Ganeev *et al.* 2004 [84] Stepanov *et al.* 2010 [85]
Ag	SiO_2	E = 60 D = 4.0×10^{16} J = 10	Z-scan	λ = 1064 τ = 35 ν = 2 I_0 = 1.0×10^{10}	n_2 = 1.5×10^{-8} Re$[\chi^{(3)}]$ = 2.5×10^{-9}	Ganeev *et al.* 2003 [62]2004 [63]
Ag	SiO_2	E = (1.7 - 2.4)×10^3 D = (4.0 - 7.0)×10^{16} J = 0.3 T = 500, 1 h	Z-scan	λ = 532 τ = 7.0×10^3 P = 0.14	Three-photon absorption	Joseph *et al.* 2007 [86]
Ag	SiO_2	E = 2.0×10^3 D = 7.0×10^{16} T = 600, 1 h	Z-scan	λ = 527 τ = 0.233 ν = ×10^3	β = -(2.6 - 1.8)×10^{-6} Im$[\chi^{(3)}]$ = 4.7×10^{-10} I_{sat} = (1.2 - 3.5)×10^7	Rangel-Rojo *et al.* 2009 [87]2010 [88]
Ag	SiO_2	E = 200 D = 2.0×10^{17} J = 2.5	Z-scan	λ = 532 τ = 38 ν = 10	n_2 = -3.0×10^{-11} Re$[\chi^{(3)}]$ = 3.0×10^{-8} β = -7.0×10^{-8} Im$[\chi^{(3)}]$ = 2.6×10^{-8} $\lvert\chi^{(3)}\rvert$ = 4.0×10^{-8}	Wang *et al.* 2009 [89]
Ag	SiO_2	E = 200 D = 2.0×10^{17} J = 2.5	Z-scan	λ = 1064 τ = 38 ν = 10	n_2 = -1.7×10^{-10} Re$[\chi^{(3)}]$ = 1.8×10^{-7} $\lvert\chi^{(3)}\rvert$ = 1.8×10^{-7}	Wang *et al.* 2009 [89]

Figure 1.3: Optical nonlinearities parameters from the literature reviewed by A. L. Stepanov [25]. $\chi^{(3)}$ represents the effective third-order susceptibility of the Ag nanoparticles composite.

Quantum finite-size effects lead to a substantial change in the plasmonic resonance of Ag nanoparticles. Scholl *et al.* [26] experimentally showed plasmonic resonance blueshift of 0.5 eV with decrease of particle size from 20 to 1.7 nm. Using an analytical quantum model, these authors attributed the blueshift to an increase in the dielectric function of the Ag nanoparticles. However, quantum effects in the nonlinear properties remain poorly understood. Using DFWM, Ushida *et al.* [27] investigated the size dependence of $\left|\chi_m^{(3)}\right|$ of Ag nanoparticles for sizes varying from 4.2 to 31 nm. These authors concluded that $\left|\chi_m^{(3)}\right|$ is roughly size independent. Using DFWM, Yang *et al.* [28] investigated Cu nanoparticles for sizes varying from 5.2 to 12.6 nm. These authors concluded that $\left|\chi_m^{(3)}\right|$ shows $1/a^3$ dependence. It's expected that the size dependence of $\left|\chi_m^{(3)}\right|$ is due to the contribution of conduction electrons only. From the noble metals, Cu has the relative highest contribution of interband transitions at the LSPR. Consequently, Ag particles are expected to be highly sensitive to the quantum finite-size effects. Using a numerical and analytical approach, Govyadinov *et al.* [29] have yielded predictions of spectral and size dependences of $\chi_m^{(3)}$.

Optical nonlinearities of Ag nanoparticles not only depend on intrinsic nonlinearities $\chi_m^{(3)}$ but also on extrinsic components, volume fraction and local field factor. Ag nanoparticles has been investigated with respect to excitation intensity dependence. The sign of the transient transmission changes $\Delta T/T$ has been found to change with the excitation intensity. Gurudas *et al.* [30] and Zeng *et al.* [31] have reported positive to negative sign change with increasing excitation intensity. Conversely, Henari *et al.* [32] have reported negative to positive sign change. The origin of $\Delta T/T$ has been attributed to several processes. Intuitively, positive $\Delta T/T$ is explained as saturation of the conduction electron transitions. On the other hand, negative $\Delta T/T$ is

explained by conflicting processes, including two- and three-photon absorption, reverse saturable absorption, and nonlinear scattering [30-32]. Using a numerical calculation, Drachev *et al.* [33] have reported the nonlinear modulation of the plasmonic resonance of a 22-nm-sized Ag particle. These authors yielded predictions of plasmonic resonance redshifts at strong excitation. Experimental investigations show conflicting results with those derived from numerical calculations.

1.2 Fundamentals of NLO properties of metal nanoparticles

Induced polarization **P** expanded in a power series of the electric field **E** [34]

$$\mathbf{P} = \varepsilon_{m,0}\left(\chi_m^{(1)}\mathbf{E} + \chi_m^{(2)}\mathbf{EE} + \chi_m^{(3)}\mathbf{EEE} + \chi_m^{(4)}\mathbf{EEEE} + ...\right). \quad (1.2)$$

For centrosymmetric media (i.e. spheres), the even-orders $\chi_m^{(n)}$ vanish. The first non-zero $\chi_m^{(n)}$ is then the third-order as

$$\mathbf{P} = \varepsilon_{m,0}\left(\chi_m^{(1)} + \chi_m^{(3)}|\mathbf{E}|^2\right)\mathbf{E}. \quad (1.3)$$

1.2.1 Effective third-order nonlinear susceptibility of spherical metal particles composite

Under Maxwell-Garnett effective medium approximation (EMA), the effective dielectric function ε_{eff} is given as [19]

$$\frac{\varepsilon_{eff} - \varepsilon_d}{L\varepsilon_{eff} + (1-L)\varepsilon_d} = p\frac{\varepsilon_m - \varepsilon_d}{L\varepsilon_m + (1-L)\varepsilon_d}, \qquad L = 1/3 \text{ for spheres.} \quad (1.4a)$$

$$\varepsilon_{eff} = \varepsilon_d \frac{(1+2p)\varepsilon_m + 2(1-p)\varepsilon_d}{(1-p)\varepsilon_m + (2+p)\varepsilon_d}, \tag{1.4b}$$

$$\varepsilon_{eff} = \frac{(1+2p)\varepsilon_m\varepsilon_d}{(1-p)\varepsilon_m + (2+p)\varepsilon_d} + \frac{2(1-p)\varepsilon_d^2}{(1-p)\varepsilon_m + (2+p)\varepsilon_d}, \tag{1.4b}$$

where p is the volume fraction of Ag nanoparticles. For a small-induced change, the variation of ε_{eff} and ε_m can be expressed as

$$\delta\varepsilon_{eff} = \tfrac{3}{4}\chi_{eff}^{(3)}\left|\mathbf{E}_0\right|^2, \tag{1.5a}$$

$$\delta\varepsilon_m = \tfrac{3}{4}\chi_m^{(3)}\left|\mathbf{E}\right|^2. \tag{1.5a}$$

Dividing equation (1.5a) by (1.5b)

$$\frac{\partial\varepsilon_{eff}}{\partial\varepsilon_m} = \frac{\chi_{eff}^{(3)}\left|\mathbf{E}_0\right|^2}{\chi_m^{(3)}\left|\mathbf{E}\right|^2}. \tag{1.6}$$

Deriving ε_{eff} with respect to ε_m

$$\frac{\partial\varepsilon_{eff}}{\partial\varepsilon_m} = \left\{\frac{(1+2p)\varepsilon_d\left[(1-p)\varepsilon_m + (2+p)\varepsilon_d\right] - (1+2p)(1-p)\varepsilon_d\varepsilon_m}{\left[(1-p)\varepsilon_m + (2+p)\varepsilon_d\right]^2}\right\}$$

$$+\left\{\frac{-2(1-p)^2\varepsilon_d^2}{\left[(1-p)\varepsilon_m + (2+p)\varepsilon_d\right]^2}\right\}, \tag{1.7a}$$

$$\frac{\partial\varepsilon_{eff}}{\partial\varepsilon_m} = \frac{\left[(1+2p)(2+p) - 2(1-p)^2\right]\varepsilon_d^2}{\left[(1-p)\varepsilon_m + (2+p)\varepsilon_d\right]^2}, \tag{1.7b}$$

$$\frac{\partial \varepsilon_{eff}}{\partial \varepsilon_m} = \frac{\left(2+p+4p+2p^2-2-2p^2+4p\right)\varepsilon_d^2}{(1-p)^2\varepsilon_m^2+(2+p)^2\varepsilon_d^2+2(1-p)(2+p)\varepsilon_m\varepsilon_d}, \tag{1.7c}$$

For $p << 1$,

$$\frac{\partial \varepsilon_{eff}}{\partial \varepsilon_m} = p\left(\frac{3\varepsilon_d}{\varepsilon_m+2\varepsilon_d}\right)^2 = pf_l^2 . \tag{1.8}$$

From equation (1.6) and (1.8),

$$\frac{\partial \varepsilon_{eff}}{\partial \varepsilon_m} = \frac{\chi_{eff}^{(3)}\left|\mathbf{E}_0\right|^2}{\chi_m^{(3)}\left|\mathbf{E}\right|^2} = pf_l^2 , \tag{1.9}$$

then we obtain,

$$\chi_{eff}^{(3)} = p\left(\frac{3\varepsilon_d}{\varepsilon_m+2\varepsilon_d}\right)^2\left|\frac{3\varepsilon_d}{\varepsilon_m+2\varepsilon_d}\right|^2\chi_m^{(3)} . \tag{1.10}$$

1.3 Motivation and research objective

Despite the great effort to investigate the nonlinear optical properties of metal nanostructures in the last 25 years, much remains to be understood in fundamental optical properties. Experimentally, the optical nonlinearities of metal nanoparticles have been often investigated for one wavelength only. Owing to the plasmonic resonance of the Ag nanoparticles, optical nonlinearities are expected to shows strong spectral dependence around the LSPR. Scattered experimental measurements for different particle sizes at

various excitation laser characteristics restrict the understanding of the mechanisms underlying the optical nonlinearities of Ag nanoparticles.

Quantum finite-size effects on the intrinsic nonlinear optical response of metal nanostructures have been experimentally investigated by several groups. For Ag particles, size independence to the intrinsic nonlinear optical properties has been concluded [27]. Cu particles were found to follow the $1/a^3$ dependence [28]. There has been no explanation for these conflicting experimental results. Optical nonlinearities of Ag nanostructures not only depend on intrinsic nonlinearities but also on extrinsic components, volume fraction and local field factor. Using a numerical calculation, Drachev *et al.* [33] have reported the nonlinear modulation of the plasmonic resonance of a 22-nm-sized Ag particle. These authors yielded predictions of plasmonic resonance redshifts at strong excitation via nonlinear modulation of the local field factor. Experimental evaluation of the dispersion of the optical nonlinearities with excitation dependence is necessary for comprehending the modulation of the local field factor.

This thesis describes the fabrication of Ag nanoparticles embedded in silica glass by ion-implantation. Ion-implanted metal nanoparticles have several advantages, including chemical stability and ligands free. Several samples were fabricated with average particle sizes from 3.0 to 16 nm. By using femtosecond pump-and-probe spectroscopy, the dispersion of the optical nonlinearities was investigated. This technique has the advantage to analyze the optical nonlinearities in a wide wavelength range. I have systematically investigated the size dependence in the intrinsic nonlinear optical properties of 3.0-16-nm-size Ag nanoparticles in silica glass. From these results, the quantum finite-size effects were discussed. In addition, I have systematically investigated the excitation power dependence in the nonlinear optical properties of Ag nanoparticles embedded in silica glass. From these results,

the modulation of the local field factor controlled by optical nonlinearity was discussed. This Thesis will explore fundamental properties of metal nanoparticles and discuss the conflicting results from previous investigations. To move the nanoplasmonics technology from concepts to applications significant challenges and clarification of fundamental optical properties have to be solved. Also, better understanding of optical nonlinearities of metal nanostructures may provide new interesting application in quantum plasmonics, including single-photon generation and ultra-compact devices for integrated components [35,36].

Chapter 2

Ag nanoparticles: Fabrication and linear optical properties

2.1 Introduction

Owing to potential applications to nanotechnology, metal nanoparticles have generated considerable interest. The development of nanofabrication techniques along with nanocharacterization has allowed the exploration of the fundamental optical properties. The linear optical properties of these nanoparticles have been extensively characterized. However, several experimental investigations have shown plasmon resonances redshifts or blueshifts as the particle size decreases owing to a small absorption and scattering of metal particles smaller than the electron mean free path [26, 37-39]. For colloidal nanoparticles, the surface damping effects of the ligands also modify the optical properties [26]. Classical theoretical calculations have predicted plasmon resonance redshift as the particle decreases. These calculations include increased electron surface scattering for smaller particles

to modify the metal permittivity by using Drude model [26]. Contrarily, density functional theory (DFT) has predicted plasmon resonance blueshift as the particle decreases. However, DFT calculation is limited by computation time and can predict metal permittivity up to 2 nm [8].

More recently, theoretical and experimental investigations have characterized the quantum behavior of the conduction electrons inside the metal nanoparticles. By using aberration-corrected transmission electron microscope (TEM) imaging along with scanning TEM electron-loss spectroscopy, Scholl et al. [26] observed a plasmon resonance blueshift of individual Ag particles without ligands as the particle size decrease. By using Drude model and Lorentzian terms defined quantum mechanically, these authors calculated the permittivity of Ag nanoparticles considering the conduction electrons as a free electrons gas in an infinite spherical potential well. Similarly to experimental results, a plasmon resonance blueshift was predicted as the particle size decreases from 25 to 2 nm with a strong shift for particles smaller than 10 nm.

In this Chapter, the fabrication and structural characterization of the ion-implanted Ag nanoparticles embedded in SiO_2 is described. Ion-implanted metal nanoparticles have several advantages, including chemical stability and ligands free. In general, size distribution of ion-implanted nanoparticles obscures the size effects in LSPR. However, here I show the linear optical properties of the present samples and the compatibility with experimental and theoretical previous results [26,40].

2.2 Samples fabrication

2.2.1 Ion beam implantation

Ion accelerator system injects atoms into the near surface of a substrate for material modification and fabrication of metal nanoparticles composites [41-43]. Here, the implantation was realized with a high-current 60 keV Ag^- beam. Ag^- ions were generated by a Cs-assisted Ag source of plasma sputter type. Negative ions have the advantage to reduce the surface charging by balancing with secondary electron emission from the substrate interface [44]. Vertical and horizontal scanners at 5.0 and 0.9 kHz, respectively, were used to improve the ion beam distribution. The total fluence, number of ions corresponding to a cross-sectional area, of Ag^- ions was varied from 2.4 to 5.2 x 10^{16} ion/cm^2 to control the particle size. The total fluence was obtained by multiplying the implantation time with the ion beam current of 1.6 μA/cm^2 measured by a Faraday cup [44]. The ion implantation was realized in amorphous SiO_2 substrates (KU-1: OH 820 ppm). The fabrication of the samples was carried out in a controlled vacuum lower than 10^{-4} Pa. Ag^- ions range was estimated by TRIM code that is a Monte Carlo (MC) simulation. This code calculates the ion range into the substrate using a quantum mechanical approach considering the ion-atom collisions [45]. For a 60 keV Ag^- ions into a SiO_2 substrate, the estimated ion range was of 39 nm (Figure 2.1). The ion implantation leads to an approximately Gaussian depth distribution. Sputtering of Ag^- ions and atoms from the substrate owing to the fabrication process were not considered. Nevertheless, this result shows that the Ag^- ions maximum concentration is just under the substrate surface.

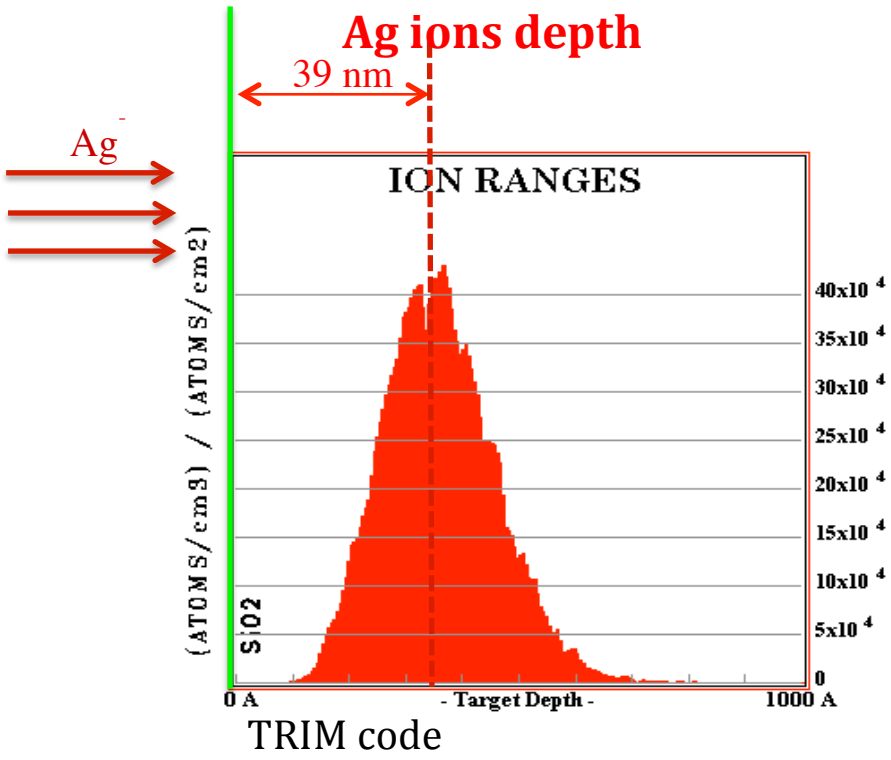

Figure 2.1: Estimated ion range by using TRIM code. Calculation based on 60 keV Ag^- ions into a SiO_2 substrate and total fluence of 10^{17} ion/cm^2.

The nanoparticles formation inside a substrate is the result of several processes, including ion implantation, diffusion, nucleation and ultimately the nanoparticles growth [25]. A schematic description of these processes with respect to the total fluence is shown in Figure 2.2. For a 60 keV Ag^- ions in silica glass, the ions reach the solubility threshold inside the substrate around 5 x 10^{15} ion/cm^2. As the Ag^- ions slow down, Ag-Ag bonds formation are preferred. Although Ag-O has a lower Gibbs free energy of -2.68 kcal/mol than pure Ag metal of 0 kcal/mol, SiO_2 formation has a much lower free energy of -200 kcal/mol. Therefore, oxygen preferably will bond with silicon to SiO_2 formation and the dissociation of Ag-O bonds occurs to reduce the

system total energy. These Gibbs free energies are values calculated at 25 °C. After reaching the supersaturation of Ag atoms, nucleation and spherical-particle growth takes place by an irradiation-enhanced diffusion process [43]. In a supersaturated system, smaller particles are more energetically unstable. Ostwald ripening is the dissolution of these smaller particles creating free Ag atoms that are then incorporated into larger particles. This reduces the particles' surface to area ratio. As the particles grow, Ostwald ripening effect enhances the particle growth by reaching a more thermodynamically stable state of the system.

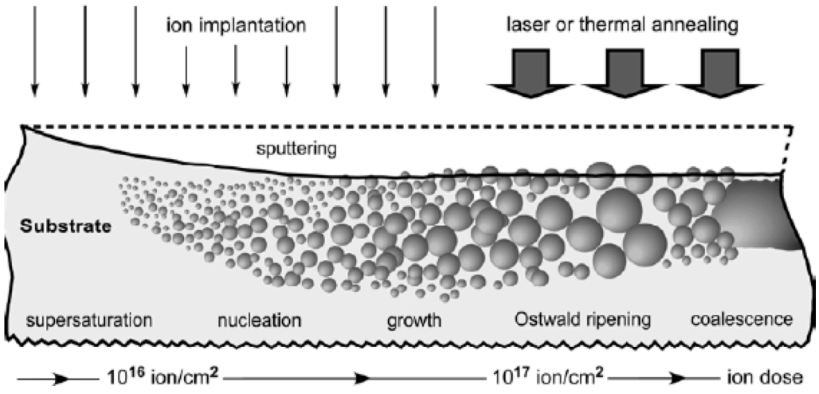

Figure 2.2: Schematic description of ion implantation and particle growth processes with respect to the total fluence [25].

2.2.2 Structural characterization

Small-angle X-ray scattering (SAXS) is a technique that measures the elastic scattering of X-rays at very low angles by a sample containing clusters in the nanosize range. Here, particle size and distribution were analyzed by SAXS (Rigaku, Mo target PSAXS 3S). By using the Debye equation, the general formulation for the scattered intensity of the SAXS profile is given as [46]

$$I(Q) = \sum_{i=1}^{n} \sum_{j=1}^{n} f_i f_j \frac{\sin(Qr_{ij})}{Qr_{ij}}, \tag{2.1}$$

where $\sin(Qr_{ij})/Qr_{ij}$ can be simplified with Mclaurin series. For a very small angle, Guinier approximation is given by

$$I(Q) = I(0)\exp(-R_g^2 Q^2 / 3), \tag{2.2a}$$

$$d = 2R_g\sqrt{5/3}, \tag{2.2b}$$

where R_g is the radius of gyration and d is the particle diameter.

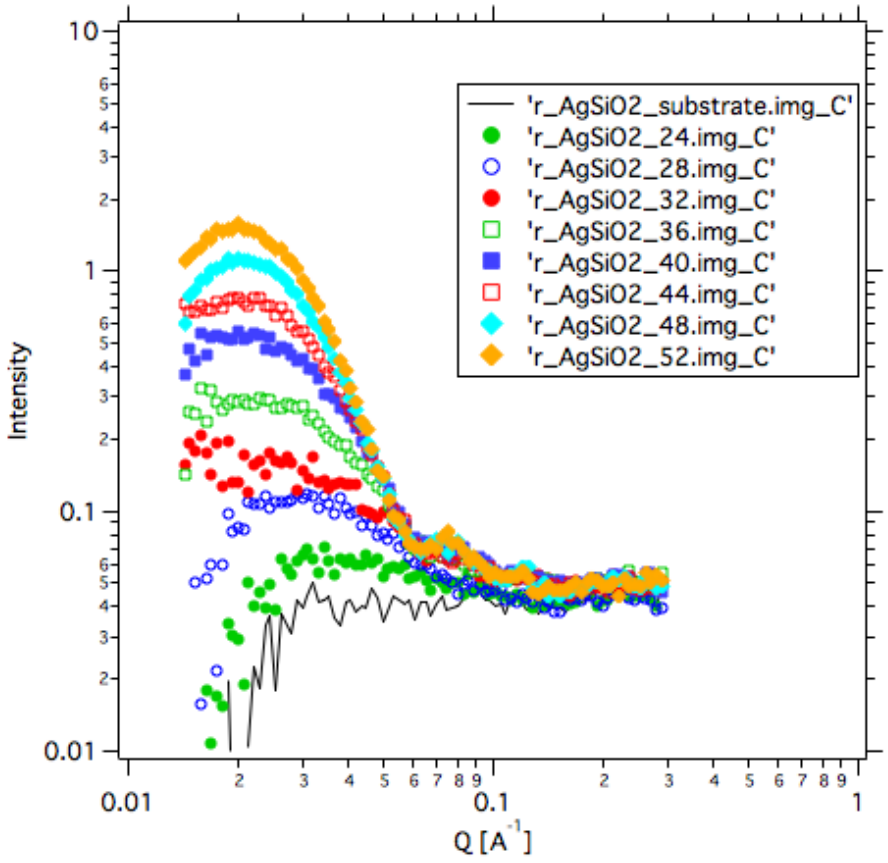

Figure 2.3: SAXS profile of Ag nanoparticles embedded in silica glass. Black line represents the virgin substrate.

The analyzed particle size diameter and standard deviation calculated from a log-normal size distribution are shown in Table 2.1. By SAXS profile, samples AgSiO2_32 showed a broad size distribution, therefore, was discarded.

Table 2.1: Description of average Ag particle sizes. Ag nanoparticles embedded in silica glass.

Sample	Total fluence (10^{16} ion/cm^2)	Average diameter (nm)
AgSiO2_24	2.4	3.0 ± 0.6
AgSiO2_28	2.8	6.6 ± 0.6
AgSiO2_36	3.6	9.6 ± 1.1
AgSiO2_40	4.0	12 ± 1.0
AgSiO2_44	4.4	13 ± 1.2
AgSiO2_48	4.8	15 ± 1.4
AgSiO2_52	5.2	16 ± 1.4

2.3 Linear optical properties

2.3.1 Spectroscopic ellipsometry measurements

Spectroscopic ellipsometry is a technique that measures the polarization changes of the reflected light from a sample. These changes are quantified by the phase difference Δ and amplitude ratio ψ between the p- and s-polarized light waves [47]

$$\tan\psi \exp(i\Delta) \equiv \frac{r_p}{r_s}, \qquad (2.3)$$

where r_p and r_s are the reflection coefficient of the p- and s-polarizations. Here, the linear optical properties, including the dielectric functions and transmission, were analyzed by the rotating analyzer spectroscopic ellipsometry (J. A. Woollam, VASE). The equipment provides spectral range from 240 to 1100 nm. Angles of incident were defined from 55° to 65° with 5° step. For a silica glass substrate, this angle increases the ellipsometry sensitivity by maximizing the differences between the p- and s-polarizations owing to proximity to the Brewster angle [47].

Ellipsometry is an indirect measurement technique; therefore an optical model is needed to obtain the optical properties. Owing to a low volume fraction of Ag ($< 10\%$) and single particle size distribution in the fabricated samples, the particles layer was assumed homogeneous and Maxwell-Garnett effective medium theory (EMA) was applied. The optical properties of the EMA, Ag particles composite, was modeled by using the intrinsic optical properties of the Ag particles and SiO_2. The imaginary component of the Ag dielectric function was modeled as oscillators accounting for the contribution of free and bound electrons. The imaginary component of the SiO_2 was modeled by Cauchy functions. Fitting process was quantified by the root mean squared error values. The real components were obtained by Kramers Kronig relation. Figure 2.4 shows the experimental and fitting of ψ and Δ of 13-nm-Ag nanoparticles.

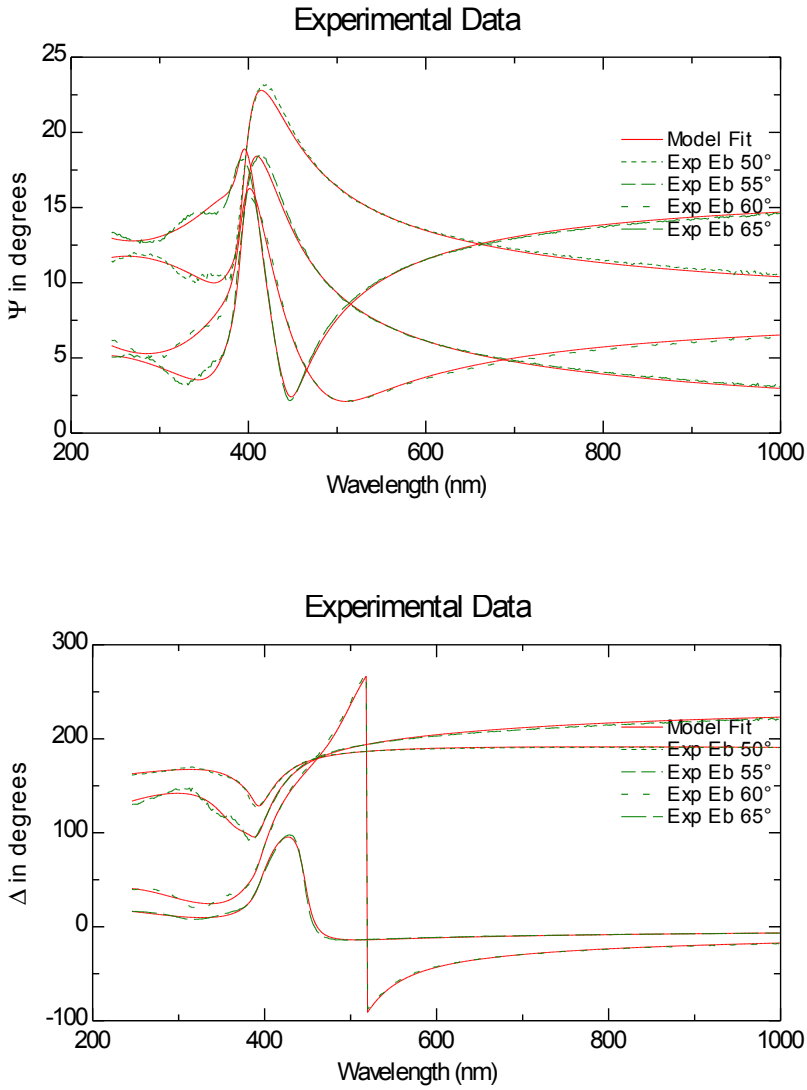

Figure 2.4: Experimental and fitting of ψ and Δ of 13-nm-Ag nanoparticles.

From the ellipsometric model, the layer thickness and volume fraction of Ag embedded in SiO_2 were analyzed and shown in Table 2.2. As the particle size increases, the Ag particles layer and volume fraction decreases and increases, respectively. This is due to the fabrication process by ion implantation. With increase of implantation time, the amount of Ag atoms increases and a complex process, including sputtering effects, reduces the depth of Ag particles inside the SiO_2.

Table 2.2: Description of structural properties of Ag particles composite layer.

Sample	Layer thickness (nm)	Volume fraction (%)
AgSiO2_24	65	3.2
AgSiO2_28	62	3.8
AgSiO2_36	61	4.6
AgSiO2_40	59	5.4
AgSiO2_44	56	6.2
AgSiO2_48	52	7.5
AgSiO2_52	53	7.9

2.3.2 Size dependence of the linear optical properties

From ellipsometric model, the dielectric function of the Ag particles composites (EMA) was analyzed and shown in Figure 2.5. The resonance structure of the dielectric function of Ag particles composites is due to the dipole plasmon resonance. As the particle size increases, the intensity of the dielectric function around the LSPR increases owing to the local field enhancement. This increase can also be observed in the absorption coefficient (Figure 2.6). The absorption coefficient of metal particles can be related to the local field factor f and Ag imaginary component of the dielectric function ε_m'' as

$$\alpha = p\left(\frac{\omega}{nc}\right)\left|f_l\right|^2 \varepsilon_m'', \tag{2.4}$$

where p is the volume fraction of Ag, n is the refractive index of silica glass and c is the speed of light.

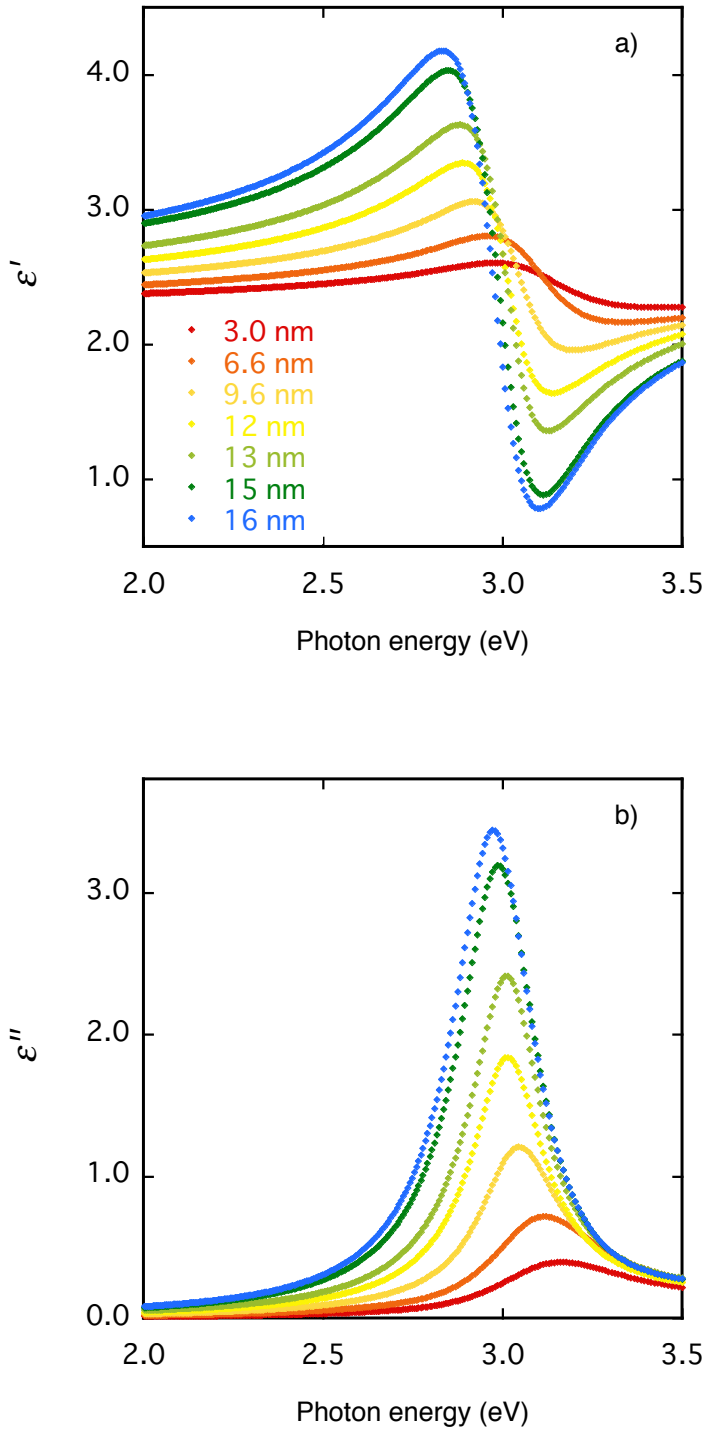

Figure 2.5: a) Real and b) imaginary components of the dielectric function of Ag nanoparticles composites with average particles sizes ranging from 3.0 to 16 nm as labeled.

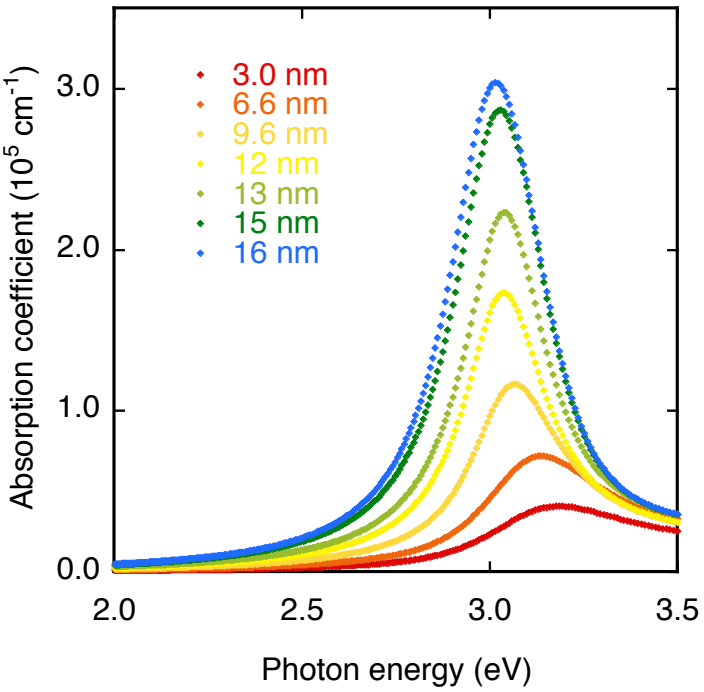

Figure 2.6: Absorption coefficient of Ag nanoparticles embedded in silica glass with average particles sizes ranging from 3.0 to 16 nm as labeled.

The intrinsic dielectric function of Ag particles ε_m was also analyzed by the spectroscopic ellipsometry and is shown in Figure 2.7. Bulk dielectric function of Ag measured by Johnson and Christy [48] is shown as a black dashed line. As the Ag particle size decrease, one can observe an overall intensity increase in the real and imaginary components. To understand the size dependence in the linear optical properties, the calculation of the absorption coefficient by using a density functional theory (DFT) model with local density approximation will be discussed next.

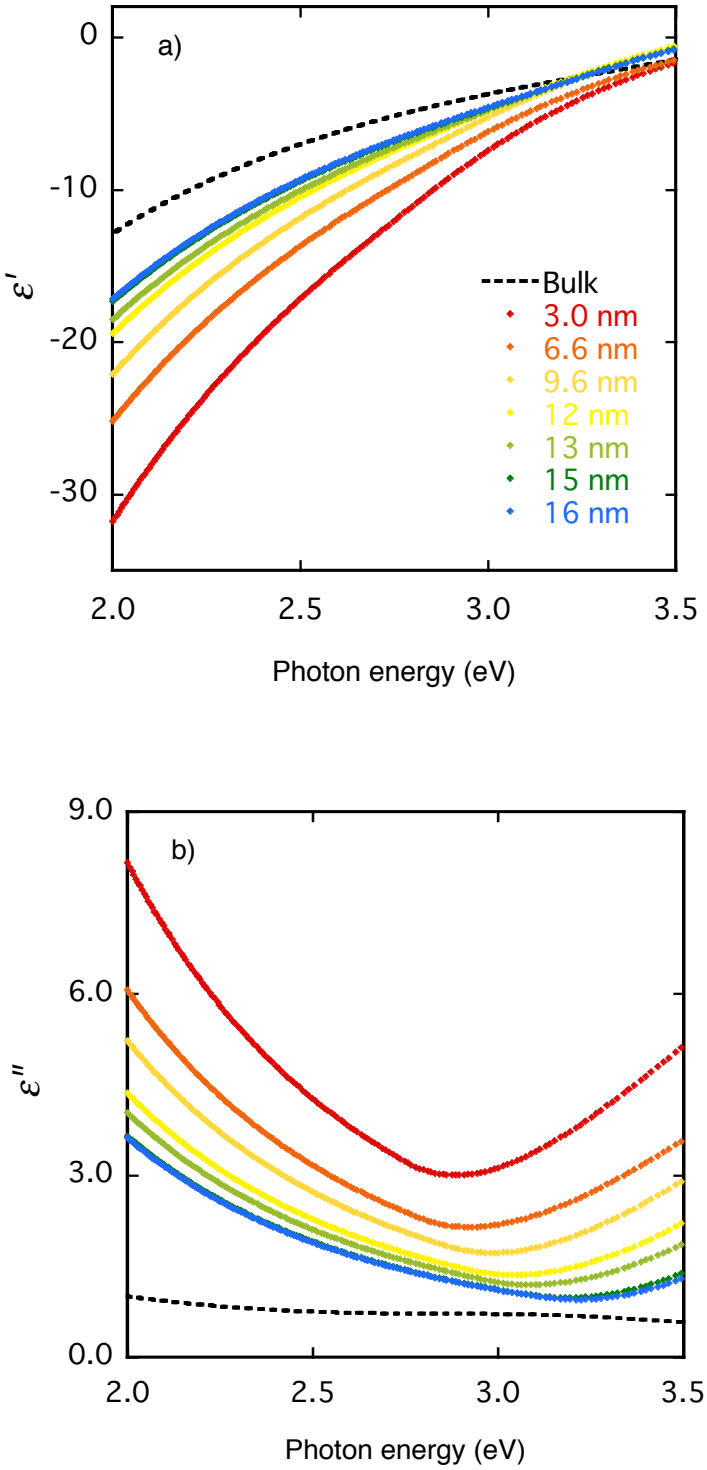

Figure 2.7: a) Real and b) imaginary components of the intrinsic dielectric function of Ag nanoparticles with average particles sizes ranging from 3.0 to 16 nm as labeled.

Figure 2.8 shows the experimental peak position of the LSPR of individual Ag particles by using monochromated scanning TEM electron energy-loss spectroscopy (black dots) [26]. White dashed line indicates the classical Mie Theory peak position prediction. Grey dots and line indicate experimental and theoretical predictions, respectively, of the bulk resonance peak position. By optical measurements, the bulk resonance cannot be observed owing to the mode symmetry. Therefore, the bulk resonance will not be discussed here. The normalized absorption efficiency obtained by extrapolating the DFT-calculated dielectric function is also shown. Under particle size of 2.7 nm, DFT technique was used to obtain the dielectric function of Ag particles. From 2.7 to 25 nm, the results were extrapolated. From experimental and theoretical results, a strong peak blueshift was observed with particle size decrease.

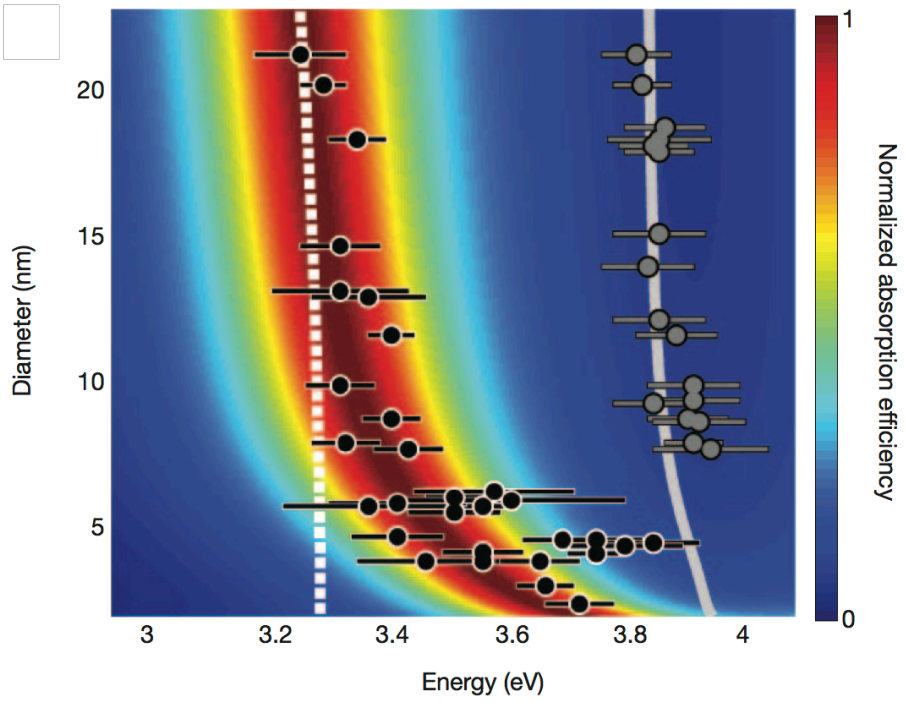

Figure 2.8: Normalized absorption efficiency of Ag particles [26].

The plasmon resonance blueshift of Ag particles with size decrease are explained as quantum finite-size effects. For particle sizes in the quantum regime, the conduction electrons have discrete energy levels. Consequently, only certain electronic transitions are allowed. This discretization of electronic transitions modifies the dielectric function of the metal particle, leading to the plasmon resonance shift with particle size (Figure 2.9). The above experimental and theoretical results of the linear optical properties of Ag particles from the literature show that the present ion-implanted samples have compatible results and therefore suitable for characterization of size dependence of the nonlinear properties.

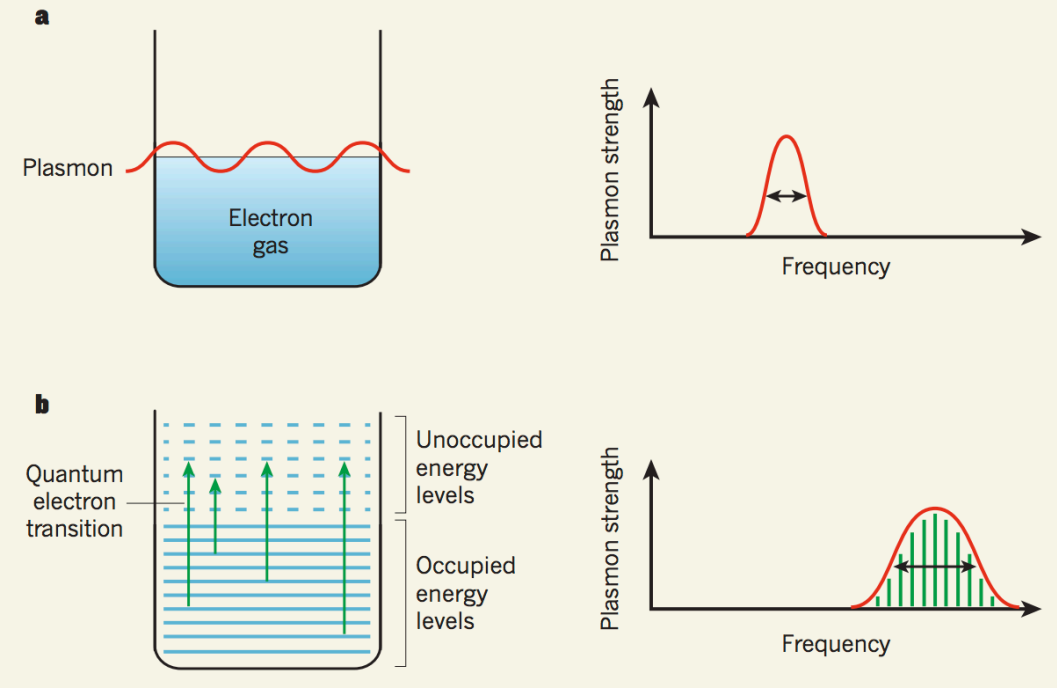

Figure 2.9: a) Larger particles than 10 nm, LSPR is described as a collective oscillations of a free electron gas. b) For particles smaller than 10 nm, quantum finite-size effects result in the plasmon resonance energy blueshift [49].

Chapter 3

Dispersion of NLO properties of Ag nanoparticles

3.1 Introduction

Theoretical approaches, quantum finite-size effects of conduction electrons and classical Mie theory, to optical properties of metal particles have yielded predictions regarding strong spectral dependence of $\chi_{eff}^{(3)}$ [50]. However, experimental investigations were mostly realized for single wavelengths only by means of Z-scan, degenerate four-wave mixing (DFWM), and pump-and-probe methods. This treatment restricts the understanding of the mechanisms underlying the nonlinear optical properties (See Fig 1.3).

In this Chapter, the dispersion of $\chi_{eff}^{(3)}$ of Ag nanoparticles embedded in silica glass is investigated around the LSPR. Experimentally, $\chi_{eff}^{(3)}$ was obtained from the refractive index of the Ag nanoparticles layer using a spectroscopic ellipsometry and $\Delta T/T$ using a femtosecond pump-and-probe spectroscopy. Under Maxwell-Garnett approximation, as described in chapter 1,

$$\chi_{eff}^{(3)}(\omega_{probe}) = pf_l^2(\omega_{probe})\left|f_l(\omega_{pump})\right|^2 \chi_m^{(3)}(\omega_{probe}). \quad (3.1)$$

Individual contribution of the local field factor and $\chi_m^{(3)}$ are discussed. These quantities are compared to those from calculated results. Around the LSPR, the dispersion of the $\chi_{eff}^{(3)}$ greatly reflects the local field enhancement.

3.2 Pump-and-probe spectroscopy

3.2.1 Scope

Optical nonlinearities of Ag nanoparticles have been investigated by means of pump-and-probe spectroscopy (Fig. 3.1). This technique has the advantage to analyze the optical nonlinearities in a wide wavelength range. Furthermore, excitation beam at 500 Hz with pulse duration of 130 fs was utilized to avoid thermal effects.

3.2.2 Z-scan technique

As mentioned above, the evaluations of the $\chi_{eff}^{(3)}$, and rarely $\chi_m^{(3)}$, were often performed for single wavelengths only by means of Z-scan technique. This technique has the advantage of a simple experimental set-up using a single beam. A brief description of this technique is described here [51-52]. By using a focused laser beam, the transmission of a nonlinear sample is measured through an aperture. The transmission is recorded by scanning in the z-axis, starting from a distance away from the focus point (negative z) passing at focus point (z = 0) and finishes away from the focus point (positive z), see Figure 3.1. This technique is based on the spatial Gaussian

beam distortion as the sample is scanned in the z-axis. From the "open" and "closed" aperture data collections, the nonlinear absorption coefficient β and index of refraction γ are, respectively, obtained and can be written as

$$\alpha = \alpha_0 + \beta I \,, \tag{3.2a}$$

$$n = n_0 + \gamma I \,, \tag{3.2b}$$

where α_0 and n_0 are the linear absorption and refractive index. I is the intensity of the laser beam. The real and imaginary components of $\chi_{eff}^{(3)}$ are obtained through

$$\chi_{eff}^{(3)\prime} = 2n_0^2 \varepsilon_0 c\gamma \,, \tag{3.3a}$$

$$\chi_{eff}^{(3)\prime\prime} = \frac{n_0^2 \varepsilon_0 c^2}{\omega}\beta \,, \tag{3.3b}$$

where ε_0 is the permittivity of the vacuum, c is the speed of light in vacuum.

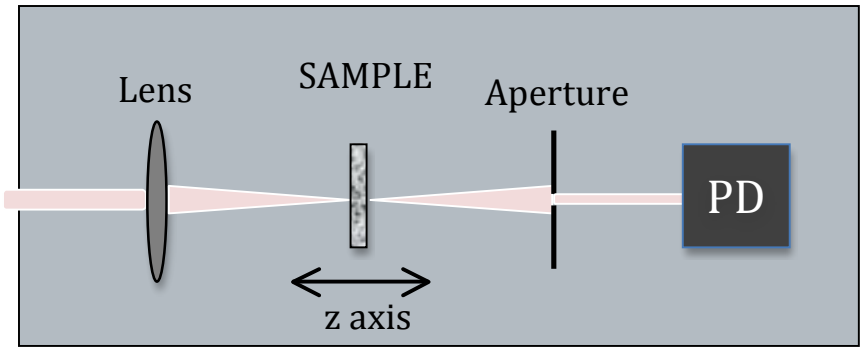

Figure 3.1: Schematic diagram of Z-scan technique.

3.2.3 Pump-and-probe spectroscopy method

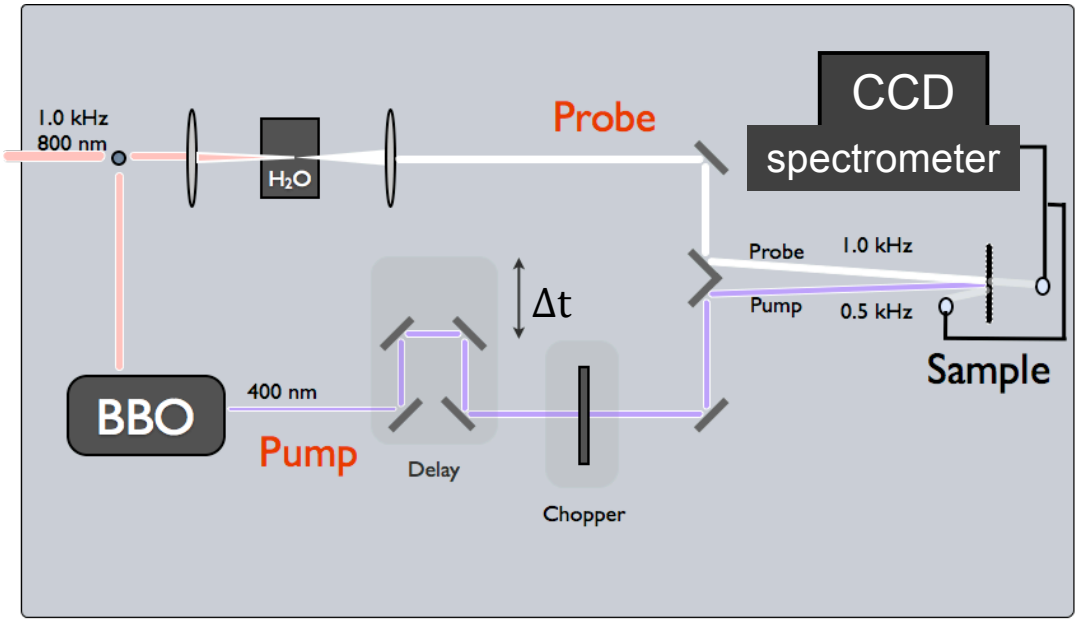

Figure 3.2: Schematic diagram of pump-and-probe spectroscopy.

Pump-and-probe spectroscopy uses two beams, so-called pump and probe. They were generated by a regenerative amplifier. In this system, 800-nm at 80-MHz pulses, generated by Millennia V and Tsunami (Spectra Physics), are trapped in a laser resonator cavity (Spitfire, Spectra Physics) with Ti:Al_2O_3 amplification medium. This medium was optically pumped by 527-nm pulses (Empower, Spectra Physics). These pulses are kept in the resonator by using a Pockels cell and a broadband polarizer. After extracting the energy stored in the cavity, the 800-nm fundamental beam at 1 KHz is extracted and equally divided into pump and probe beams [53].

The samples were excited by a pump-beam with wavelength and tunable intensity of 400 nm and 0.1-50 GW/cm^2, respectively. Pulse width and repetition of 130 fs and 500 Hz, respectively. These parameters were chosen to avoid optical nonlinearities of the samples by thermal effects. The

probe-beam was generated by focusing the fundamental beam into a water cell or CaF_2. The femtosecond white-light continuum was produced by a nonlinear process known as self-phase modulation [54]. After passing through the samples, the probe-beam was analyzed by a spectrometer and CCD camera. By modifying the pump-beam optical path, the delay between pump and probe beams was controlled for time resolved spectroscopy. Figure 3.2 shows the transient transmission changes $\Delta T/T$ of Ag NPs embedded in silica glass as a function of excitation intensity. At low excitation power, the optical nonlinearities are proportional to the excitation intensity. At higher intensity, nonlinear local field effects and higher nonlinear orders have to be considered. Here, the excitation intensity was selected at 0.6 GW/cm^2.

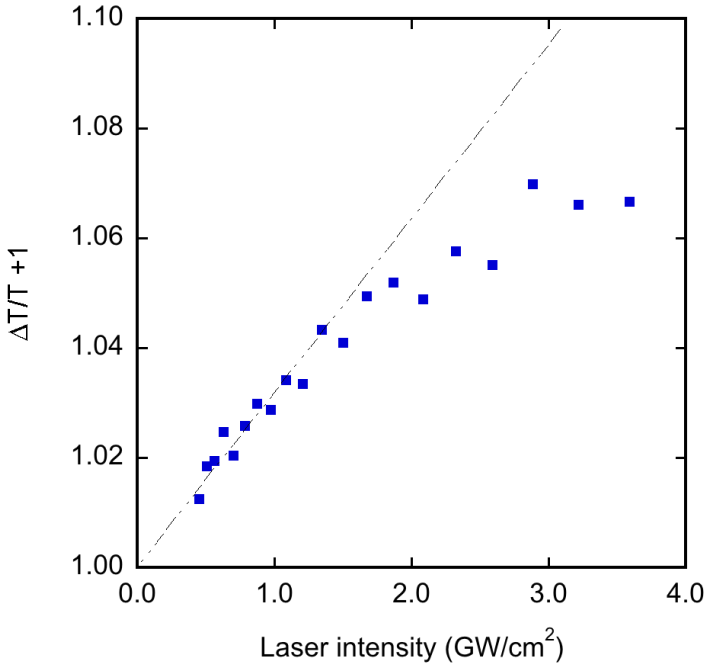

Figure 3.3: Transient transmission changes of Ag NPs embedded in silica glass as a function of excitation intensity.

The probe white-light continuum has a strong chirp due to the group velocity dispersion by the chosen nonlinear crystal [book, Femtosecond laser]. In this Chapter, a water cell was used to generate the white-light continuum. In Chapter 4 and 5, CaF_2 was selected to improve stability and intensity of the generated probe pulses. The group velocity dispersion was analyzed by measuring the nonlinearities of $SrTiO_3$ and properly corrected for the course of experiments. Figure 3.3 shows the probe beam chirp characteristics along with a polynomial fitting. It was observed that in the spectral range from 350 to 625 nm the continuum shifts nonlinearly 12 ps with time for CaF_2.

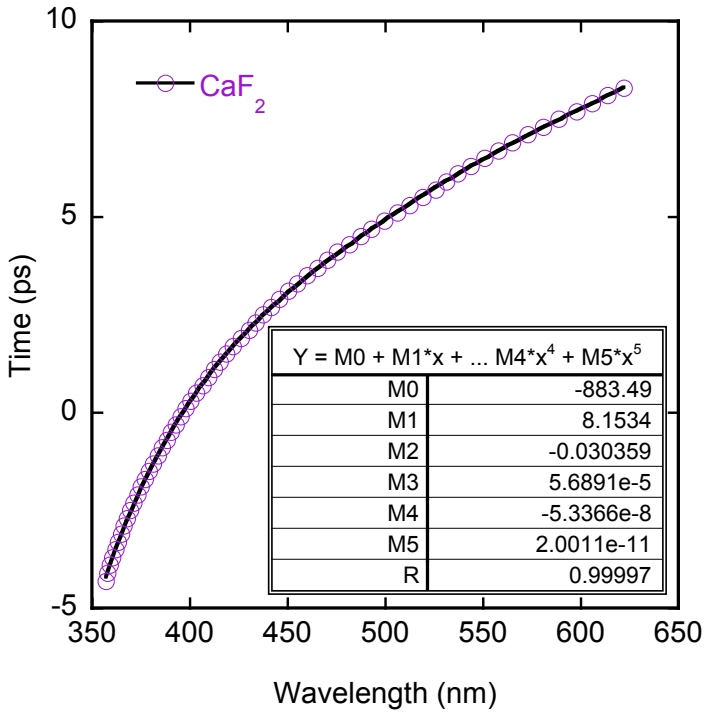

Figure 3.4: Group velocity delay of CaF_2 analyzed by measuring the optical nonlinearities of $SrTiO_3$.

3.2.4 Results

The time evolutions of $\Delta T/T$ and $\Delta R/R$ of 13-nm Ag nanoparticles embedded in silica glass at 3.07 and 3.04 eV, respectively, are shown in Figure 3.4. These time evolutions exhibit an exponential decay behavior due to the electron dynamics inside the metal particles after the laser excitation. The pump excitation creates an athermal electron distribution inside the metal particles. Electron-electron scattering redistributes the stored energy and attains a transient equilibrium. The intensity maximum of $\Delta T/T$ and $\Delta R/R$ in Figure 3.4 reflects this transient equilibrium stage. Subsequently, the cooling dynamics of the electrons into the lattice via electron-phonon interactions takes place within several tens of picoseconds [55].

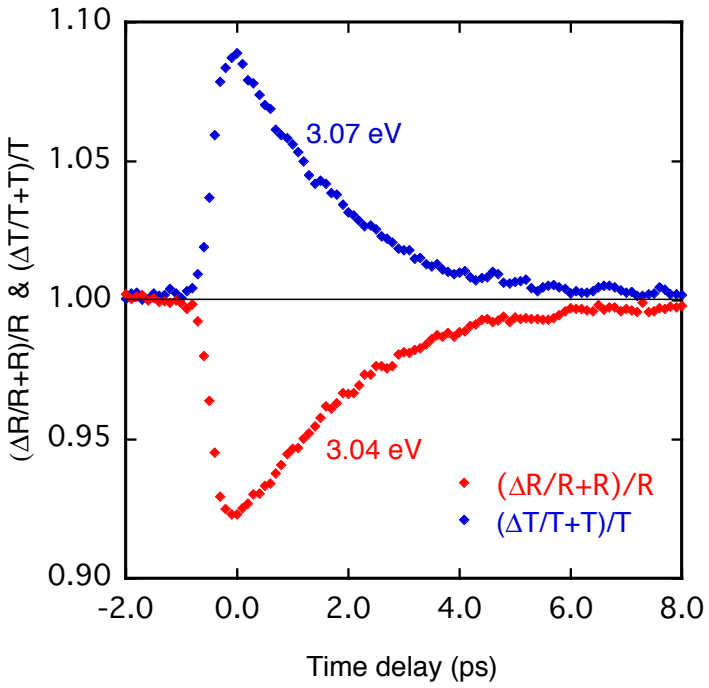

Figure 3.5: Time dependences of the transient transmission and reflection changes of 13-nm Ag NPs embedded in silica glass for different probe photon energies as labeled.

Figure 3.5 shows the dispersion of transient transmission and reflection changes of Ag nanoparticles embedded in silica glass right after the excitation pulse. The spectra show strong photon energy dependence. At the LSPR, $\Delta T/T$ and $\Delta R/R$ show a maximum of 1.07 and a minimum of 0.94, respectively. $\Delta T/T$ and $\Delta R/R$ reduce and increase at lower and higher photon energy relatively to the LSPR, respectively. These results were combined with those obtained from spectroscopic ellipsometry to evaluate the $\chi^{(3)}_{eff}$.

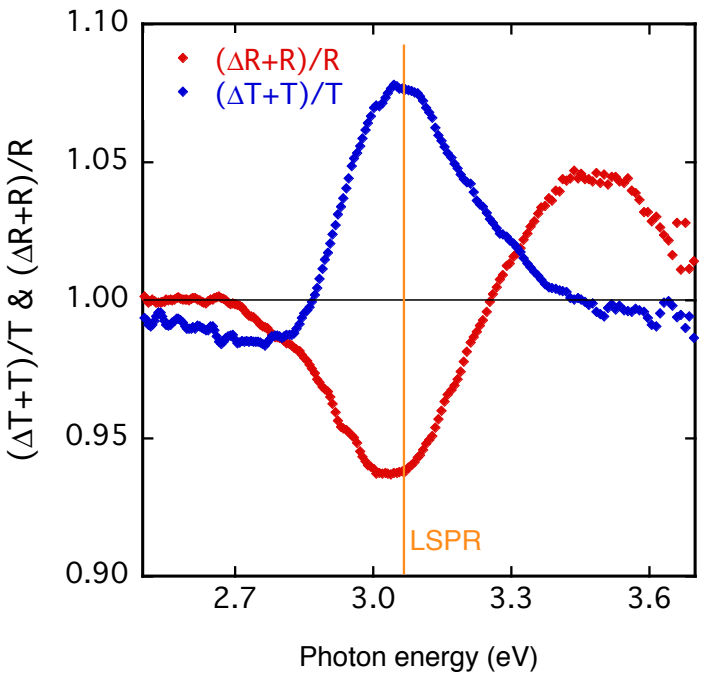

Figure 3.6: Transient transmission and reflection changes around the LSPR right after an excitation photon energy of 3.1 eV.

3.3 Third-order susceptibility of Ag nanoparticles

3.3.1 Experimental

By considering a weak-induced modification due to an excitation pulse, the modulation of the Ag nanoparticles composite's dielectric function was obtained by relating the transient transmission and reflection changes to the total differentiation [56,57]:

$$\frac{\Delta T}{T} = \frac{1}{T}\frac{\partial T}{\partial \varepsilon'_{eff}}\Delta\varepsilon'_{eff} + \frac{1}{T}\frac{\partial T}{\partial \varepsilon''_{eff}}\Delta\varepsilon''_{eff} \tag{3.2a}$$

$$\frac{\Delta R}{R} = \frac{1}{R}\frac{\partial R}{\partial \varepsilon'_{eff}}\Delta\varepsilon'_{eff} + \frac{1}{R}\frac{\partial R}{\partial \varepsilon''_{eff}}\Delta\varepsilon''_{eff}, \tag{3.2b}$$

where $\Delta\varepsilon'_{eff}$ and $\Delta\varepsilon''_{eff}$ are the real and imaginary components of the modulation of the Ag nanoparticles composite's dielectric function. The $\chi^{(3)}_{eff}$ was evaluated from $\Delta\varepsilon_{eff}$ and can be expressed as

$$\Delta\varepsilon = \tfrac{3}{4}\chi^{(3)}_{eff} I_0, \tag{3.3}$$

where 3/4 accounts for the intensity-dependent refractive index, K factor [13]. I_o is the pump peak irradiance. The partial differentials (Fig. 3.7) were numerically evaluated by using ε_{eff} obtained from ellipsometric analysis and shown in Figure 3.5.

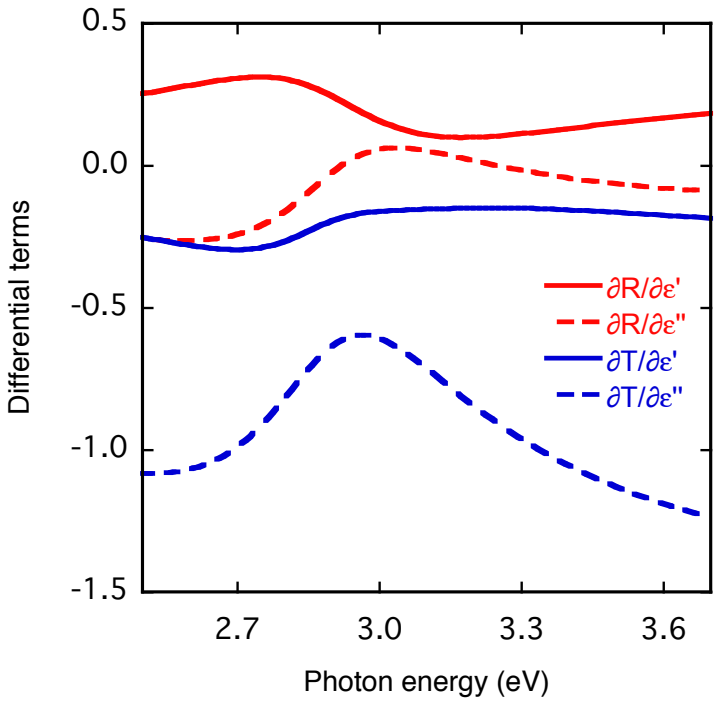

Figure 3.7: Differential terms of Ag nanoparticles embedded in silica glass numerically calculated.

Figure 3.8 shows the dispersion of the real and imaginary components of $\chi_{eff}^{(3)}$. The dispersions show strong photon energy dependence. At LSPR, the real and imaginary of $\chi_{eff}^{(3)}$ show a maximum of 0.9 x 10^{-17} m^2/V^2 and a minimum of -1.4 x 10^{-17} m^2/V^2, respectively.

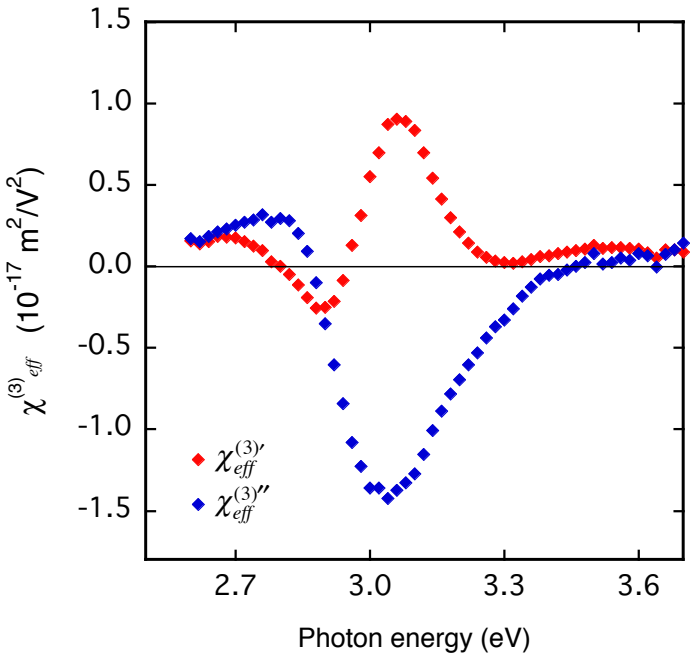

Figure 3.8: Real and imaginary components of the third order susceptibility of Ag nanoparticles embedded in silica glass. Applied electric field of 4.6 x 10^8 V/m.

3.3.2 Theoretical

To analyze the $\chi^{(3)}_{eff}$, $\Delta\varepsilon_{eff}$ was calculated under the Maxwell-Garnett effective medium approximation [50]:

$$\Delta\varepsilon_{eff} = \frac{(1+2p)\Delta\varepsilon_m + 2(1-p)\varepsilon_d}{(1-p)\Delta\varepsilon_m + (2+p)\varepsilon_d}, \tag{3.4}$$

where $\Delta\varepsilon_m$ is the modulation of the Ag particles' dielectric function, ε_d is the dielectric function of silica glass and p is the volume fraction of Ag nanoparticles in silica glass. For noble metals, $\Delta\varepsilon_m$ can be decomposed into free and bound electron components and calculated by using Drude model and first principal calculation, respectively [56]. For fitting the experimental

results, damping constant for free electrons and electron temperature of bound electrons were set at 3.6 x 10^{14} Hz and 600 K, respectively. Non-excited electron temperature was defined as 300 K. Figure 3.9 shows $\Delta\varepsilon_{eff}$ along with $\chi^{(3)}_{eff}$ for several volume fractions (Fig. 3.9a) and sizes (Fig. 3.9b) of Ag nanoparticles. Figure 3.10 shows the calculated $\chi^{(3)}_{eff}$ with volume fraction and nanoparticle size of 0.035 and 13 nm, respectively.

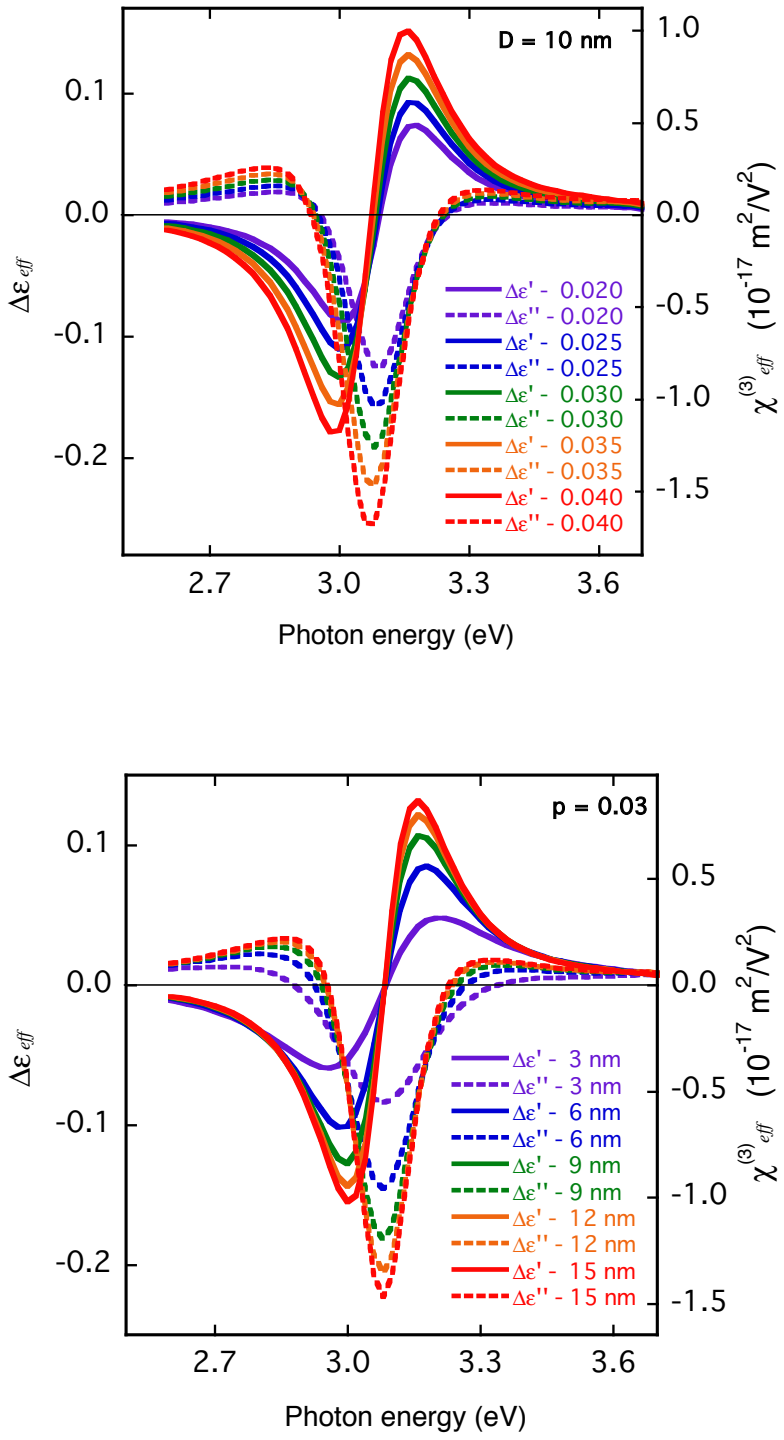

Figure 3.9: Calculated real and imaginary components of the modulation of dielectric function along with the third order susceptibility of Ag nanoparticles embedded in silica glass. Several a) volume fractions and b) sizes of Ag nanoparticles. Damping constant for free electrons and electron temperature of bound electrons were set at 3.6 x 10^{14} Hz and 600 K, respectively.

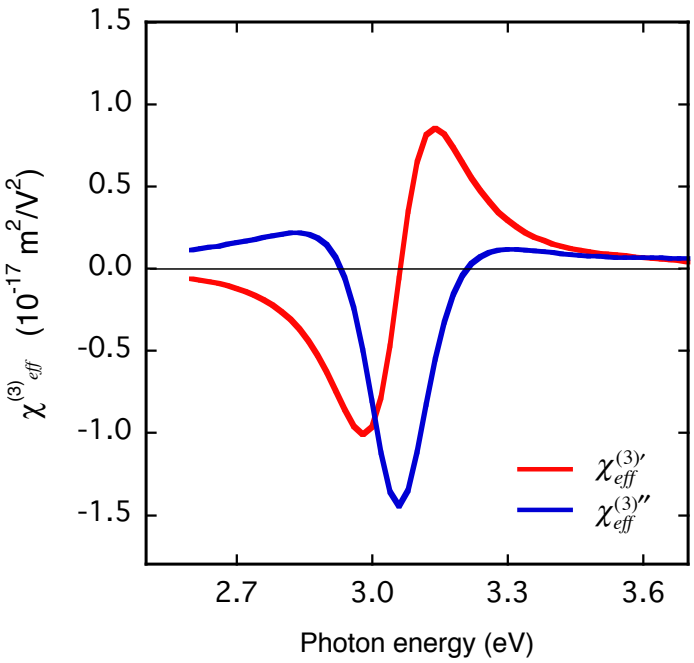

Figure 3.10: Calculated real and imaginary components of the third order susceptibility of Ag nanoparticles embedded in silica glass. Damping constant for free electrons and electron temperature of bound electrons were set at 3.6 x 10^{14} Hz and 600 K, respectively. D = 13 nm and $p = 0.035$.

3.3.3 Analysis

Overall dispersion of the experimental $\chi^{(3)}_{eff}$ (Fig. 3.8) can be explained by the classically calculated dispersion (Fig. 3.10). The experimental $\chi^{(3)}_{eff}$ shows a broader resonant structure in comparison to the calculated one. This broader structure reflects the linear optical properties. However, the asymmetric resonant structure of $\chi^{(3)\prime\prime}_{eff}$ most probably reflects the contribution of the dispersion of the intrinsic third-order susceptibility. Quantum finite-size effects and Fermi smearing play an important role in the intrinsic nonlinearity of metal nanoparticles. This will be discussed in details in the Chapter 4. Note that the intensity of the calculated dispersions

was fitted to experimental results. Therefore, intensity agreement to the experimental $\chi_{eff}^{(3)}$ cannot be discussed here.

Under Maxwell-Garnett approximation (Eq. 3.1), $\chi_{eff}^{(3)}$ is proportional to $f_l^2|f_l|^2$. The local field factor was discussed in the Chapter 1. Figure 3.11 shows the real and imaginary component of the calculated $f_l^2|f_l|^2$. Around the LSPR, the dispersion of $\chi_{eff}^{(3)}$ strongly reflects the local field factor due to the relative separation distance between the plasmon resonance and interband transition edge at 3.9 eV. This result suggests that the nonlinear optical properties of Ag nanoparticles are highly sensitive to the nanoparticle structure, including shape and size. By optimizing the Ag nanoparticle structure, we may control the internal local electric field via nonlinearity to favor specific applications. For instance, the dispersion of the $\chi_{eff}^{(3)}$ of Au and Cu nanoparticles do not directly reflect the local field factor due to the overlapping of interband transitions and LSPR.

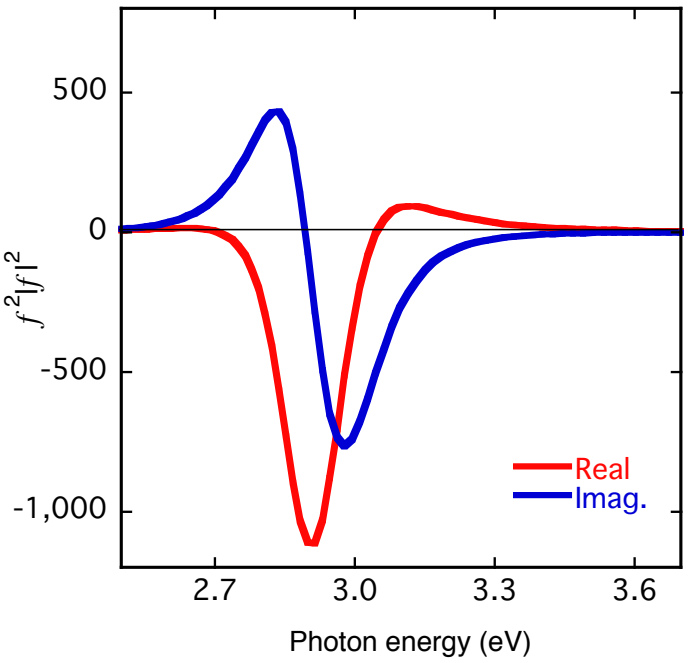

Figure 3.11: Calculated real and imaginary components of the forth power of the local field factor of Ag nanoparticles embedded in silica glass. D = 13 nm.

3.4 Chapter summary

I successfully evaluated the dispersion of the real and imaginary components of the effective third order susceptibility of Ag nanoparticles embedded in silica glass. This result was obtained by using pump-and-probe spectroscopy and spectroscopic ellipsometry.

By analyzing the dispersion of the optical nonlinearities of Ag nanoparticles, the contribution of the local field factor to the effective nonlinearity was discussed here. Around the LSPR, the dispersion of the third order susceptibility strongly reflects the local electric field

enhancement owing to the relative separation distance between the plasmon resonance and interband transition edge in contrast to other metal nanoparticles, i.e. Au and Cu. The discrepancy between the experimental and calculated dispersions at higher photon energy than the resonance peak is due to the contribution of the intrinsic nonlinearity dispersion of the Ag nanoparticles and will be discussed in the next Chapter.

Chapter 4

Size dependence of NLO properties of Ag nanoparticles

4.1 Introduction

Metal metamaterials have attracted great attention. Owing to the plasmonic excitation, these materials are applied to solar cell [58], surface enhanced Raman spectroscopy (SERS) [59], and biosensor devices [60]. Its enhanced optical nonlinearities and ultrafast response have potential application in nanophotonics devices, including ultrafast all-optical signal processing and switches, wavelength tuning of lasers, and second- and third-harmonic generation [61-65]. However, these hoped-for applications are yet to be realized [66]. Basic concepts need to be understood to advance the functional concepts toward applications. Despite the effort and great interest in metal nanoparticles, quantum finite-size effects in the nonlinear optical properties remain poorly understood.

Size dependence in the linear optical properties has been experimentally and theoretically characterized. Experimentally, Ag nanoparticles show a substantial plasmon resonance blueshift of 0.5 eV with decreasing particle size

from 20 to 1.7 nm. Based on a theory of quantum finite-size effects, the discretization of the electrons leads to a strong modification of the Ag particle permittivity as the particle size enters the quantum regime. The observed blueshift was attributed to the discretization of conduction electrons inside the nanoparticle [26].

Optical nonlinearities of metal nanoparticles have been often investigated at single photon energy by means of Z-scan [51], degenerate four-wave mixing (DFWM) [27], and pump-and-probe methods. Measurement at single photon energy restricts the understanding of the nonlinear mechanisms. Nonlinear optical properties of metal nanoparticles are also expected to show quantum finite-size effects. However, Uchida *et al.* [27] concluded by using nanosecond DFWM that $\chi_m^{(3)}$ of Ag nanoparticles are almost independent of particle size in the range of 4.2 to 31 nm. Conversely, based on a theory of quantum finite-size effects, numerical and analytical calculations have yielded predictions of strong size and spectral dependencies of $\chi_m^{(3)}$ [29].

In this Chapter, I have systematically investigated the size dependence in the nonlinear optical properties of 3.0-16-nm-size Ag nanoparticles in SiO_2. Samples description and linear optical properties were discussed in Chapter 2. Nonlinear optical properties were evaluated by using spectroscopic ellipsometry and pump-and-probe spectroscopy methods. The nonlinear mechanisms to $\chi_{eff}^{(3)}$ and $\chi_m^{(3)}$ are discussed here in details. Optical nonlinearities of Ag nanoparticles show strong quantum finite-size effects leading to a substantial increase of $\chi_m^{(3)}$ for particle sizes into the quantum regime.

4.2 Third-order susceptibility of Ag nanoparticles

4.2.1 Pump-and-probe spectroscopy: white-light continuum generation

In this and following Chapter, the probe-beam white-light continuum was generated by focusing the fundamental beam into CaF_2. The water cell was substituted by this crystal to improve stability and intensity of the generated probe pulses in the vicinity of LSPR of Ag nanoparticles. Figure 4.1 shows the spectral range of white-light continua in various condensed media [54].

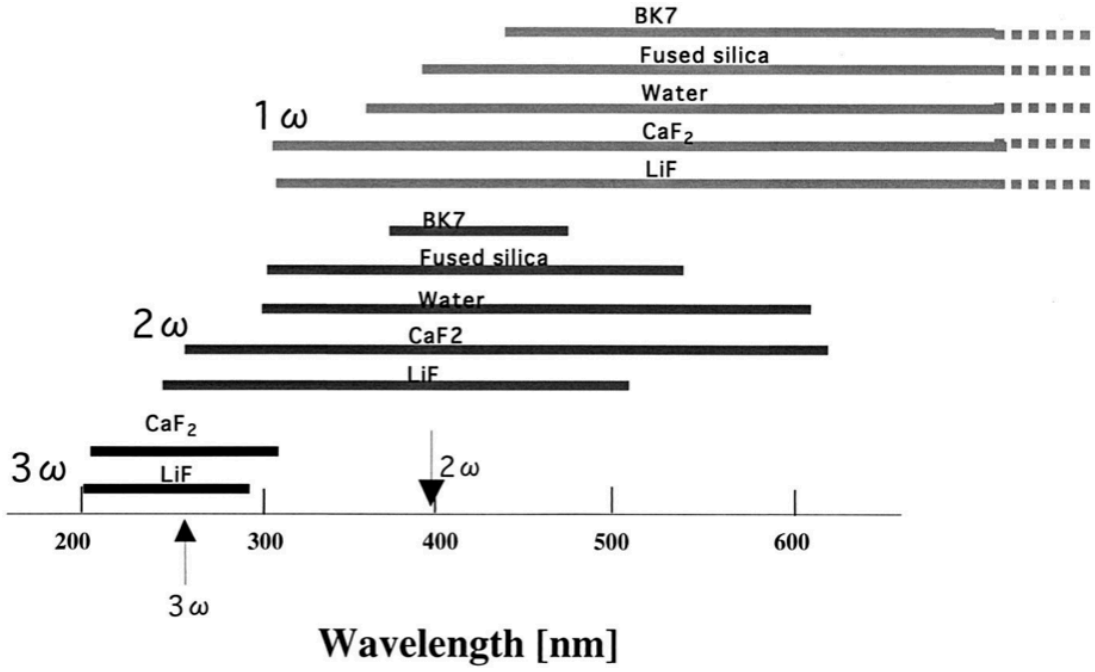

Figure 4.1: Spectral range of white-light continua for three incident wavelengths, 262 (3ω), 393 (2ω) and 785 nm (1ω) [54].

4.2.2 Transient transmission changes

The dispersion of $\Delta T/T$ was measured by using a femtosecond pump-and-probe spectroscopy. The samples were exited at 0.5 kHz with pulse duration and photon energy of 130 fs and 3.1 eV, respectively. Peak power density and focal size of 5.1 MW/mm^2 and 0.2 mm, respectively. These parameters were chosen to avoid thermal effects and higher-order nonlinearities. Excitation intensity and $\Delta T/T$ was confirmed linear up to 15 MW/mm^2. Figure 4.2 shows the dispersion of $\Delta T/T$ of Ag nanoparticles in SiO_2 with average particle sizes ranging from 3.0 to 16 nm. The observed $\Delta T/T$ peak around the LSPR exhibits a maximum at 13 nm. This peak shows a blueshift from 3.08 to 3.17 eV with decreasing particle size.

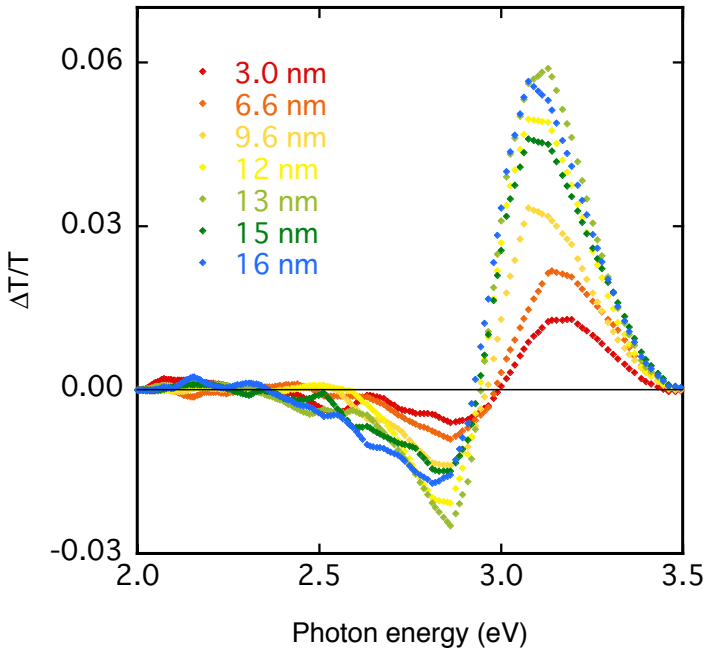

Figure 4.2: Dispersion of the transient transmission changes $\Delta T/T$ of Ag nanoparticles in SiO_2 with average particles sizes ranging from 3.0 to 16 nm as labeled. Right after the excitation pulse at 3.1 eV.

4.2.3 Evaluation of effective and intrinsic third-order susceptibility

In this Chapter, $\chi^{(3)}$ was evaluated by combining ΔT and T from pump-and-probe spectroscopy and spectroscopic ellipsometry respectively. First, the ellipsometric model was evaluated from the experimental quantities $\Psi(\omega)$ and $\Delta(\omega)$, details in Chapter 2. From this model, T of the Ag nanoparticles layer (EMA layer) was obtained. At excitation condition ($\Delta T + T$), the ellipsometric model was re-evaluated by considering a weak-induced modification due to the pump pulse. This re-evaluation was performed by fitting the transmission at excitation condition through the oscillators' parameters of Ag nanoparticles while keeping the structural parameters and substrate optical constants fixed. The transmission of 13-nm-diameter Ag nanoparticles at excitation condition along with steady state is shown in Figure 4.3. One can observe that the transmission is increased at the LSPR. From this fitting, we extracted the modulation of the dielectric function of EMA layer ($\varepsilon_{eff} + \Delta\varepsilon_{eff}$) and Ag nanoparticles ($\varepsilon_m + \Delta\varepsilon_m$). For a 13-nm-diameter Ag nanoparticles, $\varepsilon_m + \Delta\varepsilon_m$ along with steady state is shown in Figure 4.4.

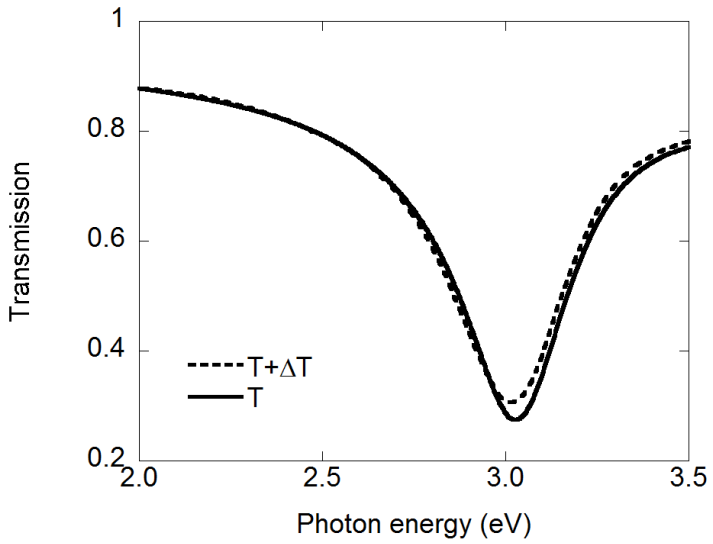

Figure 4.3: Transmission of 13-nm-diameter Ag nanoparticles at excitation condition along with steady state.

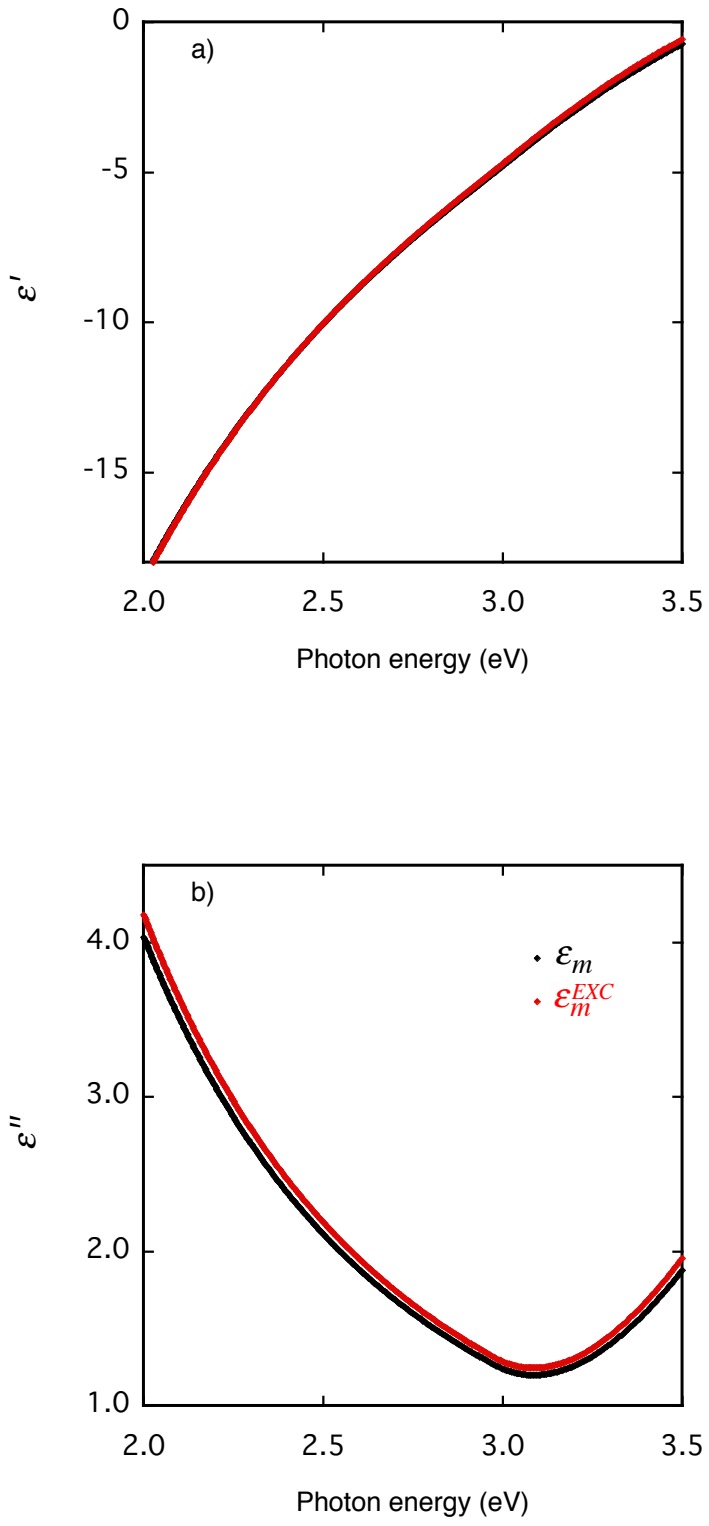

Figure 4.4: a) Real and b) imaginary components of the dielectric function of 13-nm-diameter Ag nanoparticles at excitation ($\varepsilon_m^{EXC} = \varepsilon + \Delta\varepsilon$) along with steady state condition.

4.3 Size dependence of the third-order susceptibility

4.3.1 Effective third-order susceptibility

From $\Delta\varepsilon_{eff}$, the effective $\chi^{(3)}_{eff}$ was evaluated and can be expressed as

$$\Delta\varepsilon_{eff}(\omega_{probe}) = \tfrac{3}{4}\chi^{(3)}_{eff}(\omega_{probe})I_0\,, \tag{4.1}$$

where I_0 is the excitation peak irradiance and 3/4 is the K factor for intensity-dependent refractive index.

The dispersion of the real and imaginary components of $\chi^{(3)}_{eff}$ of Ag nanoparticle's composite is shown in Figure 4.5. These components show the resonant structure blueshift with decreasing particle size. The real component minimum decreases for particle size decreasing from 16 to 3.0 nm from -7.9 to -0.6 x 10^{-17} m^2/V^2. The maximum also decreases from 2.7 to 0.2 x 10^{-17} m^2/V^2. The imaginary component minimum decreases for particle size decreasing from 16 to 3.0 nm from -7.9 to -0.8 x 10^{-17} m^2/V^2. The maximum also decreases from 2.8 x 10^{-17} to 0.8 x 10^{-18} m^2/V^2. $\left|\chi^{(3)}_{eff}\right|$ presents narrower spectral shape in comparison to the linear LSPR (Figure 2.6) due to the higher-order process as shown in Figure 4.6. As discussed in Chapter 2, the size dependence of the linear optical properties is dictated by the square of the local field and imaginary component of the dielectric function of the Ag particles. From ellipsometric results of $\chi^{(3)}_{eff}$, the size dependence of the nonlinear optical properties is dictated by the forth power of the local field and $\chi^{(3)}_{m}$.

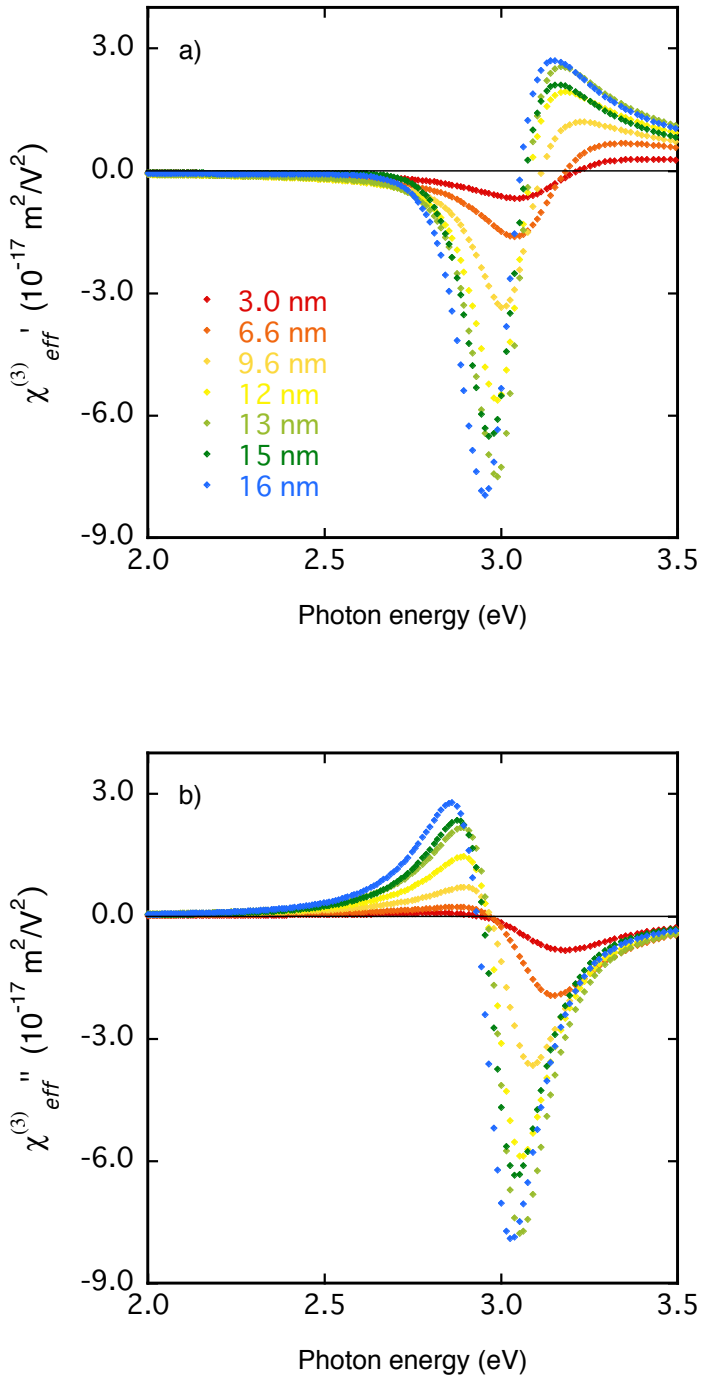

Figure 4.5: a) Real and b) imaginary components of the third-order susceptibility $\chi^{(3)}_{eff}$ of Ag nanoparticles in SiO_2 with average particles sizes ranging from 3.0 to 16 nm as labeled.

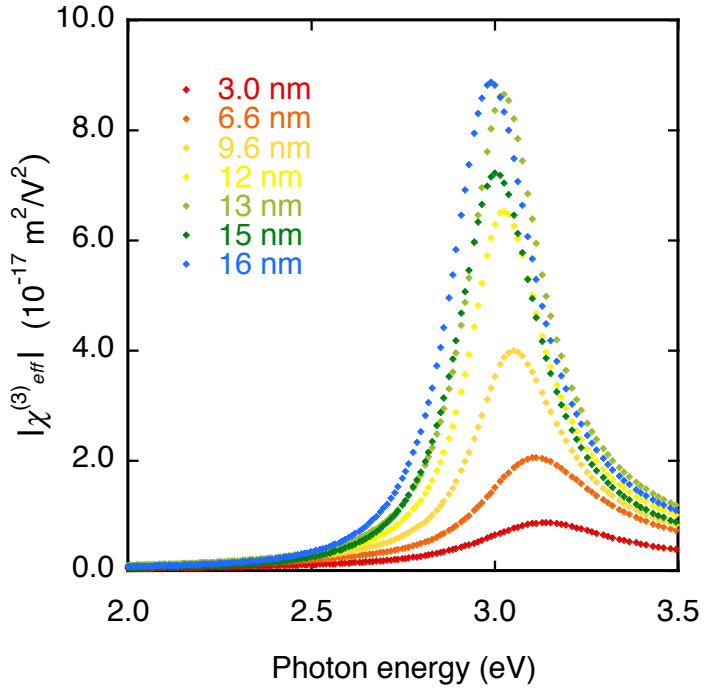

Figure 4.6: Third-order susceptibility $\left|\chi^{(3)}_{eff}\right|$ of Ag nanoparticles in SiO_2 with average particles sizes ranging from 3.0 to 16 nm as labeled.

4.3.2 Intrinsic third-order susceptibility

Under Maxwell-Garnett EMA, $\chi^{(3)}_{eff}$ is dictated by the forth power of the local field and $\chi^{(3)}_{m}$. To illustrate the size dependence of the nonlinear optical properties to $f_l^2|f_l|^2$ and $\chi^{(3)}_{m}$, $\left|\chi^{(3)}_{eff}\right|/\alpha$ and $\left|pf_l^2|f_l|^2\right|/\alpha$ as a function of the particle size are shown in Figure 4.7. They were divided by the linear absorption coefficient to eliminate the Ag volume fraction contribution. The intensity tendency of $\left|\chi^{(3)}_{eff}\right|/\alpha$ in respect to the Ag particle sizes ranging from 3.0 to 16 nm cannot be reproduced by the forth power of the local field. This result indicates that $\chi^{(3)}_{m}$ also presents size dependence. Conversely, by using DFWM with a 7 ns pulse width, Uchida *et al.* [27] showed that $\chi^{(3)}_{m}$ is roughly independent of the Ag particle sizes ranging from 4.2 to 31 nm (Table 4.1).

Magruder III *at al.* measured Cu nanoparticles by using two laser pulse durations of 6 and 100 ps. From the Z-scan results, these authors concluded that the optical nonlinearities by using pulse durations of 6 and 100 ps are predominantly due to electronic and thermo-optic effects, respectively. For this reason, the results of $\chi_m^{(3)}$ investigated by Uchida *et al.* are predominantly due to thermo-optic contribution owing to the nanosecond pulse width. Therefore, the size and spectral dependence of $\chi_m^{(3)}$ significantly determine the optical nonlinearities of Ag nanoparticle's composite. From ellipsometric results $\Delta\varepsilon_m$, $\chi_m^{(3)}$ was evaluated and can be expressed as

$$\Delta\varepsilon_m(\omega_{probe}) = \tfrac{3}{4}\chi_m^{(3)}(\omega_{probe})\left|f_l(\omega_{pump})\right|^2 I_0, \qquad (4.2)$$

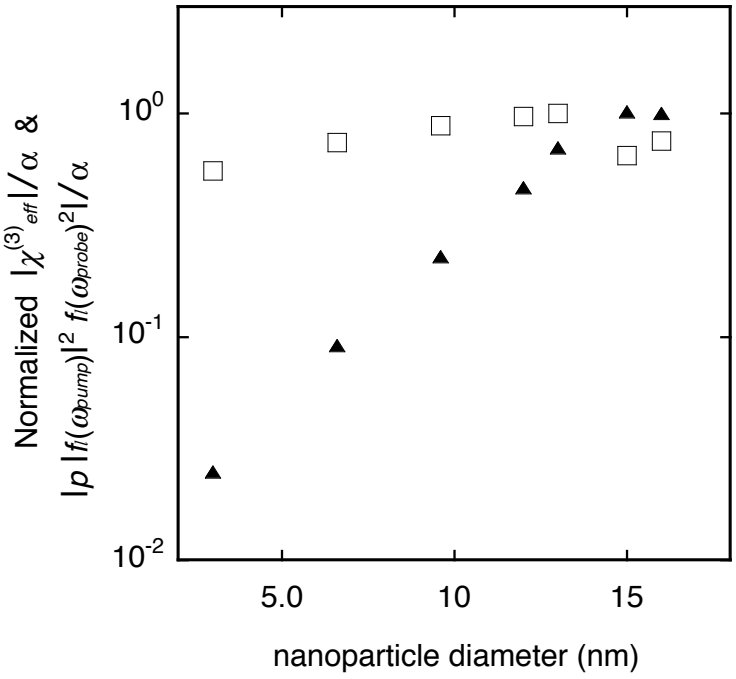

Figure 4.7: Normalized $\left|\chi_{eff}^{(3)}\right|/\alpha$ (□) and $\left|pf_l^2\left|f_l\right|^2\right|/\alpha$ (▲) as a function of the Ag particle size.

Table 4.1: Parameters of Ag nanoparticles embedded in glass, radius ranging from 2.1 to 15.3 nm [27].

Radius R (nm)	Absorption Coefficient α (cm^{-1})	Dielectric Constant ϵ_m''	Local-Field Factor f_i	Volume Fraction p (10^{-5})	Nonlinearity $\chi^{(3)}$ (esu)	$\chi^{(3)}/\alpha$ (esu cm)	$\chi_m^{(3)}$ (esu)
2.1	544	1.557	4.958	15.1	3.1×10^{-10}	5.9×10^{-13}	3.35×10^{-9}
3.0	1414	1.176	6.674	30.0	1.3×10^{-9}	9.3×10^{-13}	2.94×10^{-9}
3.3	1729	1.083	7.295	33.5	3.6×10^{-9}	2.1×10^{-12}	3.78×10^{-9}
4.0	40	0.934	8.502	0.7	1.2×10^{-10}	2.9×10^{-12}	3.34×10^{-9}
4.9	3432	0.804	9.914	48.4	1.2×10^{-8}	3.6×10^{-12}	2.61×10^{-9}
5.2	2595	0.771	10.346	35.1	1.1×10^{-8}	4.3×10^{-12}	2.79×10^{-9}
5.4	197	0.751	10.628	2.6	1.1×10^{-9}	5.8×10^{-12}	3.45×10^{-9}
5.7	1783	0.723	11.046	22.5	1.3×10^{-8}	7.2×10^{-12}	3.82×10^{-9}
6.0	2246	0.698	11.448	27.3	1.8×10^{-8}	8.2×10^{-12}	3.91×10^{-9}
6.4	2061	0.673	11.880	24.2	1.9×10^{-8}	9.2×10^{-12}	3.92×10^{-9}
8.8	2731	0.548	14.762	25.6	3.3×10^{-8}	1.2×10^{-11}	2.68×10^{-9}
10.4	3188	0.498	16.407	26.6	4.4×10^{-8}	1.4×10^{-11}	2.28×10^{-9}
10.9	3455	0.485	17.010	27.7	7.6×10^{-8}	2.2×10^{-11}	3.29×10^{-9}
11.3	2379	0.476	17.335	18.7	6.1×10^{-8}	2.6×10^{-11}	3.61×10^{-9}
12.1	3249	0.459	18.225	24.0	1.1×10^{-7}	3.4×10^{-11}	4.15×10^{-9}
13.0	2032	0.441	19.412	13.9	6.2×10^{-8}	3.0×10^{-11}	3.14×10^{-9}
15.3	1678	0.404	22.381	9.5	4.6×10^{-8}	2.7×10^{-11}	1.90×10^{-9}

Figure 4.8 shows the absolute component of $\left|\chi_m^{(3)}\right|$ of Ag nanoparticle with average particle sizes ranging from 3.0 to 16 nm. $\left|\chi_m^{(3)}\right|$ (Fig. 4.8a) shows strong intensity increase with decreasing Ag particle size. To understand the intrinsic optical nonlinearities, a theory of quantum finite-size effects in metal nanoparticles developed by Rautian [67] will be discussed next.

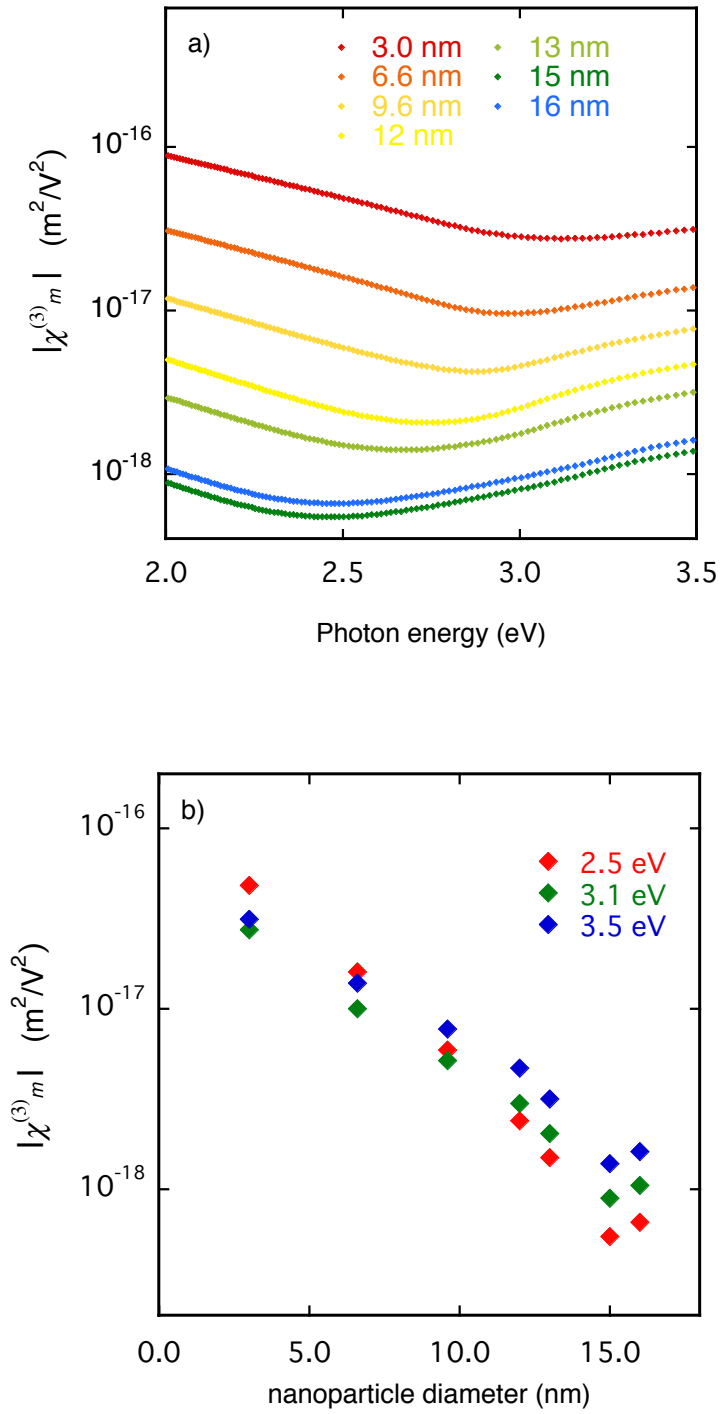

Figure 4.8: a) Absolute component of the intrinsic third-order susceptibility $\left|\chi_m^{(3)}\right|$ of Ag nanoparticle with average particle sizes ranging from 3.0 to 16 nm as labeled. b) Absolute component of $\left|\chi_m^{(3)}\right|$ of Ag nanoparticle in respect to nanoparticle diameter at 2.5, 3.1 and 3.5 eV.

Rautian's model of metal nanoparticles [67] considers the conduction electrons inside the nanoparticle as a free-electron gas. These electrons are considered to be in an infinite spherical potential well. The model does not consider particle surface roughness and electron-electron interaction. Rautian's analytical model assumes two dominant contributions to $\chi_m^{(3)}$. The nonresonant $\chi_{mn}^{(3)}$ and resonant $\chi_{mr}^{(3)}$ contributions can be expressed as

$$\chi_{mn}^{(3)} = \frac{2}{15}\left(\frac{e^2 n}{m\omega^2}\right)\left(\frac{ea}{\hbar\omega}\right)^2 \frac{\Gamma_2}{\Gamma_1}\left[1 - i\frac{2\Gamma_2}{\omega}\right]F_3 , \tag{4.3a}$$

$$\chi_{mr}^{(3)} = -i\frac{2}{15}\left(\frac{e^2 n}{m\omega^2}\right)\left(\frac{ea}{\hbar\omega}\right)^2 \frac{\Gamma_2}{\Gamma_1}\left(\frac{\omega}{2\Gamma_2}\right)^2\left(\frac{\delta_F}{\hbar\omega}\right)^5 g_3 , \tag{4.3b}$$

where e is the electron charge, n is the electron density, m is the electron mass, a is the particle radius, Γ_1 and Γ_2 are the relaxation rates for population and coherence, respectively. g_3 and F_3 are the integration over resonant states and summation of nonresonant terms near the Fermi energy E_F. The parameters g_3 and F_3 are considered weakly size dependent. $\delta_F = 2\sqrt{E_F E_0}$, where $E_0 = \hbar^2/2ma^2$.

The $\chi_{mn}^{(3)}$ contribution accounts for the interactions of the excitation electric field with E_F electrons. $\chi_{mr}^{(3)}$ accounts for conduction electron transitions between discrete states, that is, quantum finite-size effects. By reducing the number of nested summations from eight to five, Govyadinov *et al.* [29] developed the theory of Rautian a step further without additional approximations. The developed equations are amenable to numerical calculation. These authors plotted the numerical and analytical calculations of the $\left|\chi_m^{(3)}\right|$ of an Ag nanoparticle in respect to its size (Figure 4.9). For a $<$ 4 nm, the sharp maxima and minima are due to the quantum finite-size effects.

These sharp lines are artifacts created by the numerical calculation at zero-temperature. Figure 4.9 inset shows the calculation at 300 K. At a finite temperature, the discontinuities are eliminated but do not remove the fine structure of the dispersion. Numerically, the calculations were carried out with a fine step in size of 0.41 nm that is the Ag lattice constant. Experimentally, this fine structure is unlikely to be observable owing to the particles size distribution. For 4 nm $<$ a $<$ 8 nm, the discrepancy between the numerical and analytical calculations are described as from unknown origins [29]. $\chi_m^{(3)}$ has the predominant contribution of $\chi_{mn}^{(3)}$ and $\chi_{mr}^{(3)}$ for bigger and smaller nanoparticles, respectively. $\chi_{mn}^{(3)}$ and $\chi_{mr}^{(3)}$ show dependence on the particle size of a^2 and a^{-3}, respectively. For this reason, $\chi_m^{(3)}$ shows a minimum value in respect to the particle size (Figure 4.9). The critical particle size, where $\left|\chi_m^{(3)}\right|$ has the minimum value, is defined by Γ_2. By using $\Gamma_2 = \gamma_\infty / 2$ where $\gamma_\infty = 70$ cm^{-1} is the relaxation constant of bulk Ag, the critical particle diameter is 8 nm (Figure 4.10).

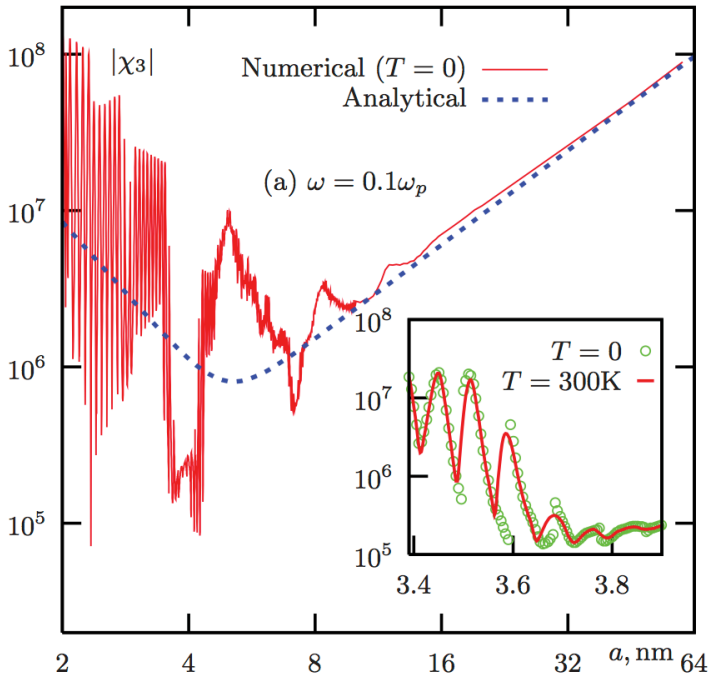

Figure 4.9: Absolute component of the intrinsic third-order susceptibility of an Ag nanoparticle in respect to its size. $\omega = 0.9$ eV.
In the inset, results at T = 0 and at T = 300 K [29].

The obtained experimental results of $\left|\chi_m^{(3)}\right|$ of Ag particles also show a minimum in respect to the particle size (Figure 4.8). Due to the nonresonant contribution, $\left|\chi_m^{(3)}\right|$ strongly increases with decreasing Ag particle size from 15 to 3.0 nm. The resonant contribution appears from particle size of 15 nm. However, for the experimental results the $\left|\chi_m^{(3)}\right|$ minimum appears at particle size of 15 nm. This result suggests that the Ag nanoparticle Γ_2 is reduced with decreasing particle size. Γ_2 has to be clarified to better understand the critical particle size in the results obtained by using quantum finite-size theory.

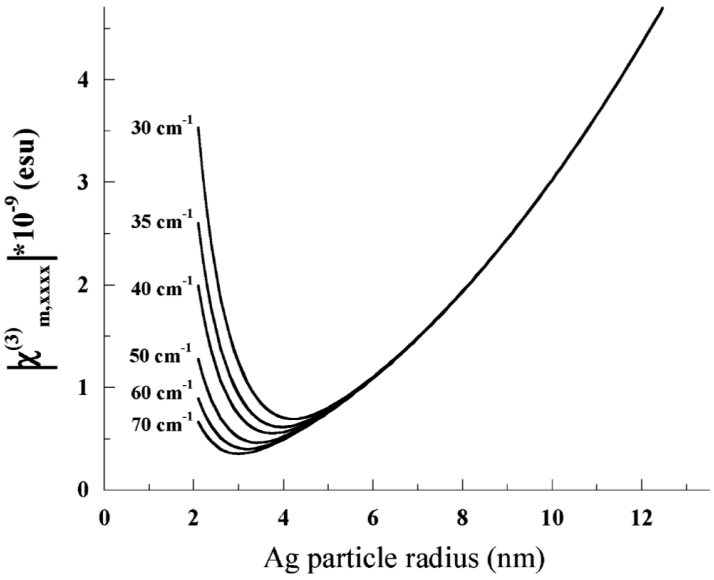

Figure 4.10: Absolute component of the intrinsic third-order susceptibility of an Ag nanoparticle in respect to its size. At fixed ratio of $\Gamma_2/\Gamma_1 = 10$ and various values of Γ_2 as labeled [33].

The real and imaginary components of $\chi_m^{(3)}$ show strong spectral and size dependence. To understand the real and imaginary components of $\chi_m^{(3)}$, the dielectric function of Ag nanoparticles ε_m calculated by using a theory of quantum finite-size effects in metal nanoparticles will be discussed next [26].

The ε_m of Ag nanoparticles can be described as

$$\varepsilon_m = \varepsilon_{mfree} + \varepsilon_{m\_IB}, \tag{4.4}$$

where ε_{mfree} is the contribution of intraband transitions and ε_{m_IB} the interband transitions. Classically, the ε_{mfree} is described by the Drude model as [26]

$$\varepsilon_{mfree} = 1 - \frac{\omega_p^2}{\omega(\omega + i\gamma)}, \tag{4.5}$$

where ω_p is the plasma frequency. For small nanoparticles, quantum finite-size effects should also be considered. To account for these effects, the conduction electrons were modeled as a free electron gas in an infinite spherical potential well. By using Drude model and defining the Lorentzian terms with quantum effects, ε_{mfree} can be defined as [26]

$$\varepsilon_{mfree} = \omega_p^2 \sum_i \sum_f \frac{S_{if}}{\omega_{if}^2 - \omega^2 - i\gamma\omega}, \tag{4.6}$$

where $\omega_{if} = \left(E_f - E_i\right)/\hbar$ is the allowed transition frequency from an occupied state i to an unoccupied state f and S_{if} is the oscillator strength of each transition frequency. The energy level in a spherical potential well is defined as

$$E = \frac{\hbar^2 \pi^2}{8Ma^2}(2n + l + 2)^2, \tag{4.7}$$

where M is the electron mass and n and l are the quantum numbers. By using the equation (4.6) and (4.7), the real and imaginary components of ε_{mfree} were calculated and shown in Figure 4.11.

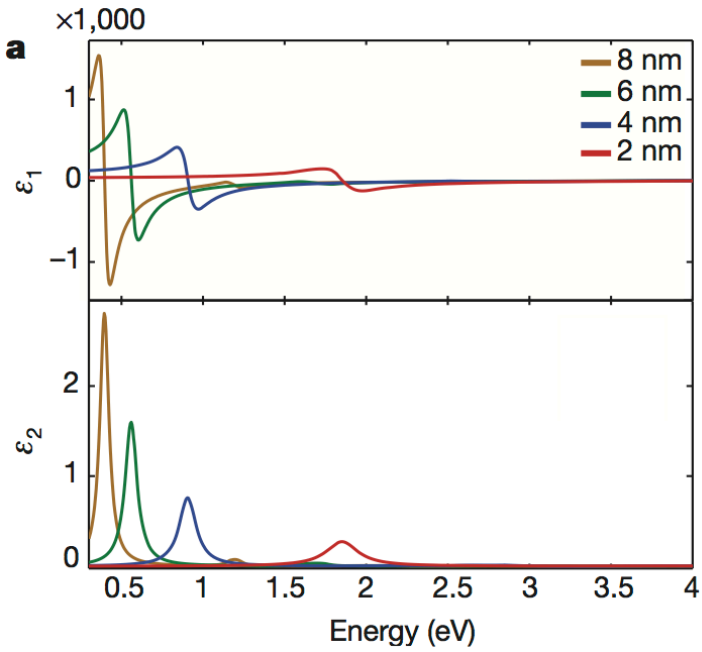

Figure 4.11: Real and imaginary components of the dielectric function of an Ag nanoparticle with particle diameter ranging from 2 to 8 nm as labeled [26].

In Figure 4.12(a), the real component $\chi_m^{(3)\prime}$ shows negative and positive values at lower and higher photon energies, respectively. $\chi_m^{(3)\prime}$ presents a signal changeover shift from 2.2 to 3.1 eV with the particle size decrease from 16 to 3.0 nm. As the particle size decreases, the calculated linear ε_m' (Figure 4.11) shows the conduction-electron transitions shifting toward the visible spectrum owing to the discretization of the electron transitions defined by Equation (4.7). The signal changeover blueshift of $\chi_m^{(3)\prime}$ also reflects the discretization of the electron transitions as the particle size decreases.

In Figure 4.12(b), the imaginary component $\chi_m^{(3)\prime\prime}$ shows a strong intensity increase as the particle decreases due to the discretization of the electron transitions. The dispersion of $\chi_m^{(3)\prime\prime}$ shows a minimum redshift and is

flattened as the particle size decreases. This minimum is most certainly owing to the contribution of intraband and interband at lower and higher photon energies, respectively. We note that the calculations of linear and nonlinear optical properties of Ag particles do not consider the interband transitions [26,29]. The linear ε_m'' obtained by ellipsometric results shows a minimum due to the intraband and interband transitions. Similarly to $\chi_m^{(3)''}$, this minimum redshifts as the particle size decreases. The dispersion flattened and minimum at higher photon energy of $\chi_m^{(3)''}$ compared to ε_m'' indicate that intraband transitions dominate the optical nonlinearities around the LSPR for smaller nanoparticles. This increased contribution of the conduction electrons can be explained by the increase of allowed electron transitions in the LSPR region due to quantum finite-size effects.

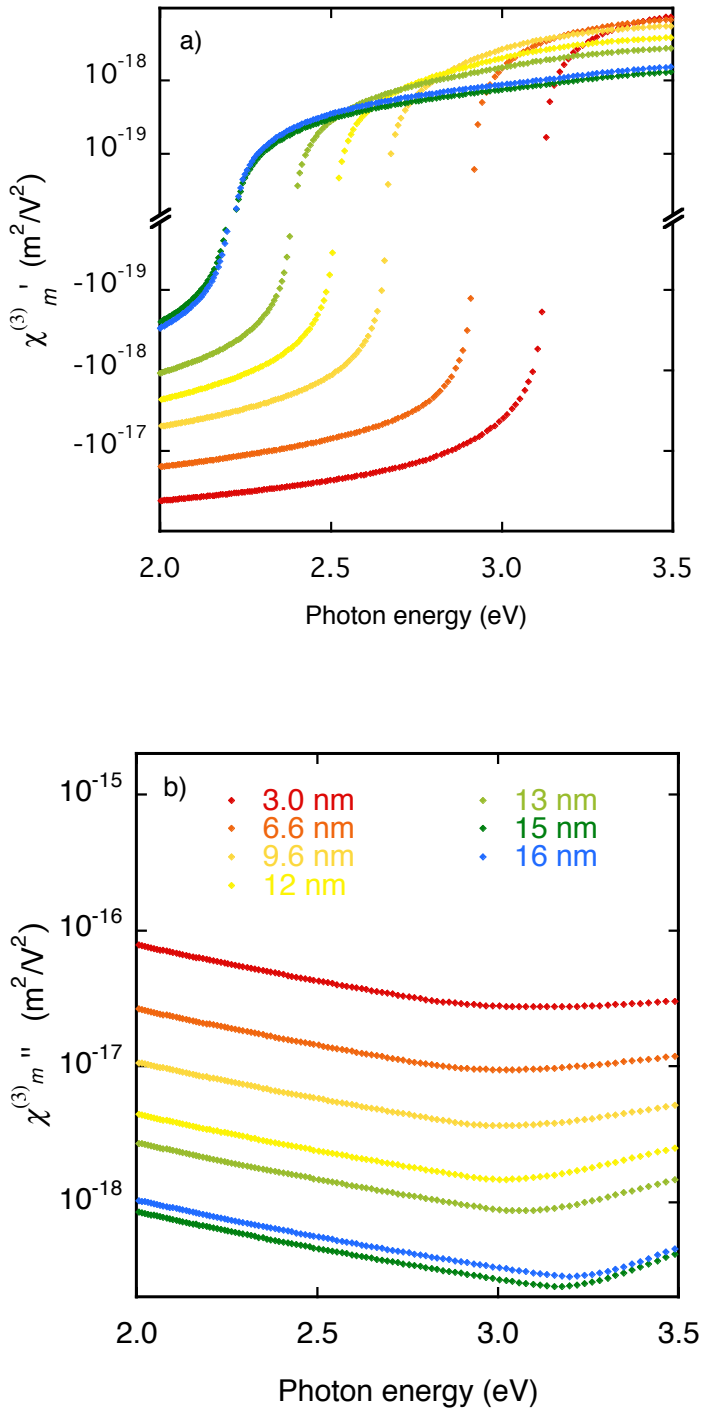

Figure 4.12: a) Real and b) imaginary components of the intrinsic third-order susceptibility $\chi_m^{(3)}$ of Ag nanoparticles with average particle sizes ranging from 3.0 to 16 nm as labeled.

4.4 Chapter summary

In this Chapter, the particle size dependence of $\chi_m^{(3)}$ of Ag nanoparticles was investigated by using spectroscopic ellipsometry and spectroscopy pump-and-probe. From the experimental results, I showed a strong intensity increase in $\left|\chi_m^{(3)}\right|$ as the Ag nanoparticles diameter decreases from 15 to 3.0 nm. The $\chi_m^{(3)\prime}$ and $\chi_m^{(3)\prime\prime}$ show spectral dependence in the vicinity of the LSPR. This spectral dependence is increased as the Ag nanoparticles decrease. The intensity and spectral dependence of $\chi_m^{(3)}$ mostly reflect the discretization of the electron transitions owing to the quantum finite-size effects. The critical Ag particle size for the quantum effects was found at 15 nm. The experimental results of $\chi_m^{(3)}$ also show that the interband may play an important role to determine the optical nonlinearities around the LSPR. As the nanoparticle size decreases, $\chi_m^{(3)}$ shows strong intensity increase and the local electric-field factor decreases. For applications of optical nonlinearities of Ag metamaterials to nanophotonics, novel structure designs may optimize the balance between the $\chi_m^{(3)}$ and local field factor.

Chapter 5

Power dependence of NLO properties of Ag nanoparticles

5.1 Introduction

Under Maxwell-Garnett EMA, the third-order susceptibility of metal particle composites is proportional to the intrinsic third-order susceptibility of the metal particle itself and forth power of the local electric field factor. In Chapter 4, I had discussed the size dependence of the intrinsic third-order susceptibility. Here, the enhancement of the effective optical nonlinearities of the metal nanoparticle through LSPR was investigated for Ag nanoparticles composites. Despite the great effort in the fabrication and characterization of metal nanoparticles and extraordinary interest in its nonlinear optical properties, modulation of the local electric field controlled by optical nonlinearity is poorly understood. By utilizing the optical nonlinearities of a metal nanoparticle via control of the local electric field, all-optical switches, routers and repeaters devices in nanophotonics may revolutionize various ultrafast optical applications [17].

Optical nonlinearities of metal nanoparticles have been often investigated at single photon energy by means of Z-scan, DFWM, and pump-and-probe methods. The evaluations in these papers were often performed for one wavelength only. This treatment restricts the understanding of the mechanisms underlying the nonlinear optical properties. The optical nonlinearities of Ag nanoparticles composite show strong photon energy dependence owing to plasmonics effects. Due to this strong photon energy dependence, conflicting previous investigations had attributed the optical nonlinearities to a variety of processes; including saturable absorption (SA), reverse SA (RSA), two-photon absorption (TPA), multi-photon absorption, excited state absorption and free-carrier absorption [68]. Furthermore, several previous investigations had shown mixed SA and RSA and evolution from RSA to SA as the excitation power is increased.

In this Chapter, I have systematically investigated the excitation power dependence in the nonlinear optical properties of Ag nanoparticles embedded in SiO_2. Samples description and linear optical properties were discussed in Chapter 2. Nonlinear optical properties were evaluated by using spectroscopic ellipsometry and pump-and-probe spectroscopy methods. The excitation power dependence in the transient transmission changes $\Delta T/T$ shows complex and non-monotonic changes. The experimental results of the local field factor reveal the possibility to modulate the optical resonance condition of an Ag nanoparticle by using its optical nonlinearity.

5.2 Power dependence of $\Delta T/T$

Optical nonlinearities were obtained by using a femtosecond pump-and-probe spectroscopy. The samples were exited at 0.5 kHz with pulse duration and

photon energy of 130 fs and 3.1 eV, respectively. Peak power density was controlled with a neutral density filter from 0.41 to 3.70 GW/cm^2. These values are under the optical damage threshold of the samples. $\Delta T/T$ of the Ag nanoparticles embedded in SiO_2 at various peak power densities are shown in Figure 5.1. $\Delta T/T$ shows a complex change as the excitation power is increased. One can observe that for all particles sizes, the maximum increases and redshifts with excitation power. The minimum also redshifts with excitation power, however, the shift is stronger. For a particle size of 13 nm, the shift with excitation intensity increase from 0.41 to 3.70 GW/cm^2 is of 0.03 and 0.07 eV in the maximum and minimum, respectively. The dispersion sign changeover redshifts with excitation power. This sign changeover is bigger for smaller Ag nanoparticles sizes.

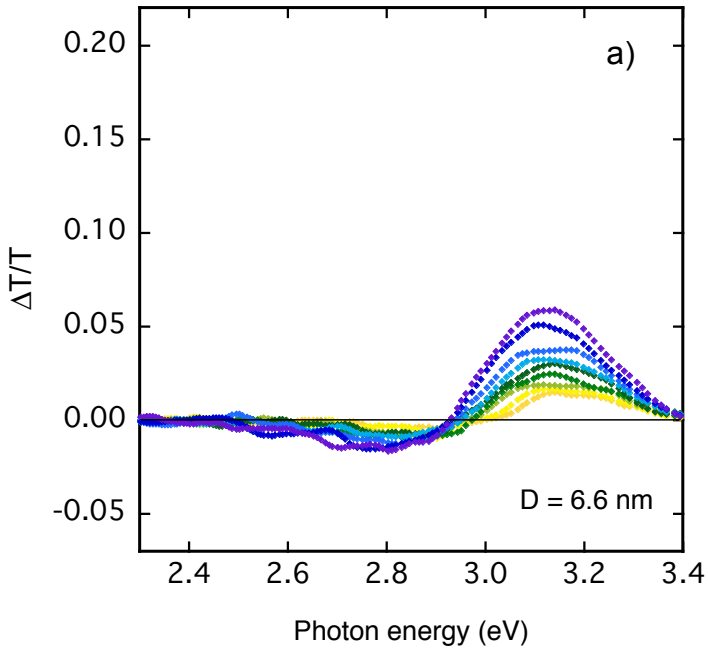
a)
0.20
0.15
0.10
0.05
0.00
-0.05
ΔT/T
D = 6.6 nm
2.4
2.6
2.8
3.0
3.2
3.4
Photon energy (eV)

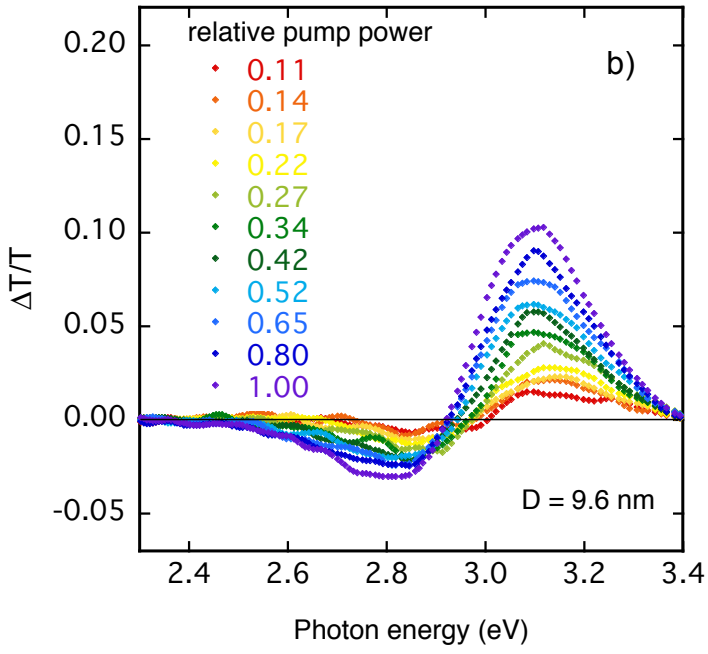
relative pump power
0.11
0.14
0.17
0.22
0.27
0.34
0.42
0.52
0.65
0.80
1.00
b)
0.20
0.15
0.10
0.05
0.00
-0.05
ΔT/T
D = 9.6 nm
2.4
2.6
2.8
3.0
3.2
3.4
Photon energy (eV)

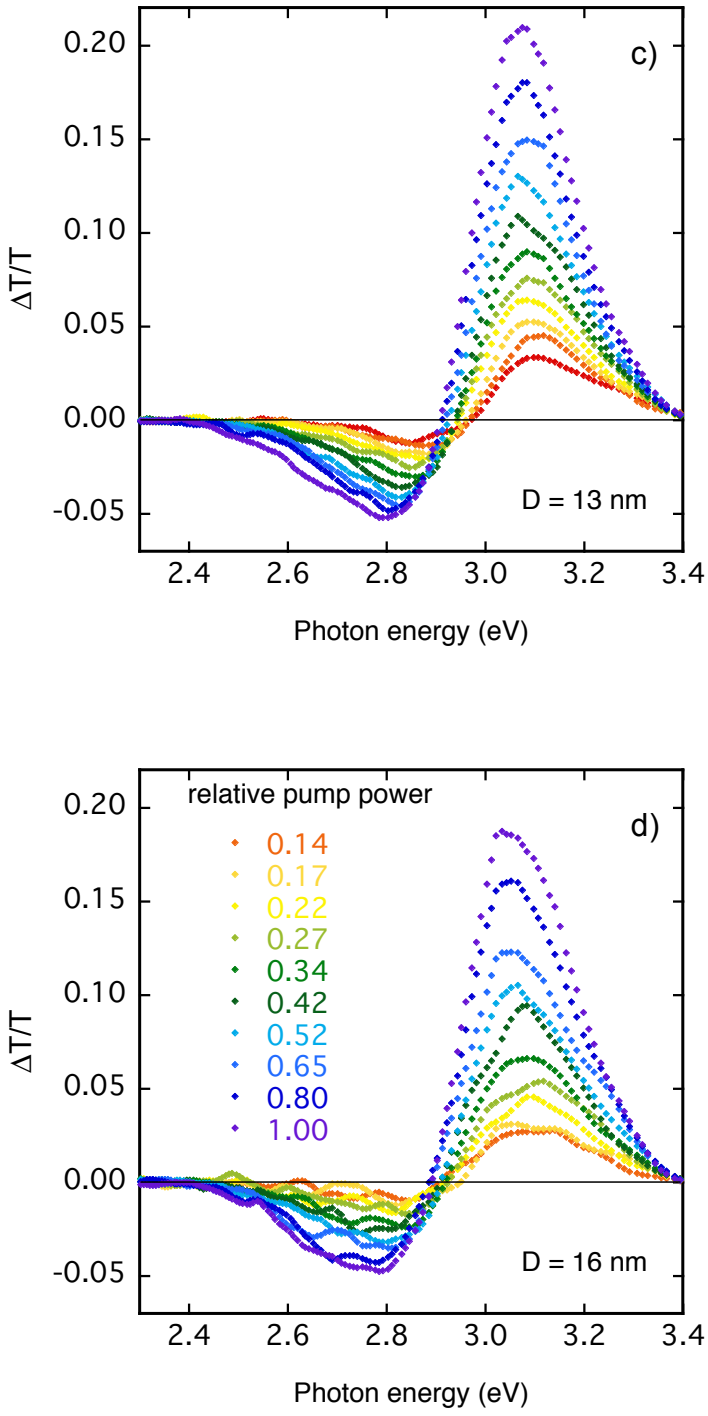

Figure 5.1: Dispersion of the transient transmission changes $\Delta T/T$ of Ag nanoparticles in SiO_2 with average particles sizes of a) 6.6, b) 9.6, c) 13 and d) 16 nm as labeled. Right after the excitation pulse at 3.1 eV.

By using the total differentiation, $\Delta T / T$ can be expressed as

$$\frac{\Delta T}{T} = \frac{1}{T}\frac{\partial T}{\partial n}\Delta n + \frac{1}{T}\frac{\partial T}{\partial k}\Delta k \,, \tag{5.1a}$$

$$\varepsilon_{eff} + \Delta\varepsilon_{eff} = \sqrt{\tilde{n} + \Delta\tilde{n}} \,, \tag{5.1b}$$

$$\Delta\varepsilon_{eff} = \tfrac{3}{4}\chi^{(3)}_{eff} I_0 \,, \tag{5.1c}$$

where $\tilde{n} = n + ik$ is the complex refractive index and I_0 is the peak power density. Under Maxwell-Garnett EMA, the third-order susceptibility $\chi^{(3)}_{eff}$ of metal particle composites is proportional to the intrinsic third-order susceptibility of the metal particle itself and forth power of the local electric field factor. In Chapter 3, I have showed that the dispersion of $\chi^{(3)}_{eff}$ of Ag nanoparticles mostly reflects the local field factor. Around the LSPR, the dispersion of $\Delta T / T$ also mostly reflects the local field factor due to the relation between $\Delta T / T$ and $\chi^{(3)}_{eff}$ (Equation 5.1). To understand the dispersion of $\Delta T / T$, the local field factor will be investigated.

5.3 Modulation of the local-electric field

5.3.1 Local field factor

The local field factor of metal nanoparticles for a low excitation was discussed in the Chapter 1. The local field factor was obtained for Ag particle sizes of 6.6, 9.6, 13 and 16 nm and shown in Figure 5.2. The dielectric functions of Ag nanoparticles and SiO_2 were obtained by spectroscopic ellipsometry. One can

observe that the local field enhancement increases with the increase of Ag nanoparticle size. Also, the resonance structure redshifts with the Ag nanoparticle size. This increase and redshift are due to the modification of the resonance condition at minimum intensity of $|\varepsilon_m + 2\varepsilon_d|$.

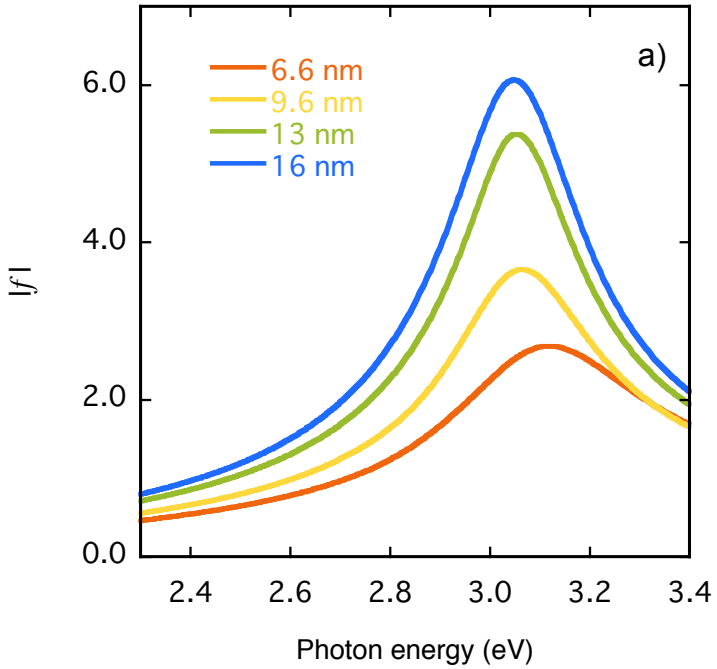

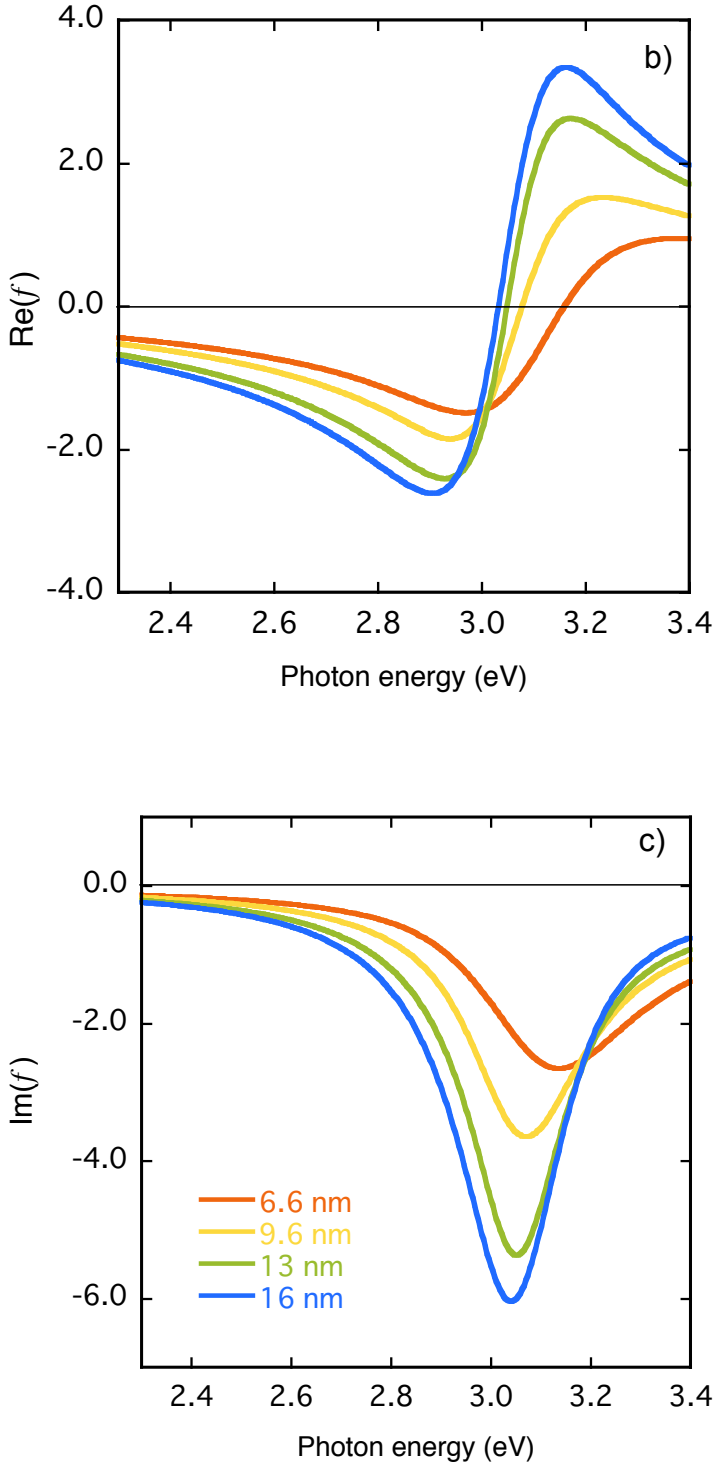

Figure 5.2: a) Absolute, b) real and c) imaginary components of the local field factor of Ag nanoparticles in SiO_2 with average particle sizes of 6.6, 9.6, 13 and 16 nm as labeled.

5.3.2 Evaluation of the modulation of the local field factor

By using the Maxwell-Garnett EMA, the local field factor was evaluated at various excitation intensities. Similarly to Chapter 4, $\chi_{eff}^{(3)}$ and $\chi_{m}^{(3)}$ were evaluated from $\Delta T/T$ by using spectroscopic ellipsometry and pump-and-probe spectroscopy [see Equations (4.1) and (4.2)]. $\chi_{eff}^{(3)}$ of Ag nanoparticles composites at various excitation intensities are shown in Figure 5.3.

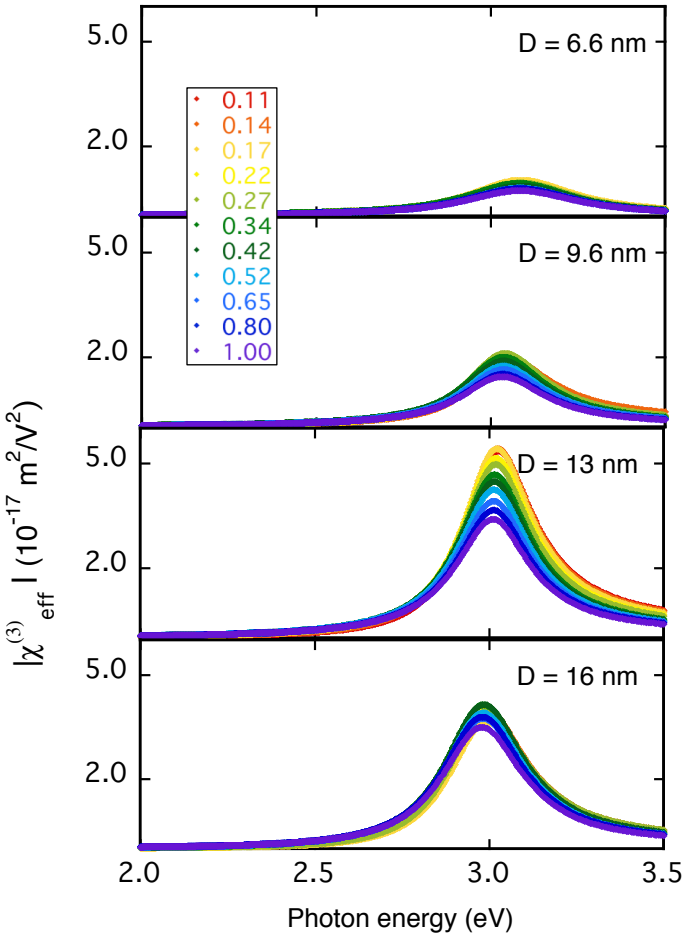

Figure 5.3: Absolute component of the third-order susceptibility of Ag nanoparticles in SiO_2 with average particle sizes of 6.6, 9.6, 13 and 16 nm as labeled.

5.3.3 Modulation of the local field

The local field factors of Ag nanoparticles composites at various excitation intensities are shown in Figure 5.4. For all particle sizes, the local field enhancement peak shows an intensity decrease and redshift as the excitation intensity increases. This decrease is stronger for higher excitation intensity; i.e. for particle size of 13 nm, relative excitation intensity from 0.11 to 0.42 and 0.11 to 1.00 shows a reduction in the local field enhancement peak of 2 % and 9 %, respectively. Furthermore, the local field factor values at lower photon energy increase with excitation intensity increase.

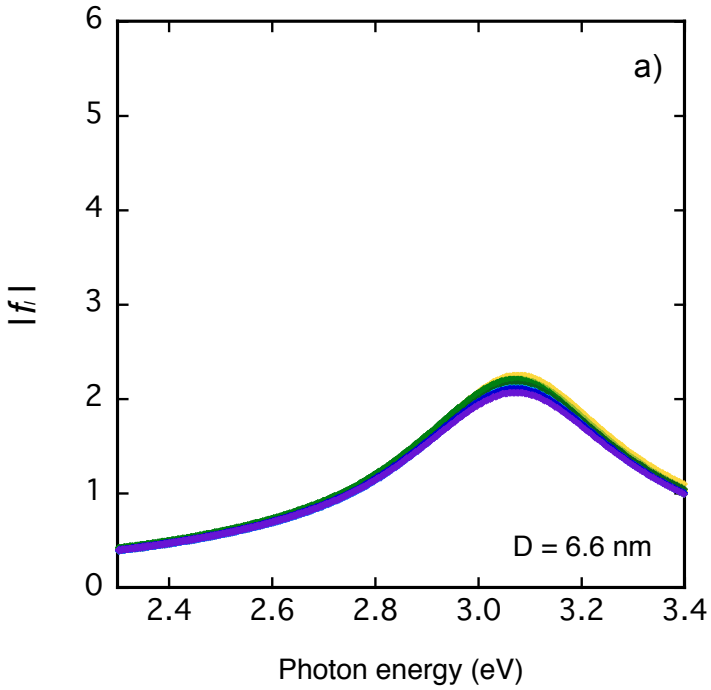
a)
D = 6.6 nm
|f|
Photon energy (eV)
0
1
2
3
4
5
6
2.4
2.6
2.8
3.0
3.2
3.4

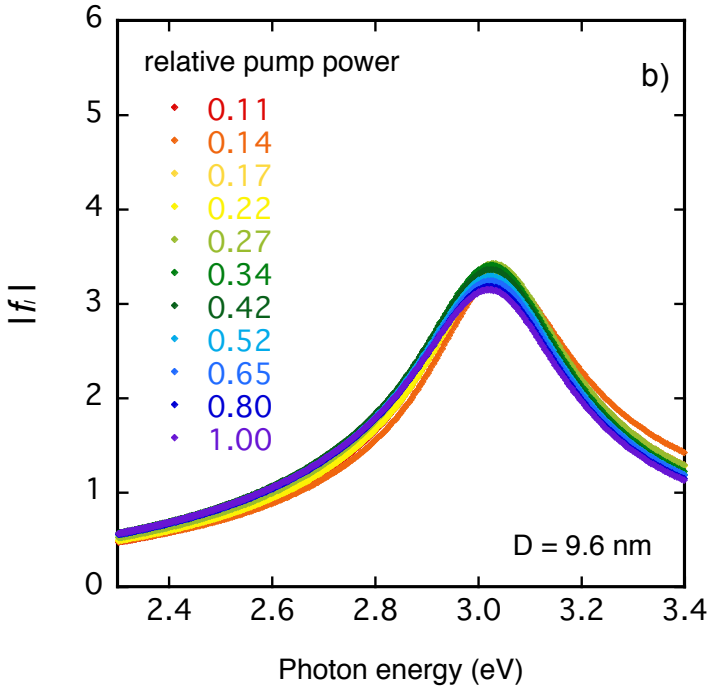
relative pump power
0.11
0.14
0.17
0.22
0.27
0.34
0.42
0.52
0.65
0.80
1.00
b)
D = 9.6 nm
|f|
Photon energy (eV)
0
1
2
3
4
5
6
2.4
2.6
2.8
3.0
3.2
3.4

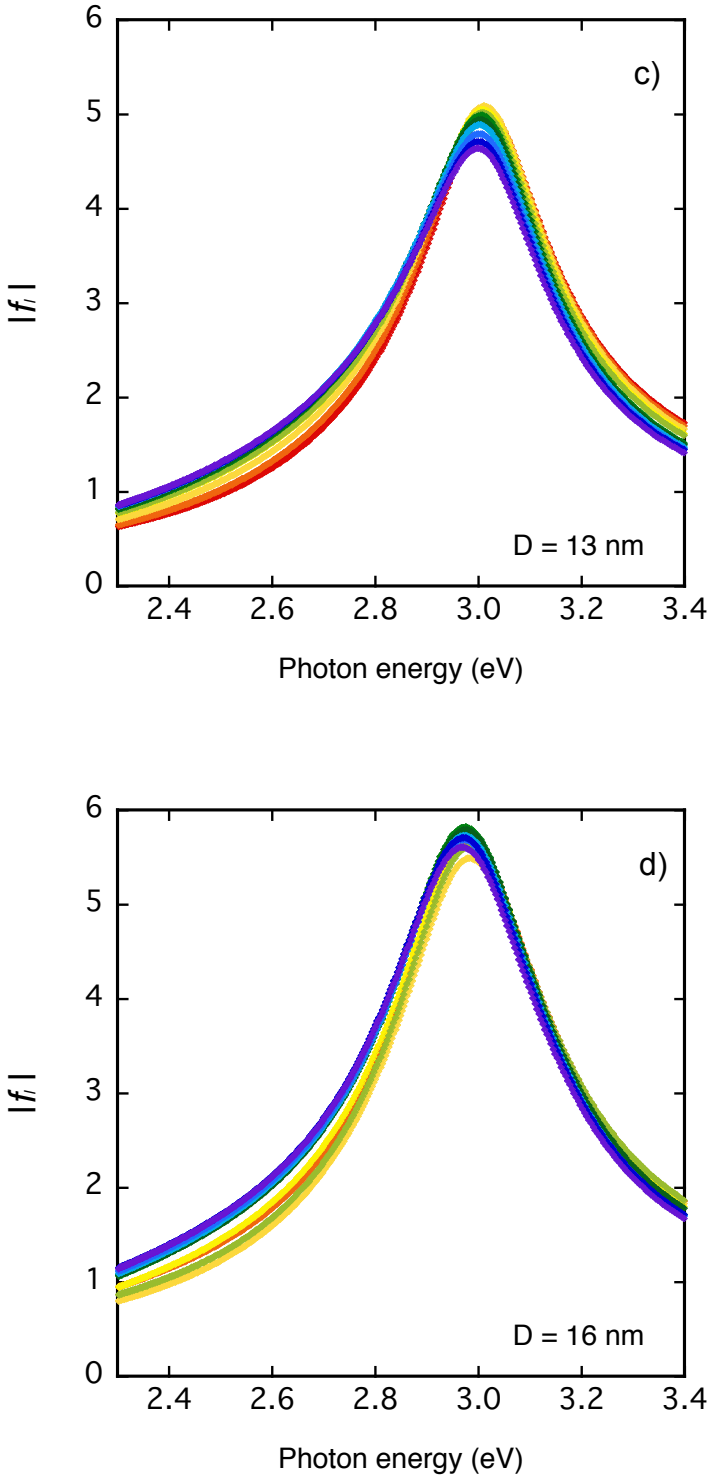

Figure 5.4: Absolute component of the local field factor of the Ag nanoparticle with particle sizes of a) 6.6, b) 9.6, c) 13 and d) 16 nm.

The local field factor depends on the excitation intensity and can be expressed as

$$f_l(\omega, I_0) = \frac{3\varepsilon_d(\omega)}{\varepsilon_m^{EXC}(\omega, I_0) + 2\varepsilon_d(\omega)}, \tag{5.2a}$$

$$\varepsilon_m^{EXC}(\omega, I_0) = 1 + \chi_m^{(1)}(\omega) + \chi_m^{(3)}(\omega)\left|f_l(\omega, I_0)\right|^2 I_0, \tag{5.2b}$$

ε_m^{EXC} is the dielectric function of an Ag particle at excitation-state. From Equation 5.2, one can observe the coupling between $\varepsilon_m^{EXC}(\omega, I_0)$ and $\left|f_l(\omega, I_0)\right|$, and $\left|f_l(\omega, I_0)\right|$ shows intensity dependence as the excitation intensity increases. However, the local field factor is generally thought to be constant [30,69]. Owing to this coupling, the Ag nanoparticle behaves as an internal feedback system that can alter its resonance condition by optical nonlinearity. Therefore, this internal feedback system leads to the peak position shift and spectral modulation of the local field factor that can be observed in Figure 5.4. For the smallest Ag particle size (6.6 nm), one can observe an overall dispersion decrease and shift smaller than 0.01 eV of the local field factor with excitation intensity. It demonstrates that the modulation of the local field factor by optical nonlinearity depends on the particle size. For a small particle, the local field enhancement might not be enough to modify its resonance condition. To understand these experimental results, a numerical calculation of the modulation of the local field by optical nonlinearities via $\chi_m^{(3)}$ will be discussed next. Drachev *et al.* [Drachev] have shown the local field factor of an Ag particle with various sizes and excitation intensities. The local field $\left|f_l(\omega, I_0)\right|$ can be solved numerically with [33]

$$A\left|f_l(\omega,I_0)\right|^6+B\left|f_l(\omega,I_0)\right|^4+C\left|f_l(\omega,I_0)\right|^2+D=0\,, \tag{5.3a}$$

and the coefficients as

$$A=c^2+d^2\,,\ B=2(ac+bd)\,,\ C=a^2+b^2\,,\ D=-\varepsilon_d^2\,, \tag{5.3b}$$

these parameters as

$$a=\mathrm{Re}(\varepsilon_m)+2\varepsilon_d\,,\ b=\mathrm{Im}(\varepsilon_m)\,,\ c=I_0\,\mathrm{Re}\left(\chi_m^{(3)}\right),\ d=I_0\,\mathrm{Im}\left(\chi_m^{(3)}\right), \tag{5.3c}$$

The numerically solved $\left|f_l(\omega,I_0)\right|$ at various excitation intensities is shown in Figure 5.5 [33]. For Ag nanoparticle size of 6 nm, the enhancement peak decreases with excitation intensity increase. For 22 nm, the enhancement peak decreases, and also redshifts and becomes distorted. From experimental results, these features were observed from particle size of 9.6 nm. The modulation of the local field factor by optical nonlinearities depends on the particle size. For smaller particles, the local field enhancement is not sufficient to modify its resonance condition via the third-order nonlinearity.

The modulation of the local field factor plays an important role to the nonlinear optical properties of Ag nanoparticles, including $\Delta T/T$. As the excitation intensity increases, $\Delta T/T$ changes non-monotonically (Figure 5.1). The resonant structure of $\Delta T/T$ redshifts, however the maximum and minimum shift differently; i.e. for a 13-nm-Ag-particle, the maximum and minimum of $\Delta T/T$ shift 0.04 and 0.07 eV, respectively. The sign changeover of the resonant structure also redshifts with the excitation intensity increase and the shift is stronger for smaller particles. To better observe the non-monotonically changes with power and size dependence, $\Delta T/T$ at selected

photon energies with respect to the excitation intensity is plotted in Figure 5.6. From 0.41 to 1.55 GW/cm^2, relative excitation intensity from 0.11 to 0.42, $\Delta T/T$ can be considered linearly proportional to the excitation intensity [19]. In this range, the linear fit of $\Delta T/T$ is shown as dashed lines. As the excitation intensity exceeds 1.55 GW/cm^2, $\Delta T/T$ shows a complex behavior. At 2.80 and 3.10 eV, $\Delta T/T$ intensity decreases with respect to the nonlinear response at lower excitation intensity. Conversely, the intensity increases for 3.00 eV. Furthermore, around 2.93 eV, for all particle sizes, $\Delta T/T$ changes sign from negative to positive as the excitation intensity increases.

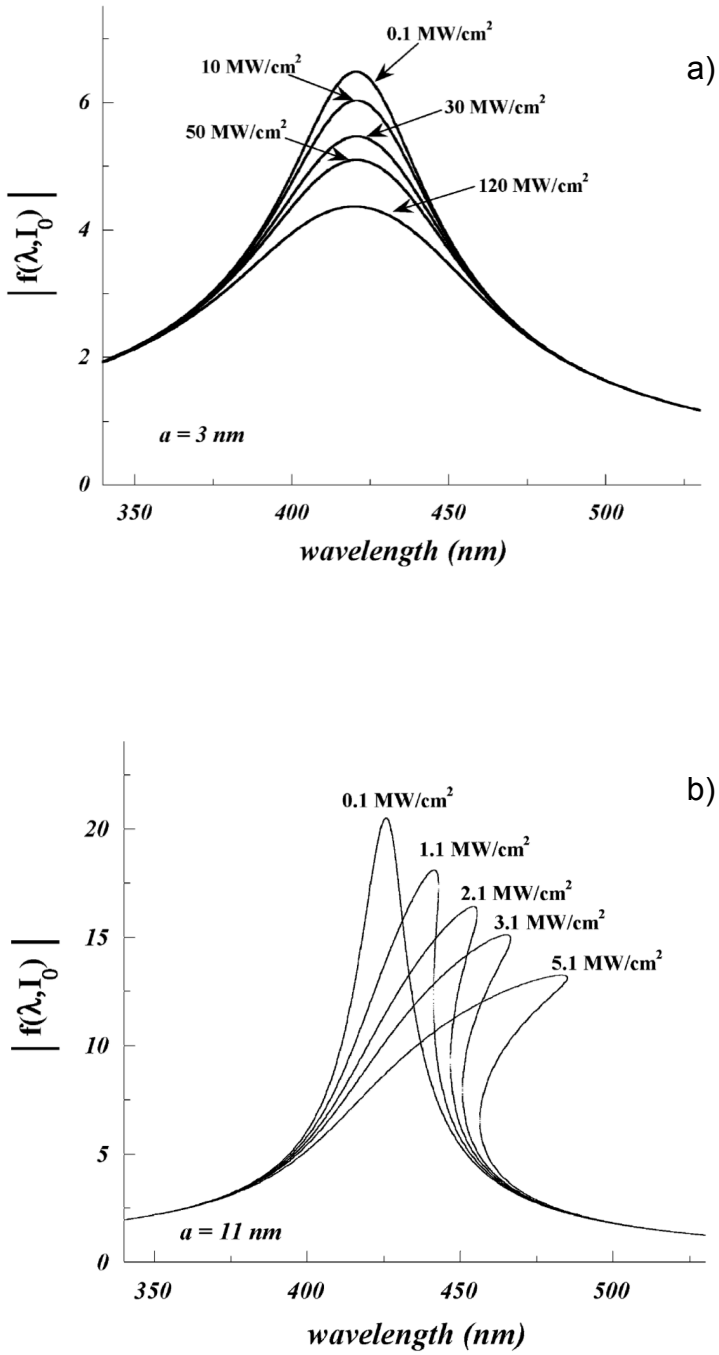

Figure 5.5: Absolute component of the local field factor of an Ag nanoparticle with particle diameters of a) 6 and d) 22 nm [33].

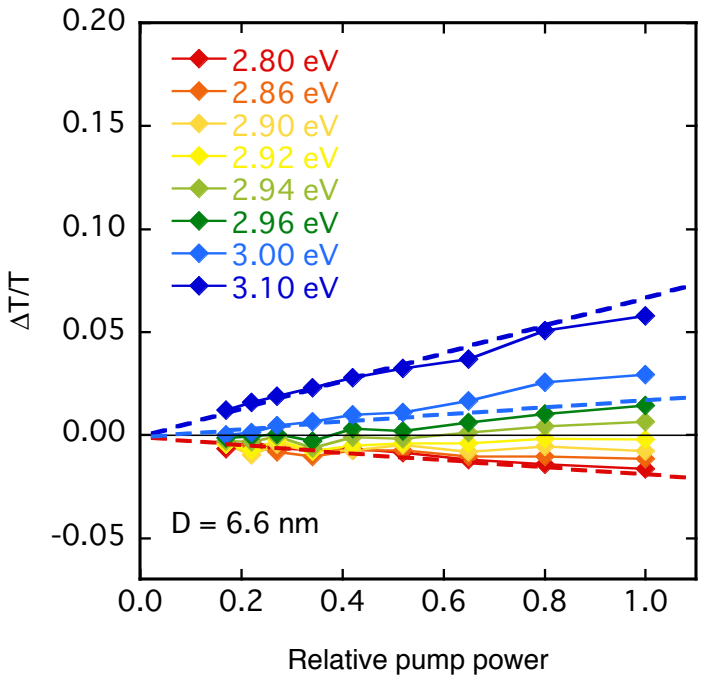
0.20
0.15
0.10
0.05
0.00
-0.05
ΔT/T
2.80 eV
2.86 eV
2.90 eV
2.92 eV
2.94 eV
2.96 eV
3.00 eV
3.10 eV
D = 6.6 nm
0.0
0.2
0.4
0.6
0.8
1.0
Relative pump power

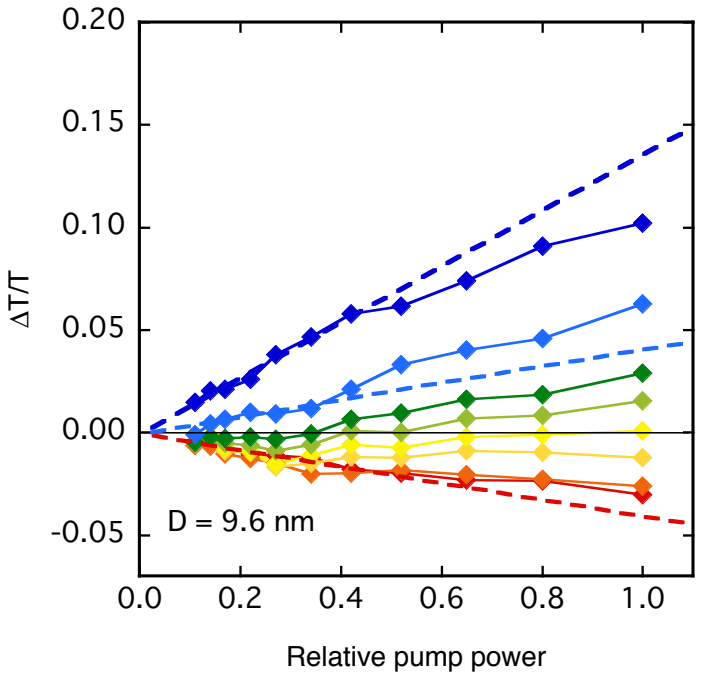
0.20
0.15
0.10
0.05
0.00
-0.05
ΔT/T
D = 9.6 nm
0.0
0.2
0.4
0.6
0.8
1.0
Relative pump power

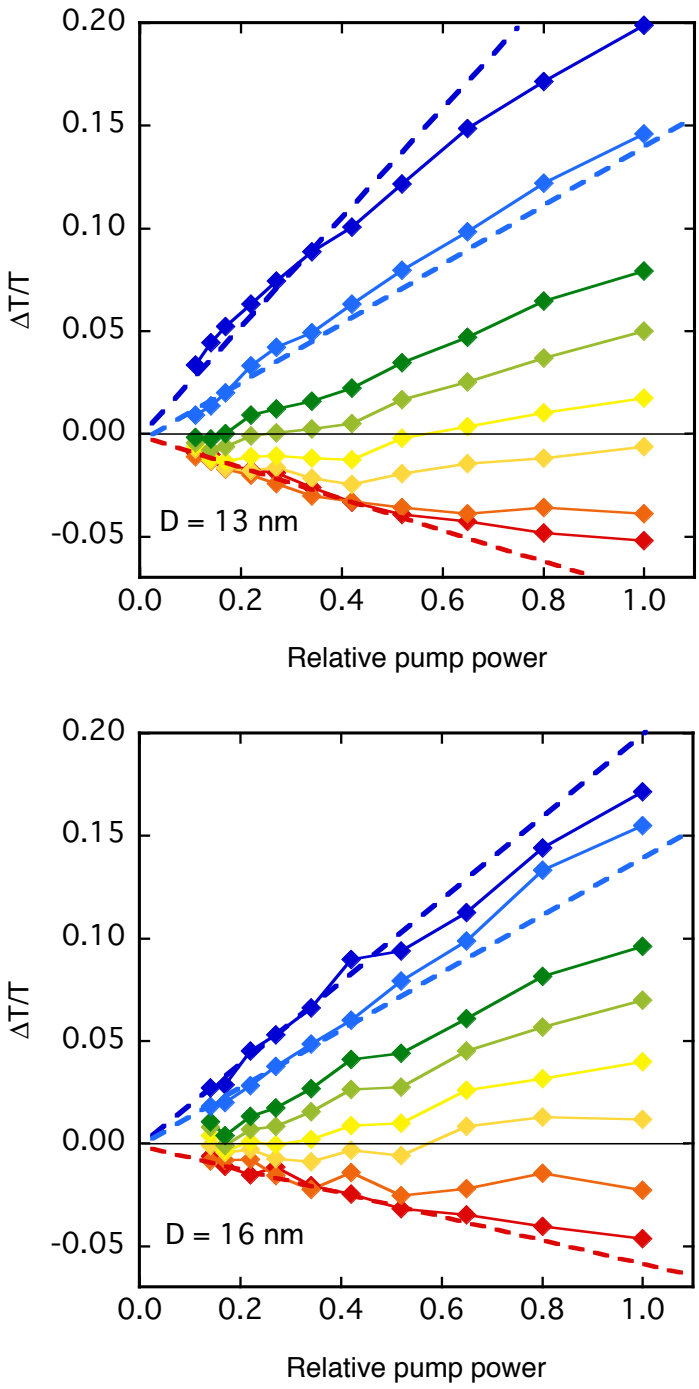

Figure 5.6: Transient transmission changes $\Delta T / T$ of Ag nanoparticles embedded in SiO_2 with particle sizes of a) 6.6, b) 9.6, c) 13 and d) 16 nm. Values relative to a maximum pump intensity of 3.70 GW/cm^2. Solid lines are guides to the eyes. Dashed lines represent the linear fit of ΔT / T of 2.80, 3.00, and 3.10 eV up to a relative excitation intensity of 0.42.

From Figure 5.6, one can observe the strong sensitivity of the $\Delta T/T$ of Ag nanoparticles composite to the particle size, photon energy and excitation intensity. By measuring at single or a few photon energies around the LSPR, these dependencies can potentially result in misleading conclusions by attributing SA and/or RSA to a specific metal nanoparticles. Phenomenological SA and RSA correspond to positive and negative $\Delta T/T$, respectively. By using an open aperture Z-scan, Boni et al. [70] have measured the optical nonlinearities of Ag nanoparticles, with an average particles size of 5.4 nm, in a lead-germanium oxide glass (Figure 5.7). Pulse width and repetition rate of 120 fs and 1 kHz, respectively. From Z-scan results, they attributed RSA between 2.25 (550 nm) and 2.58 ev (480 nm) owing to a two-photon absorption process of the substrate enhanced by the Ag particles. Ganeev et al. [71] have measured Ag nanoparticles, with 5-10 nm sizes, in water (Figure 5.8). Pulse width and repetition rate of 1.2 ps and 10 Hz, respectively. At 3.12 eV (397 nm), they concluded SA owing to a nonlinear refractive process. In contrast to these conclusions, the dispersion of $\Delta T/T$ (RSA and SA) in the vicinity of the LSPR observed here, are attributed mainly to the dispersion of the local field factor (plasmonics effects) via $\chi_m^{(3)}$ (see Figure 5.1 and Equations 5.1).

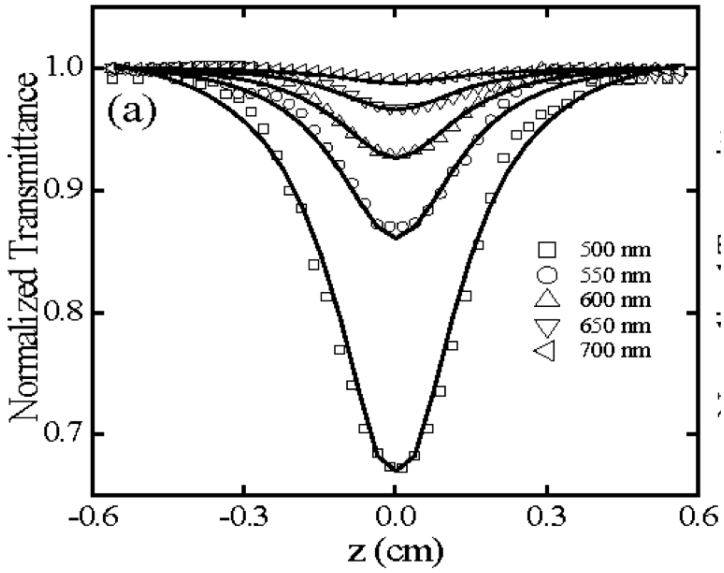

Figure 5.7: Open aperture Z-scan at several wavelengths in Ag particles in lead-germanium oxide glass with average particle size of 5.4 nm [70].

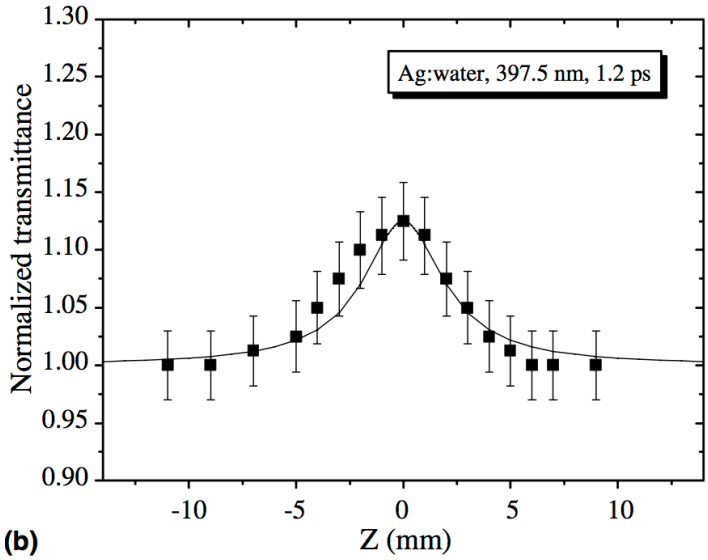

Figure 5.8: Open aperture Z-scan at 3.12 eV (397 nm) in Ag particles in water with particle size of 5-10 nm [71].

By using an open aperture Z-scan, Karthikeyan *et al.* [72] systematically measured the $\Delta T/T$ of Ag nanoparticles embedded in soda lime glass with four particle sizes between 2.6 to 6.3 nm (Figure 5.9). Pulse width and repetition rate of 100 fs and 1 Hz, respectively. At 3.07 eV, they attributed RSA for small Ag particles owing to the interband transitions by two-photon absorption process. In contrast to these conclusions, here I showed that all particle sizes present negative and positive $\Delta T/T$ at lower and higher photon energy (Figure 5.1) owing to plasmonics effects. In Karthikeyan *et al.* investigation, the size dependence of the normalized transmission is due to the LSPR shift with Ag particle size.

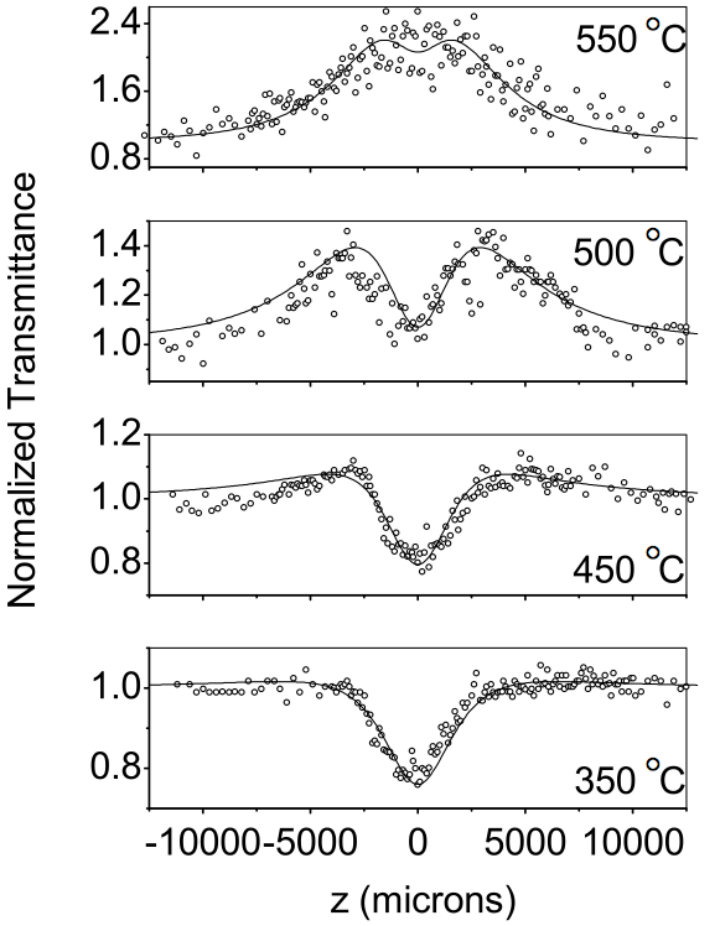

Figure 5.9: Open aperture Z-scan at 3.07 eV (404 nm) in Ag particles in soda lime glass with estimated particle size of 6.35 (550 °C), 4.62 (500 °C), 3.63 (450 °C), 2.58 nm (350 °C) [72].

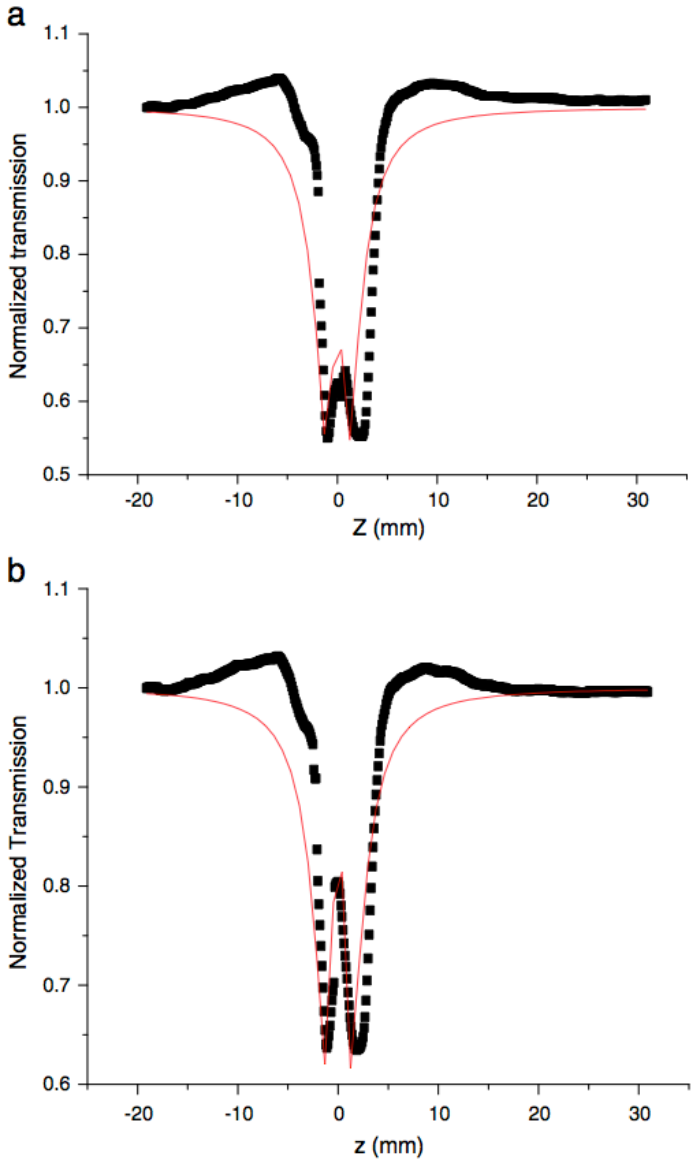

Figure 5.10: Open aperture Z-scan at 3.07 eV (404 nm) in Ag particles in soda lime glass with estimated particle size of 6.35 (550 °C), 4.62 (500 °C), 3.63 (450 °C), 2.58 nm (350 °C) [32].

By measuring at single photon energy around the LSPR, excitation dependency can also potentially result in misleading conclusions by attributing changeover from RSA to SA to a specific metal nanoparticles [73-80]. By using an open aperture Z-scan, Henari *et al.* [32] measured the $\Delta T/T$ of Ag nanoparticles embedded in europium oxide glass with excitation intensities of 1.1 x 10^7 and 3.2 x 10^7 W/m^2 (Figure 5.10). Experiment was performed with a continuous wave at photon energy of 2.60 eV (476 nm). They attributed RSA to the interband transitions by two-photon absorption process and SA to the surface plasmon resonance band bleach. Here, I showed that the sign changeover from negative to positive values of $\Delta T/T$ with respect to excitation intensity appears near the LSPR owing to nonlinear modulation of the local field via $\chi_m^{(3)}$.

5.4 Chapter summary

In this Chapter, the characterization of the optical nonlinearities of Ag nanoparticles on excitation intensity, particle size and photon energy explored the fundamental nonlinear optical properties of metal nanoparticles. The present results clarified the apparently conflicting previous findings based on Z-scan measurements. In contrast to conclusions based on single photon energy results, I have shown that the dispersion of the transient transmission changes reflects mainly the local field enhancement and its nonlinear modulation. For all Ag particle sizes, the transient transmission changes show negative and positive values at lower and higher photon energy in the vicinity of the localized surface plasmon resonance. For particle sizes larger than 9.6 nm, the transient transmission changes peak position and change of sign redshift with excitation intensity increase. This demonstrates the modulation

of the resonance condition by optical nonlinearities. The modulation control of the local electric field of a metal nanoparticle via third-order nonlinearities has several applications in nanophotonics. Intrinsic nonlinear modulation without an external feedback system shows ultrafast response, energy efficiency and nanoscale device size [17,81-84]. These results may provide new insights to optimization of metal nanoparticles and metalmaterials.

Chapter 6

Conclusion

In this Thesis, I fabricated Ag nanoparticles embedded in silica glass and evaluated its optical nonlinearities. From these results, fundamental nonlinear optical properties were investigated. The main achievements of this study are:

- I successfully analyzed the dispersion of the effective $\chi_{eff}^{(3)}$ and intrinsic $\chi_{m}^{(3)}$ in a wide photon energy range (2.0 – 3.5 eV) with particle sizes in the quantum regime.

- I demonstrated the effects of size quantization in the nonlinear optical properties of Ag nanoparticle ranging from 3.0 to 16 nm. $\left|\chi_{m}^{(3)}\right|$ strongly increases for smaller particles. In addition, I showed the critical particle size at 15 nm. This critical size is due to the contribution of quantum and plasmonic effects at smaller and bigger particle sizes, respectively.

- I demonstrated the nonlinear modulation of the local field factor via $\chi_{m}^{(3)}$ without an external feedback system. This modulation shows size dependence. For D ≤ 6.6 nm, overall decrease of the local field factor

was observed with excitation intensity increase. For D > 6.6 nm, I showed the modulation of the local field factor.

- I showed that $\Delta T/T$ has a non-monotonically change with excitation intensity around the LSPR. Negative to positive $\Delta T/T$ with excitation intensity was observed.

- From the experimental results of size and power dependence of the optical nonlinearities, I clarified the conflicting single photon energy experimental results.

6.1 Future work

In this Thesis, I have measured and analyzed the $\chi_m^{(3)}$ of Ag nanoparticles up to particle size of 16 nm. This was a limitation of the ion-implantation technique. Theoretical approaches predict an increase of $\chi_m^{(3)}$ with r^2 dependence. However, this theoretical result is unphysical and $\chi_m^{(3)}$ is expected to converge to the bulk value for larger particles. Therefore, experimental measurements of particle sizes larger than 16 nm are needed.

Influence of interband transition and "hot electron" to the size dependence of $\chi_m^{(3)}$ can be investigated by measuring Au and Cu nanoparticles. These metal have overlapped LSPR and interband transitions.

I have shown the nonlinear modulation of the local field factor via $\chi_m^{(3)}$ without an external feedback system. By controlling the nonlinear modulation control of the local field factor, bistable regime of the nonlinear optical properties may be observed at specific conditions. This bistable regime plays an important role to advance several nanophotonics technologies, such as ultrafast all-optical switches, routers, repeaters and single-photon generation. In most configurations, optical bistability is achieved by a nonlinear material and an external resonator. However, the use of an external feedback system slows down the temporal response and requires special alignment. Intrinsic optical bistability of pure metallic particles has been predicted numerically but never experimentally realized yet.

International peer-reviewed journals

R. Sato, H. Momida, M. Ohnuma, M. Sasase, T. Ohno, N. Kishimoto, and Y. Takeda, "Experimental dispersion of the third order optical susceptibility of Ag nanoparticles," *JOSA B* **29**, 2410-2413 (2012).

R. Sato, M. Ohnuma, K. Oyoshi, and Y. Takeda, "Experimental investigation of nonlinear optical properties of Ag nanoparticles: Effects of size quantization," *Phys. Rev. B* **90**, 125417 (2014).

R. Sato, M. Ohnuma, K. Oyoshi, and Y. Takeda, "Spectral investigation of nonlinear local field effects in Ag nanoparticles," *submitted to J. Appl. Phys.*

References

[1] I. Angelini, G. Artioli, P. Bellintani, V. Diella, M. Gemmi, A. Polla, and A. Rossi, "Chemical analyses of bronze age glasses from Frattesina di Rovigo, northern Italy," Journal of Archeological Science 31, 1175-1184 (2004).

[2] O. Bobin, M. Schvoerer, J. L. Miane, and J. F. Fabre, "Coloured metallic shine associated to luster decoration of glaze ceramics: a theoretical analysis of the optical properties," Journal of Non-Crystalline Solids 332, 28-34 (2003).

[3] P. Sciau, Nanoparticles in Ancient Materials: The Metallic Lustre Decorations of Medieval Ceramics, The Delivery of Nanoparticles (InTech Europe Ed., Rijeka, Croatia, 2012)

[4] M. Faraday, "The Bakerian lecture: experimental relations of gold (and other metals) to light," Philosophical Transactions of the Royal Society of London 147, 145-181 (1847).

[5] J. A. A. J. Perenboom, P. Wyder, and F. Meier, "Electronic properties of small metallic particles," *PHYSICS REPORTS (Review Section of Physics Letters)* **78**, 173-292 (1981).

[6] K. L. Kelly, E. Coronado, L. L. Zhao, and G. C. Schatz, "The optical properties of metal nanoparticles: The influence of size, shape, and dielectric environment," *Journal of Physical Chemistry B* **107**, 668-677 (2003).

[7] M. A. Garcia, "Surface plasmons in metallic nanoparticles: fundamentals and applications," *Journal of Physics D: Applied Physics* **44**, 283001 (2011).

[8] Y. He, and T. Zeng, "First-principles study and model of dielectric functions of silver nanoparticles," *Journal of Physical Chemistry* **114**, 18023-18030 (2010).

[9] J. Ando, K. Fujita, N. I. Smith, and S. Kawata, "Dynamic SERS imaging of cellular transport pathways with endocytosed gold nanoparticles," *Nano Letters* **11**, 5344-5348 (2011).

[10] Z. Fan, M. Shelton, A. K. Singh, D. Senapati, S. A. Khan, and P. C. Ray, "Multifunctional plasmonic shell-magnetic core nanoparticles for targeted diagnostics, isolation, and photothermal destruction of tumor cells," *ACS Nano* **6**, 1065-1073 (2012).

[11] D. K. Gramotnev, and S. I. Bozhevolnyi, "Plasmonics beyond the diffraction limit," *Nature Photonics* **4**, 83-91 (2010).

[12] K. F. MacDonald, Z. L. Samson, M. I. Stockman, and N. I. Zheludev, "Ultrafast active plasmonics," *Nature Photonics* **3**, 55-58 (2009).

[13] P. N. Butcher and D. Cotter, *The Elements of Nonlinear Optics* (Cambridge University Press, Cambridge, United Kingdom, 1990).

[14] F. Hache, D. Richard, and C. Flytzanis, "Optical nonlinearities of small metal particles: surface-mediated resonance and quantum size effects," *Journal of the Optical Society of America B* **3**, 1647-1655 (1986).

[15] N. del Fatti, and F. Vallee, "Ultrafast optical nonlinear properties of metal nanoparticles," *Applied Physics B* **73**, 383-390 (2001).

[16] T. Hanke, J. Cesar, V. Knittel, A. Trugler, U. Hohenester, A. Leitenstorfer, and R. Bratschitsch, "Tailoring spatiotemporal light confinement in single plasmonic nanoantennas," *Nano Letters* **12**, 992-996 (2012).

[17] M. Kauranen, and A. V. Zayats, "Nonlinear plasmonics," *Nature Photonics* **6**, 737-748 (2012).

[18] Y.-K. Yoon, R. S. Bennink, R. W. Boyd, and J. E. Sipe, "Intrinsic optical bistability in a thin layer of nonlinear optical material by means of local field effects," *Optics Communications* **179**, 577-580 (2000).

[19] R. W. Boyd, *Nonlinear Optics* (Academic Press, San Diego, Calif, USA, 2008).

[20] M. S. Bahae, A. A. Said, T.-H. Wei, D. J. Hagan, and E. W. van Stryland, "Sensitive measurement of optical nonlinearities using a single beam," *IEEE Journal of Quantum electronics* **26**, 760-769 (1990).

[21] Y. Hamanaka, A. Nakamura, N. Hayashi, and S. Omi, "Dispersion curves of complex third-order optical susceptibilities around the surface plasmon resonance in Ag nanocrystal-glass composites," *Journal of the Optical Society of America B* **20**, 1227-1232 (2003).

[22] Y. Hamanaka, A. Nakamura, S. Omi, N. del Fatti, F. Vallee, and C. Flytzanis, "Ultrafast response of nonlinear refractive index of silver nanocrystals embedded in glass," *Applied Physics Letters* **75**, 1712-1714 (1999).

[23] C. Voisin, N. del Fatti, D. Christofilos, and F. Vallee, "Ultrafast electron dynamics and optical nonlinearities in metal nanoparticles," *Journal of Physical Chemistry B* **105**, 2264-2280 (2001).

[24] M. Quinten, *Optical Properties of Nanoparticle Systems* (Wiley-Vch, Weinheim, Germany, 2011).

[25] A. L. Stepanov, "Nonlinear optical properties of implanted metal nanoparticles in various transparent matrixes: A Review," *Reviews on Advanced Materials Science* **27**, 115-145 (2011).

[26] J. A. Scholl, A. L. Koh, and J. A. Dionne, "Quantum plasmon resonances of individual metallic nanoparticles," *Nature* **483**, 421-428 (2012).

[27] K. Uchida, S. Kaneko, S. Omi, H. Tanji, Y. Asahara, and A. J. Ikushima, "Optical nonlinearities of a high concentration of small metal particles dispersed in glass: copper ad silver nanoparticles," *Journal of the Optical Society of America B* **11**, 1236-1243 (1994).

[28] L. Yang, K. Becker, F. M. Smith, R. H. Magruder III, R. F. Haglund Jr., L. Yang, R. Dorsinville, and R. R. Alfano, "Size dependence of the third-order susceptibility of copper nanoclusters investigated by four-wave mixing," *Journal of the Optical Society of America B* **11**, 457-461 (1994).

[29] A. A. Govyadinov, G. Y. Panasyuk, J. C. Schotland, and V. A. Markel, "Theoretical and numerical investigation of the size-dependent optical effects in metal nanoparticles," *Physical Review B* **84**, 155461 (2011).

[30] U. Gurudas, E. Brooks, D. M. Bubb, S. Heiroth, T. Lippert, and A. Wokaun, "Saturable and reverse saturable absorption in silver nanodots using picosecond laser pulses," *Journal of Applied Physics* **104**, 073107 (2008).

[31] C. Zheng, W. Li, W. Chen, and X. Ye, "Nonlinear optical behavior of silver nanopentagons," *Materials Letters* **116**, 1-4 (2014).

[32] F. Z. Henari, and A. A. Dakhel, "Observation of simultaneous reverse saturation absorption and saturation absorption in silver nanoparticles incorporated into europium oxide thin film," *Optics Communications* **284**, 651-655 (2011).

[33] V. P. Drachev, A. K. Buin, H. Nakotte, and V. M. Shalaev, "Size dependent $\chi^{(3)}$ for conduction electrons in Ag nanoparticles," *Nano Letters* **4**, 1535-1539 (2004).

[34] M. Fox, *Optical Properties of Solids* (Oxford University Press, New York, USA, 2010).

[35] D. E. Chang, V. Vuletic, and M. D. Lukin, "Quantum nonlinear optics – photon by photon," *Nature Photonics* **8**, 685-694 (2014).

[36] D. E. Chang, A. S. Sorensen, P. R. Hemmer, and M. D. Lukin, "Quantum optics with surface plasmon," *Physical Review Letters* **97**, 053002 (2006).

[37] H. Hovel, S. Fritz, A. Hilger, and U. Kreibig, "Width of cluster plasmon resonances: Bulk dielectric functions and chemical interface damping," *Physical Review B* **48**, 178-188 (1993).

[38] S. Thomas, S. K. Nair, E. M. A. Jamal, S. H. Al-Harthi, M. R. Varma, and M. R. Anantharaman, "Size-dependent surface plasmon resonance in silver silica nanocomposites," *Nanotechnology* **19**, 1-7 (2008).

[39] D. D. Evanoff Jr., and G. Chumanov, "Synthesis and optical properties of silver nanoparticles and arrays," *ChemPhysChem* **6**, 1221-1231 (2005).

[40] M. Schnippering, M. Carrara, A. Foelske, R. Kotz, and D. J. Fermin, "Electronic properties of Ag nanoparticle arrays. A Kelvin probe and high resolution XPS study," *Physical Chemistry Chemical Physics* **9**, 725-730 (2007).

[41] R. L. Zimmerman, D. Ila, C. Muntele, and I. Muntele, "Ion beam assisted formation of nanolayers," *Nuclear Instruments and Methods in Physics Research B* **241**, 506-510 (2005).

[42] D. Ila, E. K. Williams, S. Sarkisov, C. C. Smith, D. B. Poker, and D. K. Hensley, "Formation of metallic nanoclusters in silica by ion implantation," *Nuclear Instruments and Methods in Physics Research B* **141**, 289-293 (1998).

[43] U. Kreibig, M. Vollmer, *Optical Properties of Metal Clusters* (Springer, Berlin, Germany, 1995).

[44] N. Kishimoto, Y. Takeda, C. G. Lee, N. Umeda, N. Okubo, and E. Iwamoto, "High-current heavy-ion accelerator system and its application to material modification," *Japanese Journal of Applied Physics* **40**, 1087-1090 (2001).

[45] J. F. Ziegler, J. P. Biersack, and U. Littmark, *The Stopping and Range of Ions in Solids* (Pergamon Press, New York, USA, 1985).

[46] G. Cocco, L. Schiffini, G. Strukul and G. Caturan, "Bimodal metal particle size distributions of Pd and Pt on vitreous supports from SAXS data," *Journal of Catalysis* **65**, 348-358 (1980).

[47] H. Fujiwara, *Spectroscopic Ellipsometry* (Willey Press, West Sussex, England, 2007).

[48] P. B. Johnson, and R. W. Christy, "Optical constants of the noble metals," *Physical Review B* **6**, 4370 (1972).

[49] F. J. G. de Abajo, "Microscopy: Plasmon go quantum," *Nature* **483**, 417-418 (2012).

[50] M. G. Papadopoulos, A. J. Sadlej, and J. Leszczynski, *Nonlinear Optical Properties of Matter* (Springer, Dordrecht, The Netherlands, 2006).

[51] M. Sheik-Bahae, A. A. Said, T.-H. Wei, D. J. Hagan, and E. W. van Stryland, "Sensitive measurement of optical nonlinearities using a single beam," *IEEE Journal of Quantum Electronics* **26**, 760-769 (1990).

[52] J. Wang, B. Gu, H.-T. Wang, and X.-W. Ni, "Z-scan analytical theory for material with saturble absorption and two-photon absorption," *Optics Communications* **283**, 3525-3528 (2010).

[53] C. Rulliere, *Femtosecond Laser Pulses* (Springer, The Netherlands, 2005).

[54] C. Nagura, A. Suda, H. Kawano, M. Obara, and K. Midorikawa, "Generation and characterization of ultrafast white-light continuum in condensed media," *Applied Optics* **41**, 3735-3742 (2002).

[55] T. Stoll, P. Maioli, A. Crut, N. del Fatti, and F. Vallee, "Advances in femto-nano-optics: ultrafast nonlinearity of metal nanoparticles," *The European Physical Journal B* **87**, 260 (2014).

[56] Y. Takeda, O. A. Plaksin, and N. Kishimoto, "Dispersion of nonlinear dielectric function of Au nanoparticles in silica glass," *Optics Express* **15**, 6010-6018 (2007).

[57] J.-Y. Bigot, V. Halte, J.-C. Merle, and A. Draunois, "Electron dynamics in metallic nanoparticles," *Chemical Physics* **251**, 181-203 (2000).

[58] W. Zhang, M. Saliba, S. D. Stranks, Y. Sun, X. Shi, U. Wiesner, and H. J. Snaith, "Enhancement of perovskite-based solar cells employing core-shell metal nanoparticles," *Nano Letters* **13**, 4505-4510 (2013).

[59] K. C. Bantz, A. F. Meyer, N. J. Wittenberg, H. Im, O. Kurtulus, S. H. Lee, N. C. Lindquist, S.-H. Oh, and C. L. Haynes, "Recent progress in SERS biosensing," *Physical Chemistry Chemical Physics* **13**, 11551-11567 (2011).

[60] J. N. Anker, W. P. Hall, O. Lyandres, N. C. Shah, J. Zhao, and R. P. van Duyne, "Biosensing with plasmonic nanosensors," *Nature Materials* **7**, 442-453 (2008).

[61] G. A. Wurtz, R. Pollard, W. Hendren, G. P. Wiederrecht, D. J. Gosztola, V. A. Podolskiy, and A. V. Zayats, "Designed ultrafast optical nonlinearity plasmonic nanorod metamaterial enhanced by nonlocality," *Nature Nanotechnology* **6**, 107-111 (2011).

[62] C. Argyropoulos, C. Ciraci, and D. R. Smith, "Optical bistability with film-coupled plasmonic nanocubes," *Applied Physics Letters* **104**, 063108 (2014).

[63] H. Husu, R. Siikanen, J. Makitalo, J. Lehtolahti, J. Laukkanen, M. Kuittinen, and M. Kauranen, "Metamaterials with tailored nonlinear optical response," *Nano Letters* **12**, 673-677 (2012).

[64] M. Abb, P. Albella, J. Aizpurua, and O. L. Muskens, "All-optical control of a single plasmonic nanoantenna-ITO hybrid," *Nano Letters* **11**, 2457-2463 (2011).

[65] R. E. Noskov, A. E. Krasnok, and Y. S. Kivshar, "Nonlinear metal-dielectric nanoantennas for light switching and routing," *New Journal of Physics* **14**, 093005 (2012).

[66] N. Meinzer, W. L. Barnes, and I. R. Hooper, "Plasmonic meta-atoms and metasurfaces," *Nature Photonics* **8**, 889-898 (2014).

[67] S. G. Rautian, "Nonlinear saturation spectroscopy of the degenerate electron gas in spherical metallic particles," *JETP* **85**, 451-461 (1997).

[68] M. Hari, S. Mathew, B. Nithyaja, S. A. Joseph, V. P. N. Nampoori, and P. Radhakrishnan, "Saturable and reverse saturable absorption in aqueous silver nanoparticles at off-resonance wavelength," *Optical Quantum Electronics* **43**, 49-58 (2012).

[69] C. Zheng, X. Y. Ye, S. G. Cai, M. J. Wang, and X. Q. Xiao, "Observation of nonlinear saturable absorption and reverse saturable absorption in silver nanowires and their silica gel glass composite," *Applied Physics B* **101**, 835-840 (2010).

[70] L. de Boni, E. C. Barbano, T. A. de Assumpcao, L. Misoguti, L. R. P Kassab, and S. C. Zilio, "Femtosecond third-order nonlinear specra of lead-germanium oxide glasses containing silver nanoparticles," *Optics Express* **20**, 6844-6850 (2012).

[71] R. A. Ganeev, M. Baba, A. I. Ryasnyansky, M. Suzuki, and H. Kuroda, "Characterization of optical and nonlinear optical properties of silver nanoparticles prepared by laser ablation in various liquids," *Optics Communications* **240**, 437-448 (2004).

[72] B. Karthikeyan, J. Thomas, and R. Philip, "Optical nonlinearity in glass-embedded silver nanoclusters under ultrafast laser excitation," *Chemical Physics Letters* **414**, 346-350 (2005).

[73] R. de Nalda, R. del Coso, J. Requejo-Isidro, J. Olivares, A. Suarez-Garcia, J. Solis, and C. N. Afonso, "Limits to the determination of the nonlinear

refractive index by the Z-scan method," *Journal of the Optical Society of America B* **19**, 289-296 (2002).

[74] B. Karthikeyan, M. Anija, C. S. S. Sandeep, T. M. M. Nadeer, and R. Philip, "Optical and nonlinear optical properties of copper nanocomposite glasses annealed near the glass softening temperature," *Optics Communications* **281**, 2933-2937 (2008).

[75] R. A. Ganeev, A. I. Ryasnyansky, A. L. Stepanov, and T. Usmanov, "Characterization of nonlinear optical parameters of copper- and silver-doped silica glasses at 1064 nm," *Physics of State Solid (b)* **241**, 935-944 (2004).

[76] R. A. Ganeev, A. I. Ryasnyansky, A. L. Stepanov, and T. Usmanov, "Saturated absorption and reverse saturated absorption of Cu:SiO_2 at 532 nm," *Physics of State Solid (b)* **241**, R1-R4 (2004).

[77] T. Cesca, P. Calvelli, G. Battaglin, P. Mazzoldi, and G. Mattei, "Local-field enhancement effect on the nonlinear optical response of gold-silver nanoplanets," *Optics Express* **20**, 4537-4547 (2012).

[78] T. Cesca, G. Pellegrini, V. Bello, C. Scian, P. Mazzoldi, P. Calvelli, G. Battaglin, and G. Mattei, "Nonlinear optical properties of Au-Ag nanoplanets made by ion beam processing of bimetallic nanoclusters in silica," *Nuclear Instruments and Methods in Physics Research B* **268**, 3227-3230 (2010).

[79] J. T. Seo, Q. Yang, *et al.*, "Optical nonlinearities of Au nanoparticles and Au/Ag coreshells," *Optics Letters* **34**, 307-309 (2009).

[80] R. Philip, and G. R. Kumar, "Picosecond optical nonlinearity in monolayer-protected gold, silver, and gold-silver alloy nanoclusters," *Physical Review B* **62**, 160-166 (2000).

[81] Y.-K. Yoon, R. S. Bennink, R. W. Boyd, and J. E. Sipe, "Intrinsic optical bistability in a thin layer of nonlinear optical material by means of local field effects," *Optics Communications* **179**, 577-580 (2000).

[82] J .W. Haus, N. Kalyaniwalla, R. Inguva, M. Bloemer, and C. M. Bowden, "Nonlinear-optical properties of conductive spheroidal particle composites," *Journal of the Optical Society of America B* **6**, 797-807 (2002).

[83] K. M. Leung, "Optical bistability in the scattering and absorption of light from nonlinear microparticles," *Physical Review A* **33**, 2461-2464 (1986).

[84] D. J. Bergman, O. Levy, and D. Stroud, "Theory of optical bistability in a weakly nonlinear composite medium," *Physical Review B* **49**, 129-134 (1994).